Investigation of the Photophysical Properties of π-Conjugated Polymers

A Study by Non-Linear, Time-Resolved, and Single-Molecule Spectroscopy

Von der Universität Bayreuth
zur Erlangung des Grades eines
Doktors der Naturwissenschaften (Dr. rer. nat.)
genehmigte Abhandlung

eingereicht von

Richard Hildner
geboren in Stadtsteinach

1. Gutachter: Prof. Dr. J. Köhler
2. Gutachter: Prof. Dr. A. Köhler

Tag der Einreichung: 14.12.2007
Tag des Kolloquiums: 30.04.2008

Contents

Chapter 1

Introduction

In 1976 Alan J. Heeger, Alan G. MacDiarmid, H. Shirakawa, and co-workers demonstrated in a pioneering work that polyacetylene, structurally one of the simplest π-conjugated polymers, can be made highly conductive by doping with halogens and arsenic pentafluoride (AsF_5) [1]. For this work the Nobel price in chemistry was awarded to Heeger, MacDiarmid, and Shirakawa in 2000. This discovery stimulated intense research both in industry and academia to develop novel materials and applications based on organic materials. A major breakthrough in this new field of *organic electronics* was the demonstration of the first light-emitting diode based on a small organic molecule [tris(8-hydroxy-quinoline) aluminium, Alq_3] reported by Tang and VanSlyke from the Eastman Kodak research laboratories in 1987 [2]. Three years later, in 1990, the first organic light-emitting diode based on a π-conjugated polymer [poly(*para*-phenylenevinylene), PPV] was presented in the research group of Richard H. Friend in Cambridge [3].

Since then the number of applications based on organic molecules as active materials has grown rapidly. Besides organic light-emitting diodes (OLEDs) optically pumped organic lasers, photovoltaic cells, field effect transistors, non-volatile and dynamic random-access memory elements, and sensitive chemical sensors for measuring e. g. DNA concentrations have been developed [2–11]. By now several applications, such as electric razors and mobile phones, equipped with small displays based on organic molecules are commercially available. And in October 2007 Sony announced the market launch of the world's first *OLED-TV* [12]. This impressively demonstrates the progress that has been made in this field during the last two decades.

For several applications the use of organic materials is advantageous with respect to silicon and the inorganic semiconductor technologies. Organic systems combine the electronic and optical properties of (semi-)conductors with the mechanical properties of polymers

(plastics). Applying the rich toolbox of organic macromolecular chemistry many different systems with tailor-made properties can be synthesised, particularly the band gap ($\pi - \pi^*$ gap) can be tuned across the visible range of the spectrum by chemical synthesis [11,13–15]. Functionalised side-groups bound to the backbone of the molecules provide excellent solubility in organic solvents. As a result, the materials can be deposited from solution by spin-coating or ink-jet printing, which allows for easy processing and low-cost manufacturing of devices [15–17]. In contrast to inorganic semiconductors the organic systems do not require rigid, crystalline substrates, but may be cast on nearly any desired material, in particular on large-area, flexible substrates [16–18]. Hence, novel applications come within reach, such as flexible displays or electronic circuits printed directly on packings (e. g. radio-frequency identification chips, RFID-chips) [17, 18], that can not be realised with conventional semiconductor technologies. Further interesting prospects arise from the exploitation of self-organisation processes of π-conjugated oligomers to build supramolecular structures [19, 20]. Such structures constitute model systems for future light harvesting architectures and for the study of excitation energy transfer mechanisms, because self-organisation provides precise control of the mutual distance and orientation between adjacent oligomers.

Many applications of conjugated polymers require high mobilities of charge carriers and/or electronic excitations. These mobilities are determined both by device-specific properties as well as intrinsic electronic properties of these functional organic materials [4,11,21]. In particular, the nature of the lowest electronically excited states in conjugated polymers determines the electronic properties that are exploited in optoelectronic devices. Additionally, detailed knowledge about the dynamics of electronic excitations within the density of electronically excited states and about their decay kinetics into the electronic ground state is necessary for a further optimisation of the performance of optoelectronic devices [11,22]. Hence, in parallel with the development of applications, there is tremendous effort to elucidate and understand the intrinsic electronic and optical properties of π-conjugated polymers both by experiments and theoretical modelling [11,21–31]. In particular, the microscopic understanding of the dynamics and relaxation pathways of electronic excitations as well as of electron-electron interactions and the electron-phonon coupling is still not complete.

Information about such key factors can generally be obtained by optical spectroscopy. However, to determine these various parameters, a combination of spectroscopic techniques has to be employed. Therefore, two-photon fluorescence excitation and time-resolved spectroscopy on thin conjugated polymer films as well as fluorescence spectroscopy on individual conjugated polymer chains is performed in this work.

Because conjugated polymers are usually centrosymmetric molecules, the electronic states possess a well-defined parity, where the electronic ground state has even parity and the higher electronically excited singlet states are of alternating odd and even parity [21, 23, 25, 26]. Hence, two-photon spectroscopy allows the excitation and characterisation of higher lying electronic singlet levels with even parity [32–38], that are not accessible by conventional one-photon spectroscopy due to symmetry selection rules. In this respect, two-photon spectroscopy is an ideal complementary technique to one-photon spectroscopy.

Time-resolved spectroscopy allows the determination of the dynamics and relaxation pathways of electronic excitations within the density of electronically excited states as well as the decay kinetics to the electronic ground state. This allowed to model the excitation energy transfer as energy dispersive hopping of electronic excitations towards energetically lower lying sites within the distribution of excited states [39–48]. Particularly, measuring the spectrally resolved decay kinetics by employing Streak camera techniques permits to gain a detailed insight into these issues.

Typically, conjugated polymer samples are very heterogeneous with a high degree of disorder [28, 30, 49]. This leads to strong inhomogeneous line broadening of their ensemble spectra and as a consequence of this, only averaged parameters are accessible by conventional optical spectroscopy. In order to retrieve the entire distribution of parameters single-molecule spectroscopy may be applied. Since the beginnings in 1989 [50, 51] this technique has rapidly evolved and in the last few years single-molecule spectroscopy has been employed to investigate the photophysics of conjugated polymers by several groups [49, 52–61]. This allowed to obtain detailed information about excitation energy transfer pathways [52–54], chain conformations [49, 52, 55, 57, 58], the coherence length of electronic excitations [59], and photon antibunching from single polymer chains [60, 61].

The conjugated polymer that is investigated in this work is a rigid, rod-like ladder-type conjugated polymer, methyl-substituted ladder-type poly(*para*-phenylene), MeLPPP. This is an ideal polymer to study with spectroscopic techniques because this system features a high fluorescence quantum yield of 25 % in films and 80 % in solution [62, 63], a very low defect concentration, excellent solubility in organic solvents and miscibility with inert polymers [7, 13]. In addition, the low intra-chain disorder owing to its rigid, rod-like backbone [7, 13, 64] leads to small inhomogeneous line broadening of the ensemble spectra of MeLPPP.

This work is organised as follows: In chapter 2 the photophysical properties of conjugated polymers and basic theoretical concepts are introduced. The experimental setup and the sample preparation for the various measurements is briefly described in chapter 3. Chapter 4 deals with two-photon fluorescence excitation spectroscopy on thin MeLPPP-

films at room temperature, where the symmetry properties of the vibronic wavefunctions in the lowest electronically excited singlet states of MeLPPP are studied. In chapter 5 the results of time-resolved spectroscopy on thin MeLPPP-films both at 1.5 K and at room temperature are presented. The relaxation dynamics within the distribution of the electronically excited states is investigated and the non-exponential decay kinetics of the lowest electronically excited level is discussed in terms of a distribution of excited state lifetimes. Finally, single-molecule fluorescence spectroscopy experiments at low temperatures are presented in chapter 6. In combination with statistical pattern recognition techniques for data analysis this allows to retrieve the electron-phonon coupling strength in MeLPPP at low temperatures and to shed some light on the origin of the strong spectral diffusion processes of the optical transitions.

Chapter 2

Photophysical Properties of Conjugated Polymers

In this chapter the basic photophysical properties of π-conjugated polymers are presented. After a short introduction into theoretical concepts for π-conjugated systems and the chromophore picture of π-conjugated polymers, the electronic and spectral properties of chromophores are described. In particular, linear and nonlinear optical transitions and the corresponding selection rules, homogeneous and inhomogeneous line broadening mechanisms of the optical spectra, electron-phonon coupling and excitation energy transfer processes will be introduced.

2.1 Introduction to π-Conjugated Polymers

2.1.1 Hybridisation

Carbon-based materials form a large number of structures comprising the crystalline diamond, small molecules (e. g. methane, CH_4), as well as very complex organic macromolecules (e. g. polycyclic aromatic hydrocarbons such as terrylene or polymers such as polystyrene). This rich variety of structures arises from different atomic orbital hybridisations of carbon, in which its outer four valence orbitals ($2s, 2p_x, 2p_y, 2p_z$) are involved. In this quantum chemical approximation linear combinations of these atomic orbitals are constructed that lead to three types of hybridisation [23, 65].

sp^3-hybridisation: All four valence orbitals of carbon are involved and allow to form three-dimensional structures, such as in methane, CH_4, where the carbon atom sits in the centre and the four hydrogens reside in the four corners of a tetrahedron (Fig. 2.1a). The

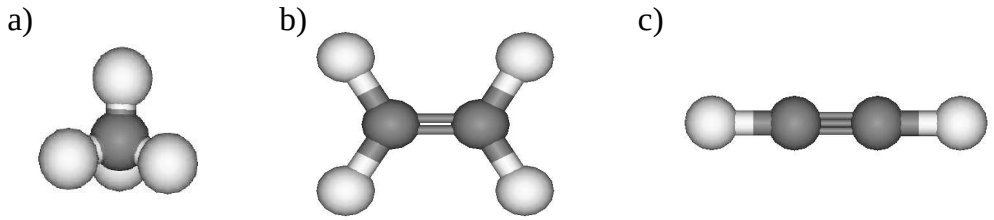

Figure 2.1: Hybridisations of carbon. a) Methane with a sp^3-hybridised carbon forms a three-dimensional, tetrahedral structure. b) Ethylene with sp^2-hybridised carbons has a planar geometry. c) Acetylene with *sp*-hybridised carbons is a linear molecule. Carbon atoms are depicted as dark-grey balls and hydrogen atoms are shown as light grey balls.

four equivalent bonds between the carbon and the hydrogens are highly directional and known as σ-bonds. These are characterised by a cylindrical symmetry of the electron density along the bond (C-H) axis, and result in a *single* bond between each H and the C atom.

sp^2-hybridisation: Here, three hybrid orbitals per carbon atom are built from the $2s, 2p_x$, and $2p_y$ atomic orbitals. This leads to the formation of three σ-bonds in one plane and thus to a planar structure of the molecule as for example in ethylene, $H_2C{=}CH_2$ (Fig. 2.1b). The remaining $2p_z$ orbitals of the two carbon atoms are oriented perpendicular to the plane spanned by the σ-bonds. The overlap of these p_z orbitals forms a π orbital, which is mirror symmetric with respect to the plane of the σ-bonds. The π orbital locks the molecule in its planar geometry because every rotation around the carbon – carbon axis would weaken the π-bond. The pair of a σ- and π-bond between two carbons results in a *double* bond.

sp-hybridisation: Only the $2s$ and $2p_x$ orbitals of each carbon are used to construct two hybrid orbitals per carbon, which form two σ-bonds. *sp*-hybridised molecules are linear such as acetylene, HC≡CH (Fig. 2.1c). The overlap of the remaining $2p_y$ and $2p_z$ orbitals gives rise to the formation of two π-bonds between the carbons which are perpendicular to each other. Together with the two σ-bonds between the C-atoms, a *triple* bond between the carbons arises.

Molecules with sp^3-hybridisation are also known as *saturated* molecules, sp^2- or *sp*-hybridised molecules are referred to as *unsaturated*.

A π-conjugated molecule is defined by alternating single and double bonds between the carbon atoms along the backbone [66]. Thus, a π-conjugated polymer (CP) chain can be built from the ethylene geometry with its sp^2-hybridisation. This leads to one of the most prominent π-conjugated polymers, *trans*-polyacetylene (*t*-PA), with alternating single and double bonds between the carbon atoms in the backbone (Fig. 2.2a). Further examples

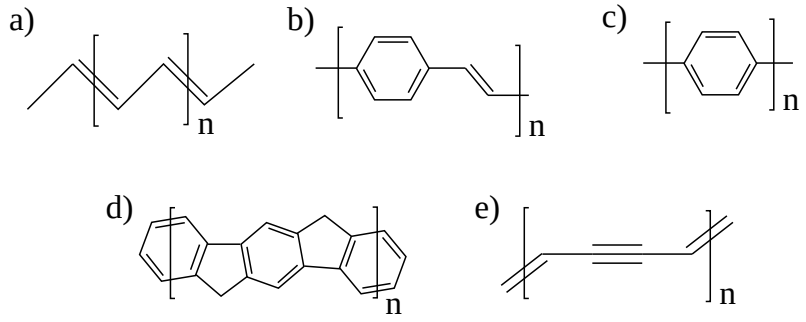

Figure 2.2: Chemical structures of common π-conjugated polymers. a) *trans*-polyacetylene, b) poly(*para*-phenylenevinylene), c) poly(*para*-phenylene), d) ladder-type poly(*para*-phenylene), e) polydiacetylene.

of CPs are poly(*para*-phenylenevinylene) (PPV), poly(*para*-phenylene) (PPP), and ladder-type poly(*para*-phenylene) (LPPP), see Fig. 2.2. Generally, all widely-used CPs comprise an uninterrupted series of sp^2-hybridised C-atoms along their backbone. An exception from this rule is polydiacetylene (PDA) with both *sp*- and sp^2-hybridised carbons. Consequently, PDA possesses alternating single and double/triple bonds between the carbons along its backbone (Fig. 2.2e).

In π-conjugated molecules the electrons in the σ orbitals are localised in highly directional bonds, while the π-electrons may delocalise over the entire molecule. As a consequence, the binding energy of the σ-electrons is much larger than that of the π-electrons [23, 28, 65]. This separation of energy scales allows the reasonable approximation that the σ orbitals determine the geometric structure of the molecules and may therefore be described by the valence bond theory as discussed above. In contrast, the π electrons determine the particular optical and electronic properties of CPs at "low" energies up to about 3 eV and are described in the molecular orbital terminology.

The energy difference between bonding and antibonding (labelled by an asterisk) orbitals depends on the nature of the orbitals (σ, π) and on the extend of electronic delocalisation [23, 28]. Whereas a $\sigma - \sigma^*$ transition in CPs requires an energy of about $80000\,\mathrm{cm}^{-1}$ (10 eV) and still higher energies, the lowest energy electronic transition is a $\pi - \pi^*$ transition between the highest occupied molecular orbital (HOMO, π orbital) and the lowest unoccupied molecular orbital (LUMO, π^* orbital). Typically, the energy required for this transition is between $16000\,\mathrm{cm}^{-1}$ and $25000\,\mathrm{cm}^{-1}$ (2 eV and 3.1 eV), which is in the visible/near ultraviolet region of the spectrum. Because the HOMO – LUMO separation is similar to the band gap in conventional inorganic semiconducting materials, CPs are also referred to as *organic semiconductors*.

Owing to the large difference of the energy scales between σ and π orbitals in CPs theoretical models, that describe their electronic and optical properties, typically neglect the dynamics of the σ electrons and focus on that of the π electrons [23, 28, 65] as will be discussed in the next section.

2.1.2 π-Electron Models

The electronic and optical properties of conjugated polymers are described by a many body Hamilton operator [21, 23, 28]

$$H = H_{n-n}(\{\mathbf{R}\}) + H_{e-e}(\{\mathbf{r}\}) + H_{e-n}(\{\mathbf{r}\}, \{\mathbf{R}\}), \tag{2.1}$$

where $\{\mathbf{R}\}$ and $\{\mathbf{r}\}$ denote the set of nuclear and electronic coordinates, respectively. The first term on the right-hand side of eq. (2.1) represents the kinetic energy of the nuclei and their mutual interactions, the second term stands for the kinetic energy of the electrons and the interactions between the electrons (electron-electron correlations), and the last term describes the interaction between the electrons and nuclei (i. e. the electron-phonon coupling). However, the Schrödinger equation with the Hamiltonian (2.1) cannot be solved exactly for complex systems such as CPs; an exact solution is only possible for the hydrogen atom in free space.

Hence, several approximations to describe the π-electron system have been developed. One of the most important is the Born-Oppenheimer (BO) approximation [21,23,24] which is based on the fact that the mass of an electron is much smaller than the mass of a nucleus ($m_\mathrm{e}/m_\mathrm{n} \approx 10^{-4}$). Therefore the electronic dynamics is much faster than the nuclear dynamics. The total wave function may then be written as a direct product of an electronic state $|e(\{\mathbf{r}\}, \{\mathbf{R}\})\rangle$, which depends parametrically on the set of nuclear coordinates $\{\mathbf{R}\}$, and an associated nuclear state $|\nu(\{\mathbf{R}\})\rangle$. In the first step, the kinetic energy of the nuclei in eq. (2.1) is neglected and the eigenvalue equation for the electronic wave functions $|e(\{\mathbf{r}\}, \{\mathbf{R}\})\rangle$ is solved. This procedure yields the eigenvalues $E_e(\{\mathbf{R}\})$, which are again a parametric function of the nuclear coordinates and which describe an effective potential experienced by the nuclei. $E_e(\{\mathbf{R}\})$ is also known as *adiabatic potential energy surface* and is a specific potential for an electronic state. Next, the eigenvalue equation for the nuclei with the effective potential $E_e(\{\mathbf{R}\})$ in harmonic approximation is solved, which describes the nuclear vibrations of the molecule (in the potential energy surface of a particular electronic state).

Within the BO approximation all interactions (electron-electron, nuclei-nuclei, and electron-phonon interactions) are retained. Therefore, it is still too complicated to find so-

lutions for the Hamilton operator (2.1) within this approximation even if only the dynamics of the π electrons is included and that of the σ electrons is neglected. Therefore further approximations have been made and each model focuses on a different aspect to describe the properties of CPs. The first model for π-conjugated molecules was proposed by E. Hückel in 1931 [67–69] and makes the most drastic approximation since both electron-electron and electron-phonon interactions are neglected (besides other simplifications). The σ orbitals determine the geometric structure of the molecule, i. e. the positions of the nuclei are considered to be fixed, and only the energies and eigenfunctions of the π orbitals are calculated from a linear combination of atomic orbitals (LCAO) of the carbons. The Pariser-Parr-Pople (PPP) model [70–72] explictly takes into account electron-electron interactions, but still assumes fixed nuclei (no electron-phonon coupling). The Su-Schrieffer-Heeger (SSH) model [73,74] neglects electron-electron interactions but includes electron-phonon coupling. In this model the electron-phonon coupling is limited to the predominating normal mode, the carbon – carbon bond stretch at about $1500\,\mathrm{cm}^{-1}$, that couples to the π system. The SSH theory was developed to describe the electronic structure of polyacetylene after its electrical conductivity upon doping was discovered [1].

It has been realised from many experimental observations and theoretical modelling that a complete description of the optical and electronic properties of conjugated polymers requires to include both electron-electron and electron-phonon interactions in one model (see Refs. [21, 23, 25, 27, 28] and references therein). Hence, the models briefly introduced above can be only limiting cases. However, so far approximate solutions of models that include all interactions have only been obtained for idealised, crystalline structures [23, 25, 26, 75]. More recently approximate results for perfectly aligned individual oligomer chains with only few repeating units have also been obtained [22, 75–82]. For long chain polymers with several tens to hundreds of repeating units the situation is more complicated because the polymers usually exhibit a highly disordered chain conformation (besides their large number of atoms). The modelling of the electronic structure of long and disordered conjugated polymer chains is still beyond todays capabilities if all relevant interactions are taken into account. Finally, the influence of the side groups bound to the polymer backbone and the local environment of the CPs has to be included to develop a coherent picture of the nature of their electronic states [23, 28, 81].

2.1.3 Chromophores in Conjugated Polymers

For an ideal, perfectly stretched CP chain described with the Hückel model one would expect the π electron system to be delocalised along the entire polymer backbone and the

overlap of the π-electron wave functions would not be interrupted in the molecule. However, it has been shown that electron-electron and particularly electron-phonon interactions lead to a localisation of the wave functions on subunits of a chain [28, 76, 83]. Additionally, a CP chain is typically not perfectly aligned, but exhibits a disordered chain conformation due to structural defects [28, 30, 49] such as kinks, strong bending of the chain, and large torsional angles between adjacent phenylene-rings. Moreover, a polymer chain contains to some extend chemical defects, e. g. impurities or sp^3-hybridised carbon atoms. Both the conformational and chemical defects interrupt the π-conjugation along the backbone. According to a model put forward by Bässler and co-workers [29,84,85] a CP may therefore be represented as a chain of short linear subunits each comprising several repeating units (typically 5 – 15 monomers). These linear segments are separated by chemical and/or conformational defects along the polymer backbone, which give rise to a scission of the π-electron system. The fully conjugated subunits of the chain are commonly referred to as chromophores, segments or sites and the length of such a segment (in terms of the number of repeating units) is called *conjugation length*.

Conjugated polymer chains may be as long as several hundreds of repeating units and accordingly contain tens to hundreds of sites per chain [30, 49, 60]. Therefore, a CP constitutes an intrinsically multichromophoric system which is schematically shown in Fig. 2.3. Due to the fact that the chemical/conformational defects, which break the π-conjugation, are statistically distributed, a distribution of conjugation lengths is present in a polymer sample. The average conjugation length is known as *effective conjugation length*. It has been found that both the effective conjugation length and the width of the distribution of conjugation lengths depends on the chemical structure of the polymer (flexibility of the backbone) as well as on the sample processing and preparation, such as solvent polarity, temperature, polymer concentration, film deposition procedure, and thermal annealing [30, 49, 57, 60, 86, 87].

The effective conjugation length of CPs is typically determined from a comparison of the optical spectra of the polymer with those of the corresponding oligomers [85]. It has been found from measurements on short oligomers with increasing chain lengths, i. e. for an increasing degree of π electron delocalisation, that the energy separation between the HOMO and LUMO levels decreases, and consequently the optical spectra shift towards higher wavelengths [76, 83, 88]. Finally, a saturation of the shift is observed for longer oligomers (or short chain polymers). The length of the oligomer, where the onset of the saturation is found, defines the effective conjugation length for the polymer [83, 85].

Owing to the finding that the energy separation between the HOMO and LUMO levels depends on the π electron delocalisation the distribution of conjugation lengths present in

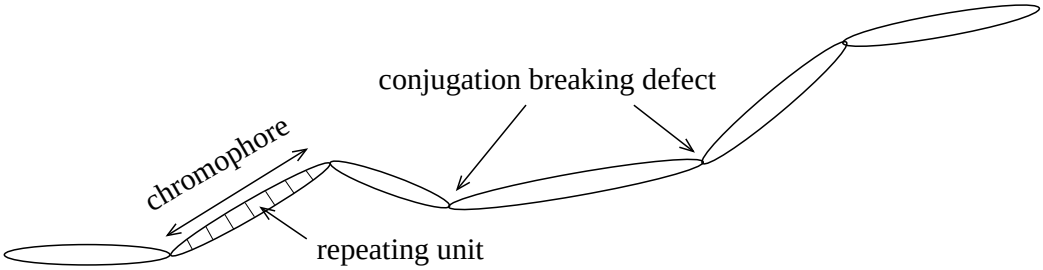

Figure 2.3: Schematic representation of a π-conjugated polymer chain. Due to conformational and/or chemical defects the π-conjugation along the polymer backbone is interrupted. This leads to the formation of several, fully conjugated subunits on a single chain, the so-called chromophores, each with a length of typically 5 – 15 repeating units.

a CP sample directly translates into a distribution of HOMO – LUMO transition energies. This effect contributes to the inhomogeneous line broadening of the ensemble spectra of CPs, which will be discussed in section 2.2.4.

Recent theoretical work addressed the issue of the formation of chromophores in CPs by quantum chemical calculations on short chain oligo(thiophenes) and oligo(phenylene-vinylenes) with up to 30 repeating units. It was assumed that these systems contain two perfectly aligned branches that are connected by either a kink, ring torsion, or a sp^3-hybridised carbon [79, 80]. It was found that the ground state wave function is delocalised over the entire oligomer (i. e. across the 'defect' over both branches) except in the presence of a sp^3-hybridised carbon. In other words, only for a missing double bond between two carbon atoms along the backbone a segmentation of the chain into chromophores occurs, whereas kinks and ring torsions do not interrupt the π-conjugation (in contrast to the simple picture described above). Immediately after creating a photoexcitation the situation in the excited state is similar. However, within the first few tens of femtoseconds after the absorption process a dynamic localisation of the electronic excitations on the perfect chain segments ("exciton self-trapping") is expected due to a structural relaxation of the backbone into its excited state equilibrium geometry caused by electron-phonon coupling [76, 79, 80]. Any further relaxation or deactivation process of electronic excitations (emission, energy transfer, see the following sections) occurs after full geometric relaxation [80].

To conclude this introductory part, it is worth noting that as yet all theoretical descriptions and concepts of e. g. chromophore formation in CPs suffer from several shortcomings. The validity of these models relies on a precise knowledge of the fundamental electronic parameters of CPs, such as electron-electron interactions and electron-phonon coupling strengths. The calculations are performed for individual, isolated polymer chains, the pa-

rameters, however, are determined from ensemble data of CPs [20, 27, 76, 81]. Therefore a direct comparison between theory and experiment is very difficult due to the highly disordered sample morphologies of CPs. Moreover, the parameters found from ensemble data are restricted to averaged values. In contrast, single-molecule experiments allow to determine the entire distribution functions of the parameters, which will be demonstrated in chapter 6. Thus a direct verification of theoretical models comes within reach. In recent years it has been shown that single-molecule spectroscopy is indeed a valuable tool to overcome the intrinsic heterogeneity of bulk CP samples and to investigate the properties of the electronic states of individual conjugated polymer chains in great detail [52–56, 89–94].

2.2 Electronic and Spectral Properties of Chromophores

2.2.1 Jablonski Diagram of Chromophores

An energy level scheme for conjugated polymers is depicted in the Jablonski diagram in Fig. 2.4 and closely resembles that of a low molecular weight organic dye molecule [95–97]. In CPs the electronic ground state (HOMO) and the lowest electronically excited state (LUMO) are both singlet levels due to typically weak spin-orbit coupling in CPs, and are labelled S_0 and S_1, respectively. In addition, a manifold of higher singlet states (S_n, $n \geq 2$) and a series of triplet states (T_1, T_2, ...) exist, where only the lowest levels are shown in Fig. 2.4. The vibrational levels (labelled $\nu_i^{(\prime)}$, $i = 0, 1, 2$) and phonon levels coupled to the electronic states are also depicted in Fig. 2.4.

For conjugated polymers the lowest optically allowed electronic transition ($S_1 \leftrightarrow S_0$ or $\pi^* - \pi$, the selection rules for optical transitions are detailed in the next sections) has transition energies between about $16000\,\mathrm{cm}^{-1}$ and $25000\,\mathrm{cm}^{-1}$ [7, 21, 28], which is in the visible/near ultraviolet region of the spectrum as mentioned earlier. A higher excited singlet level was found 1000 – $5000\,\mathrm{cm}^{-1}$ above S_1 by two-photon and pump-probe spectroscopy [33,34,36–38,98,99]. However, the assignment of this electronic state is not always unambiguously clear and therefore this level is usually labelled S_n, with $n \geq 2$. The lowest triplet state T_1 is always located about $5500\,\mathrm{cm}^{-1}$ below the lowest excited singlet level S_1 despite different S_1 – S_0 gaps for various CPs [28, 100–102]. This finding of a large singlet-triplet exchange energy highlights the importance of electron-electron correlations in conjugated polymers (see section 2.1.2).

The dominating vibrations, that couple to the electronic levels and may be observed in

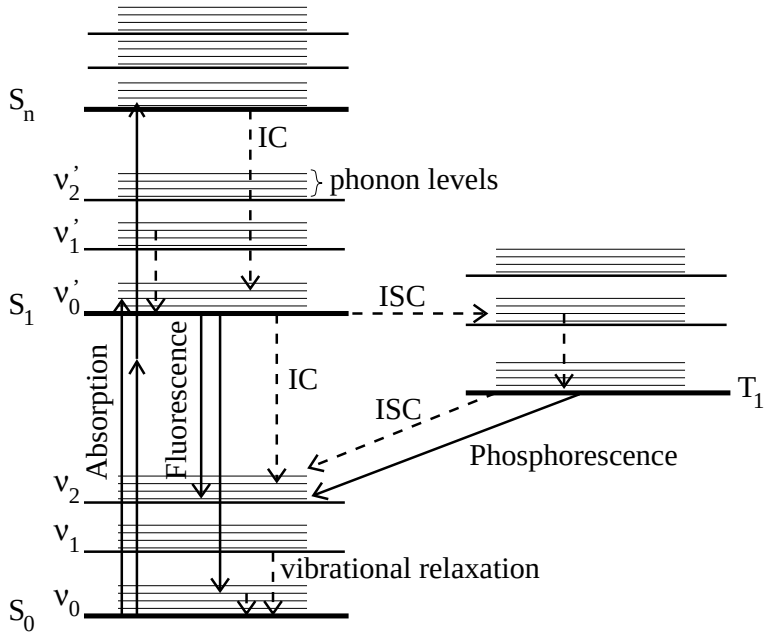

Figure 2.4: Simplified Jablonski diagram of a chromophore. Radiative transitions are drawn as solid arrows, and non-radiative transitions are depicted as dashed arrows. IC stands for internal conversion and ISC for intersystem crossing. For further details see text.

the optical spectra, are carbon – carbon bond stretching modes with energies between about $1300\,\mathrm{cm}^{-1}$ and $1600\,\mathrm{cm}^{-1}$ and their overtones. Moreover, quantum-chemical modelling of ensemble spectra of CPs indicated that low-energy vibrational modes with energies between about $60\,\mathrm{cm}^{-1}$ and $160\,\mathrm{cm}^{-1}$ couple to the electronic and vibronic levels as well [20,22,76,81, 88,103]. These low-frequency vibrations were identified as torsions/librations of phenylene- or thiophene-rings in the polymer backbone [20, 22, 76, 81] or longitudinal acoustic modes of the backbone [81, 88, 103]. In addition to these intra-molecular modes, it is well-known from optical spectroscopy (hole burning, site-selective fluorescence spectroscopy) on dye molecules that low-energy vibrations (10 – $100\,\mathrm{cm}^{-1}$) of the surrounding host matrix may by excited in combination with vibronic transitions as well [104–107]. All low-energy vibrations with energies $\lesssim 200\,\mathrm{cm}^{-1}$, i. e. intra-molecular vibrations and vibrations of the host material, will be also referred to as phonons throughout this work, irrespective of the structure (crystalline/amorphous) of the CPs and the host matrix.

Upon absorption of photons chromophores will be excited into a vibrational/phonon level of one of the electronically excited singlet states. After excitation into a vibrational/phonon level of the lowest excited singlet state S_1 fast vibrational relaxation within about $200\,\mathrm{fs}$ [39, 42, 108, 109] into the vibrational ground state of S_1 occurs. If initially a higher lying singlet level S_n ($n \geq 2$) is excited, ultra-fast internal conversion (IC) within

about 50 fs into the lowest excited singlet state [99] with subsequent vibrational relaxation into the ground vibrational level of S_1 takes place. IC is a non-radiative transition between electronic states with the same spin multiplicity. As a consequence of this, the fluorescence from CPs is independent of the initially excited singlet state [33,34,36,37,99] according to Kasha's rule [97]. Fluorescence is a radiative transition between electronic levels with the same spin multiplicity.

In addition to fluorescence the lowest excited state S_1 may also be deactivated by the non-radiative processes IC, quenching at chemical or structural defects, and intersystem crossing (ISC). Whereas in solution quenching at defects is negligible [63], in films it becomes a significant deactivation process due to a denser chain packing and consequently more efficient and rapid excitation energy transfer to defect sites (see Refs. [30, 31, 48] and section 2.3). However, the contributions of IC and quenching at defects to the non-radiative decay in films can not always be quantified and are still a matter of debate (see e. g. Refs. [31, 62]). ISC is a non-radiative transition between two electronic levels with different spin multiplicity and is weakly allowed due to weak spin-orbit coupling in CPs. This process leads to the population of the lowest triplet state T_1 from S_1. The T_1 level usually decays radiationless into the electronic ground state S_0 via ISC. However, for methyl-substituted LPPP phosphorescence, i. e. the radiative $T_1 - S_0$ transition, has also been observed with a gated time-resolved technique [101, 110]. To detect phosphorescence from other CP systems the spin-orbit coupling has to be increased for example by doping with metal atoms [100, 102].

2.2.2 Linear and Nonlinear Optical Processes

In the following the interaction of electromagnetic fields with matter will be shortly introduced with an emphasis on one- and two-photon absorption processes. This will finally lead to the derivation of selection rules that determine whether electronic/vibronic transitions are allowed and thus take place under absorption or emission of photons.

The response of a medium (more precisely, the response of the bound electrons) upon applying an external electric field $\mathbf{E}$ can be expressed as a macroscopic polarisation $\mathbf{P}$. At higher electric fields, this response becomes nonlinear and is usually written as a power series expansion of the electric field

$$\mathbf{P} = \varepsilon_0 \Big(\chi^{(1)}\mathbf{E} + \chi^{(2)}\mathbf{E}\cdot\mathbf{E} + \chi^{(3)}\mathbf{E}\cdot\mathbf{E}\cdot\mathbf{E} + \dots \Big). \tag{2.2}$$

ε_0 is the dielectric constant in free space. $\chi^{(n)}$ denotes the n^{th} order electrical susceptibility, which is generally a tensor of rank $n+1$, and can be calculated by time-dependent pertur-

bation theory [23, 111–113]. The effect of the linear susceptibility $\chi^{(1)}$ is that the external electric field with frequency ω induces an oscillating polarisation at the same frequency ω. Therefore, this contribution gives rise to a linear absorption (and emission) process of *one* photon. The behaviour of the higher order terms ($\chi^{(2)}$ and $\chi^{(3)}$) is more complicated and they describe nonlinear effects [23, 111, 112] such as sum and difference frequency generation and second harmonic generation ($\chi^{(2)}$), as well as third harmonic generation, the optical Kerr-effect, and two-photon absorption ($\chi^{(3)}$). Since CPs are usually centrosymmetric molecules (*vide infra*), the polarisability has to reverse the sign if the sign of the external electric field is changed. Consequently, all even powers of the electric field $\mathbf{E}$ in eq. (2.2) have to vanish and the lowest nonlinear susceptibility in CPs is $\chi^{(3)}$.

One-Photon Absorption

The linear susceptibility, derived by 1st order perturbation theory, reads [111, 112]

$$\chi^{(1)} = \frac{e^2}{3\varepsilon_0\hbar}\left|\mathbf{n}\cdot\hat{\mathbf{M}}_{if}\right|^2 \cdot \left(\frac{1}{\omega_f - \omega - ik_f} + \frac{1}{\omega_f + \omega + ik_f}\right), \tag{2.3}$$

where e stands for the electronic charge, ω and $\mathbf{n}$ denote the frequency and polarisation of the external electric field, respectively, $\omega_f = (E_f - E_i)/\hbar$ is the frequency for the transition between the initial $|i\rangle$ and final (excited) state $|f\rangle$ with energies E_i and E_f, respectively, and k_f is the spontaneous decay rate of the excited state. $\hat{\mathbf{M}}_{if}$ represents the transition dipole matrix element

$$\hat{\mathbf{M}}_{if} = \langle f|\hat{\mathbf{p}}|i\rangle \tag{2.4}$$

for the transition between the ground and the final state.

$$\hat{\mathbf{p}} = e \cdot \sum_m \mathbf{r}_m \tag{2.5}$$

is the dipole moment operator, where the sum runs over the coordinates $\mathbf{r}_m$ of all electrons. It is immediately clear that an optically allowed one-photon transition requires a nonzero transition dipole matrix element (2.4) in order to get a non-vanishing linear susceptibility $\chi^{(1)}$ in eq. (2.2).

Within the Born-Oppenheimer approximation the dipole matrix element (2.4) can be further expanded. The total wave functions are written as direct products of electronic and nuclear wave functions, $|i(\{\mathbf{r}\},\{\mathbf{R}\})\rangle = |e_i(\{\mathbf{r}\},\{\mathbf{R}\})\rangle \cdot |\mu(\{\mathbf{R}\})\rangle$ and $|f(\{\mathbf{r}\},\{\mathbf{R}\})\rangle = |e_f(\{\mathbf{r}\},\{\mathbf{R}\})\rangle \cdot |\nu(\{\mathbf{R}\})\rangle$ (see section 2.1.2, for simplicity the electronic and nuclear coordinates will be omitted in the following). Thus eq. (2.4) becomes

$$\hat{\mathbf{M}}_{if} = \langle f|\hat{\mathbf{p}}|i\rangle = \langle e_f|\hat{\mathbf{p}}|e_i\rangle \cdot \langle \nu|\mu\rangle, \tag{2.6}$$

where the first term in the product on the rightmost side is the electronic transition dipole moment, and the square magnitude of the second term is known as *Franck-Condon factor*

$$F_{\nu\mu} = |\langle\nu|\mu\rangle|^2. \tag{2.7}$$

The integrals in eq. (2.6) are evaluated at the same values of the set of nuclear coordinates ($\{\mathbf{R}\}$) in the initial and final electronic state, because within the BO approximation an electronic transition is assumed to take place without a change of the nuclear coordinates.

The Franck-Condon integral is the instantaneous overlap of nuclear wave functions in the initial and final electronic state and determines the probability for a transition between a vibrational level $|\mu\rangle$ of the electronic ground state and a vibrational level $|\nu\rangle$ of the final state. If (low-energy) phonon modes are neglected for the moment, the dominating vibrations that couple to the electronic states in CPs are the carbon – carbon bond stretching modes in the polymer backbone with an energy of about $1500\,\mathrm{cm}^{-1}$. The thermal energy at room temperature amounts to about $200\,\mathrm{cm}^{-1}$. Hence, it is a reasonable approximation that in thermal equilibrium only the vibrational ground state of the electronic ground state is populated, $|\mu\rangle = |0\rangle$ (i. e. the $T = 0\,\mathrm{K}$ limit is appropriate up to room temperature). In harmonic approximation the Franck-Condon factor can then be expressed in terms of a Poisson distribution [114]

$$F_{\nu 0} = |\langle\nu|0\rangle|^2 = \exp(-S)\frac{S^\nu}{\nu!}. \tag{2.8}$$

Here, S is the Huang-Rhys parameter that corresponds to the average number of vibrational quanta that are excited simultaneously with the electronic transition (because the expectation value of the Poisson distribution (2.8) is S). The Huang-Rhys parameter is also a measure for the mutual displacement of the equilibrium values of the potential energy surfaces between the electronic ground and excited state along the configuration coordinate of the corresponding vibration. For more normal modes J coupling to the electronic states, each with a Huang-Rhys parameter S_J, S is the total Huang-Rhys parameter and is given by $S = \sum_J S_J$. For $S = 0$ transitions into higher vibrational levels of the electronically excited state are not allowed. In this situation only the purely electronic (0-0) transition is allowed, i. e. the transition between the vibrational ground states of the involved electronic levels. For an increasing Huang-Rhys parameter the oscillator strength is redistributed from the purely electronic transition into the vibronic transitions, and for $S \gtrsim 5$ a 0-0 transition can no longer be observed. However, for CPs S is typically smaller than about 2 [20, 30, 47, 115].

It is convenient to introduce another useful molecular quantity, the one-photon (1P) absorption cross-section σ_1, which is proportional to the imaginary part of $\chi^{(1)}$ and thus

to the square magnitude of the transition dipole matrix element [111]:

$$\sigma_1 \propto \Im\{\chi^{(1)}\} \propto |\langle f|\hat{\mathbf{p}}|i\rangle|^2. \tag{2.9}$$

σ_1 is proportional to the probability for a chromophore to absorb a photon, and the number of photons N_{abs} a chromophore absorbs is proportional to the product of the 1P-absorption cross-section and the intensity of the incident light I_0 (in the absence of saturation effects, which are not considered here)

$$N_{\text{abs}} \propto \sigma_1 \cdot I_0. \tag{2.10}$$

σ_1 is of the order of $10^{-14}\,\text{cm}^2$ – $10^{-16}\,\text{cm}^2$ for CPs [33], which is representative for organic dyes [96].

It has been found that the linear susceptibility $\chi^{(1)}$ (or equivalently the transition dipole moment) increases with the conjugation length [23, 116–118]. Thus the absorption cross-section and consequently the number of absorbed photons increases for longer conjugation lengths for a given intensity of the incident light I_0.

Two-Photon Absorption

Two-photon (2P) absorption processes were first predicted by Maria Göppert-Mayer in 1931 by second order perturbation theory treatment of light-matter interactions [113] and are governed by the imaginary part of $\chi^{(3)}$. The full expression for the third order susceptibility is lengthy [23, 111, 112] and therefore not reproduced here. However, for the special case of 2P-absorption that is induced by incident light with a single frequency ω (one-colour 2P-absorption), the expression for the imaginary part of $\chi^{(3)}$ simplifies to [23, 111]

$$\Im\{\chi^{(3)}\} = \frac{\pi e^4}{3\varepsilon_0\hbar}\Big|\sum_v \frac{\langle f|\mathbf{n}\cdot\hat{\mathbf{p}}|v\rangle\langle v|\mathbf{n}\cdot\hat{\mathbf{p}}|i\rangle}{\omega-\omega_v}\Big|^2. \tag{2.11}$$

The summation in (2.11) is over all electronic levels of the molecule. The product of the transition dipole moments in eq. (2.11) describes the quasi-simultaneous interaction of two photons with a chromophore. The absorption of the first photon excites the molecule from the electronic ground state $|i\rangle$ into an intermediate or *virtual* state $|v\rangle$, which has an extremely short lifetime of about $10^{-15}\,\text{s}$. If a second photon is absorbed within the lifetime of the virtual level, the final excited state $|f\rangle$ is reached.

In analogy to the 1P-process, the two-photon absorption cross-section σ_2 is also proportional to $\Im\{\chi^{(3)}\}$, and is of the order of 10^{-46} – $10^{-49}\,\text{cm}^4\,\text{s}\,\text{per photon}$ for CPs [33, 35, 38, 119], which is comparable to values for organic dyes used in 2P-microscopy [120, 121]. Since the number of absorbed photons is

$$N_{\text{abs}} \propto \sigma_2 \cdot I_0^2, \tag{2.12}$$

high intensities of the incoming light I_0 of several tens of MW/cm^2 up to hundreds of GW/cm^2 are necessary to induce the 2P-process due to the small 2P-absorption cross-sections. The third order susceptibility in CPs increases with increasing conjugation length [23, 122], as the linear susceptibility. Therefore CPs are promising candidates for 2P-materials due to their high 2P-absorption cross-sections.

If the intermediate level involved in the 2P transition is a real electronic state of the molecule with a typical excited state lifetime of about 10^{-8} s the 2P absorption cross-section increases by orders of magnitude in analogy to the resonance Raman effect. However, this case will not be considered in this work.

Selection Rules and Molecular Symmetry

Selection rules determine whether an electronic or vibronic transition is optically allowed and takes place under absorption or emission of photons. In principle, this involves the explicit calculation of the transition dipole matrix elements in eqs. (2.3) and (2.11). A direct integration of these expressions is very tedious for larger molecules, because the wave functions of the initial and final electronic (vibronic) states have to be calculated from many body Hamilton operators (see section 2.1.2). However, if only a "digital" information is required, i. e. whether the transition dipole matrix elements vanish or not, and their absolute magnitude is not important, one can resort to simple spin and symmetry arguments.

Spin selection rules: The transition dipole moment operator (2.4) conserves the total spin. Hence an allowed electronic transition has to take place without a change of the total spin quantum number and singlet – triplet transitions are forbidden. However, as mentioned earlier in this section, in CPs intersystem crossing has been observed and arises from spin-orbit coupling, which mixes singlet and triplet states. In general electronic spin-orbit coupling, Herzberg-Teller vibrationally induced spin-orbit coupling, and vibrationally induced spin-orbit coupling by terms neglected in the Born-Oppenheimer approximation (non-BO spin-orbit coupling) can be distinguished [123–127]. For CPs electronic spin-orbit coupling is very small because of the lack of heavy atoms in these polymers. The relative contributions from the two vibrationally induced spin-orbit coupling mechanisms depend on the specific system under investigation. Herzberg-Teller spin-orbit coupling leads to $\pi - \pi$ coupling induced by in-plane vibrations, whereas non-BO spin-orbit coupling gives rise to $\sigma - \pi$ coupling owing to out-of-plane vibrations. The latter is particularly favoured in systems that deviate from planarity leading to $\sigma - \pi$ orbital mixing. This effect enhances the intersystem crossing rates and is likely to play a role in CPs with typically highly

disordered chain conformations.

Symmetry selection rules: The application of group theory is an elegant method to decide without direct calculation whether transitions between states with the same spin multiplicity are allowed. The first step in this approach is to classify the molecule into a point group, that determines which symmetry operations may be performed such that the the configuration of the molecule remains unchanged, i. e. such that the molecule looks the same after the transformation. There exist five symmetry (or transformation) operations [128]:

• identity element of symmetry I,

• centre of symmetry i: an inversion through the centre of symmetry, (x, y, z) $\rightarrow$ (-x, -y, -z), leaves the configuration unchanged,

• axis of symmetry C_m: the structure of the molecules does not change for a rotation by $2\pi/m$ about this axis,

• plane of symmetry σ: reflection across this plane does not change the configuration, the plane is labelled with a subscript h if this plane is perpendicular to the axis of symmetry C_m with the largest m; if the axis C_m with the largest m lies in the plane of symmetry, the plane is labelled with the subscript v,

• rotation-reflection axis of symmetry S_m: rotation by $2\pi/m$ about this axis and a subsequent reflection across a plane perpendicular to the S_m axis leaves the structure unchanged.

As an example for the assignment of a molecule to a point group, the structure of the monomer unit of LPPP is chosen (Fig. 2.5a). Besides the trivial symmetry element, the identity I, it is easily seen from a close inspection of this *ideal* geometry that this system possesses also a centre of inversion i which is in the centre of the central phenylene ring. Further, a twofold symmetry axis C_2 through the centre of inversion and perpendicular to the plane of the backbone is present, i. e. a rotation by 180^o about this axis leaves the structure unchanged. And finally, a plane of symmetry exists which is in the plane of the backbone, perpendicular to the C_2 axis, and therefore labelled σ_h. As a consequence of this, LPPP belongs to the point group C_{2h} [128] (further details about this point group can be found in Appendix A). It is convention for the C_{2h} point group that the z-axis of the coordinate system is defined by the C_2 axis, and the σ_h plane defines the x-y plane [128], see Fig. 2.5a. Note that it was arbitrarily chosen that the y-axis points along the backbone, an alternative choice of the coordinate system would be that the x-axis points along this direction (but the z-axis always has to be oriented perpendicular to the plane of the backbone). Other widely used conjugated polymers, such as PPVs and PDAs (Fig. 2.2), belong to the C_{2h} point group as well.

The generating elements of the C_{2h} point group are C_2 and i and the symmetry proper-

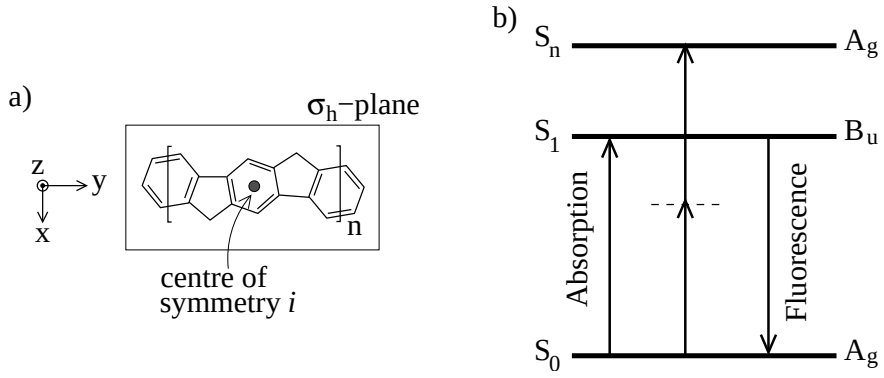

Figure 2.5: a) Chemical structure of LPPP and the conventional coordinate system for the C_{2h} point group: the σ_h plane defines the x-y plane, the C_2 axis (not shown), which is perpendicular to the σ_h plane and intersects this plane through the centre of inversion i, defines the z-axis. b) Simplified energy level scheme with the symmetry species for the three lowest singlet states S_0, S_1, and S_n. The dipole-allowed one- and two-photon transitions between these singlet levels are shown as arrows. The dashed line symbolises the intermediate state involved in the two-photon transition.

ties of the molecule are classified into symmetric and antisymmetric behaviour with respect to the transformations induced by these particular elements (see Appendix A). Symmetric (antisymmetric) behaviour with respect to the C_2 operation is denoted by the symbol A (B), while symmetric and antisymmetric behaviour with respect to the inversion i is labelled with the subscripts g and u, respectively. The latter symmetry property is also called parity. It follows that the C_{2h} point group has in total four *symmetry species* or *irreducible representations*, A_g, A_u, B_g, B_u, where the A_g species is the totally symmetric species and the remaining ones are non-totally symmetric.

Now, the wave functions of the electronic levels can be classified according to the symmetry species of the point group C_{2h} as well. To simplify the following discussion only purely electronic transitions will be considered. For CPs it has been found that the electronic singlet levels are of alternating even and odd parity with increasing energy, where the electronic ground state S_0 is a totally symmetric A_g level [21, 23, 25, 26]. This state is labelled as 1^1A_g where the first number enumerates the electronic levels with a particular symmetry species in order of increasing energy and the superscript denotes the spin multiplicity. The lowest excited singlet state S_1 has B_u symmetry, denoted as 1^1B_u, and the S_n state is again an even parity level (n^1A_g, see Fig. 2.5b).

For one-photon allowed purely electronic transitions the electronic dipole matrix element $\langle e_f|\hat{\mathbf{p}}|e_i\rangle$ [eq. (2.4)] has to be nonzero. In other words, the product of the wave

functions of the initial $|e_i\rangle$ and final electronic level $|e_f\rangle$ and the dipole moment operator $\hat{\mathbf{p}}$ has to be an *even* function of the electron coordinates such that the integral over this product does not vanish. The corresponding group theoretical expression states, that the product of the symmetry species of the involved wave functions and the dipole moment operator must be totally symmetric for at least one component of the transition dipole moment operator $\hat{p}_l$, $l = x, y, z$ [129]

$$\Gamma(|e_f\rangle) \times \Gamma(\hat{p}_l) \times \Gamma(|e_i\rangle) = A_g. \tag{2.13}$$

$\Gamma(\ldots)$ stands for the symmetry species of the quantity within parenthesis. The symmetry species of the components of the dipole moment operator in the C_{2h} point group are [129]

$$\Gamma(\hat{\mathbf{p}}) = \begin{pmatrix} B_u \\ B_u \\ A_u \end{pmatrix}. \tag{2.14}$$

The z-component of the transition dipole moment, i. e. the component perpendicular to the plane of the backbone, can be neglected for conjugated polymers. The only significant contribution to $\hat{\mathbf{p}}$ is oriented parallel to the y-axis along the backbone and the off-axis components (x- or y-components) are at least two orders of magnitude smaller [29, 87, 130], hence

$$\Gamma(\hat{\mathbf{p}}) = \begin{pmatrix} B_u \\ B_u \\ 0 \end{pmatrix}. \tag{2.15}$$

Note that the x- and y-axes are interchangeable as mentioned earlier, thus the x-component in eq. (2.15) has been retained. As a consequence, a 1P-absorption process from the electronic ground state S_0 with $\Gamma(|e_i\rangle) = A_g$ must end in a level with B_u symmetry, since the relation

$$\begin{array}{ccccccc} \Gamma(|e_f\rangle) & \times & \Gamma(\hat{p}_l) & \times & \Gamma(|e_i\rangle) & = & \\ \Gamma(|e_f\rangle) & \times & B_u & \times & A_g & = & A_g \end{array} \tag{2.16}$$

can be only satisfied for $\Gamma(|e_f\rangle) = B_u$.

For a purely electronic 2P-absorption process a similar symmetry selection rule can be derived from eq. (2.11) [129, 131]

$$\Gamma(|e_f\rangle) \times \Gamma(S_{lm}) \times \Gamma(|e_i\rangle) = A_g. \tag{2.17}$$

Here, S_{lm} $(l, m = x, y, z)$ stands for the components of the 2P-tensor, which resembles the polarisation tensor in Raman spectroscopy (which is also a 2P-process), and the symmetry

species of its components in the C_{2h} point group read [131]

$$\Gamma(S_{lm}) = \begin{pmatrix} A_g & A_g & 0 \\ A_g & A_g & 0 \\ 0 & 0 & 0 \end{pmatrix}. \tag{2.18}$$

Consequently, for a 2P-transition from the S_0 state, with $\Gamma(|e_i\rangle) = A_g$, relation (2.17)

$$\begin{array}{ccccccc} \Gamma(|e_f\rangle) & \times & \Gamma(S_{lm}) & \times & \Gamma(|e_i\rangle) & = & A_g \\ \Gamma(|e_f\rangle) & \times & A_g & \times & A_g & = & A_g \end{array} \tag{2.19}$$

can be only fulfilled for a final state with $\Gamma(|e_f\rangle) = A_g$, which is one of the higher singlet levels of CPs (Fig. 2.5b).

It follows that for conjugated polymers the $S_1 \leftarrow S_0$ transition (as well as transitions into higher singlet states with B_u symmetry) is one-photon allowed but 2P-forbidden and *vice versa* for transitions from the ground state into totally symmetric excited singlet states (Fig. 2.5b). Accordingly, fluorescence into the totally symmetric ground state S_0 can only occur from a level with odd parity, because fluorescence is also a 1P-process (Fig. 2.5b). Therefore, 1P- and 2P-spectroscopy are ideal, complementary tools to investigate the properties of electronically excites singlet states of CPs with different parity.

In chapter 4 the expressions for the symmetry selection rules (2.13) and (2.17) will be expanded to include vibronic 1P- and 2P-transitions. This will allow to derive the selection rules for vibronic transitions or alternatively to determine the symmetry species of the vibrational modes involved in vibronic 1P- and 2P-transitions. Additionally, it will be discussed to which extend the symmetry selection rules, as derived above for the *ideal* geometry of CPs, are still fulfilled in real disordered polymer samples.

2.2.3 Homogeneous Line Broadening and Electron-Phonon Coupling

While in section 2.2.2 only the "high-energy" intra-molecular modes of CPs (carbon bond stretch with an energy of about $1500\,\mathrm{cm}^{-1}$) have been considered, in the following the effect of low-energy modes (or phonons) with energies $\lesssim 200\,\mathrm{cm}^{-1}$ on the optical spectra of individual chromophores will be discussed.

In a two-level description of a purely electronic transition (e. g. $S_1 \leftrightarrow S_0$) of a chromophore the emission or absorption line shape is Lorentzian and the width (full width at half maximum, FWHM) is given by

$$\Gamma_{\mathrm{hom}}(T) = \frac{1}{2\pi T_1} + \frac{1}{\pi T_2^*(T)} = \frac{1}{\pi T_2(T)}, \tag{2.20}$$

which is known as homogeneous line width [111, 132, 133]. T_1 is the excited state lifetime, $T_2^*(T)$ denotes the temperature dependent pure dephasing time, and $T_2(T)$ stands for the total or effective dephasing time. The pure dephasing processes are caused by interactions with the environment (e. g. scattering with phonons) which lead to a fluctuation of the energy levels, but not to a variation of the population of the electronic states. This gives rise to a temperature dependent homogeneous broadening of the absorption and emission lines. At very low temperatures ($T \to 0$) the number of scattering events with phonons becomes very small, thus $T_2^* \to \infty$, and the line width of the optical transition is determined by the finite lifetime T_1 of the electronically excited state. In this limit $\Gamma_{\mathrm{hom}}(T)$ reflects the lifetime-limited, natural width of the spectral line.

An absorption or emission line as described above is also referred to as zero phonon line (ZPL) because the number of low-frequency modes is conserved in such a transition. In other words, the purely electronic transition takes place without creation or annihilation of low-energy vibrations of the chromophore or in its local surrounding.

Linear electron-phonon coupling gives rise to a purely electronic transition in combination with a simultaneous excitation of a low-energy vibration in the surrounding matrix or the CP backbone. Therefore, at low temperatures the ZPL in an emission (absorption) spectrum is accompanied by a shoulder in its low-energy (high-energy) wing [132], which is called the phonon side band (PSB, Fig. 2.6). The energy difference between the peak positions of the ZPL and PSB defines a mean phonon energy ω_m, which is characteristic of the energy of the (low-frequency) vibration coupled to the electronic state.

A measure for the linear electron-phonon coupling strength is provided by the Debye-Waller factor

$$\alpha(T) = \frac{I_{\mathrm{ZPL}}}{I_{\mathrm{ZPL}} + I_{\mathrm{PSB}}} = \exp\left(-S(T)\right), \tag{2.21}$$

where I_{ZPL} (I_{PSB}) denotes the integrated intensity of the ZPL (PSB). $S(T)$ is the temperature dependent Huang-Rhys parameter which was already introduced in eq. (2.8) for the high-energy ($1500\,\mathrm{cm}^{-1}$) vibrations, and can be derived accordingly for low-energy vibrations, because both are described as harmonic oscillators. However, in contrast to the high-energy modes, where the $T = 0\,\mathrm{K}$ limit is a reasonable approximation up to room temperature (see section 2.2.2), the thermal occupation of the phonon modes in the electronic ground state can not be neglected even at very low temperatures. Therefore, the temperature dependence of the Huang-Rhys parameter for phonon modes is explicitly retained in eq. (2.21). $S(T)$ is proportional to the average thermal occupation number of the phonon mode and increases for increasing temperatures [107]. Due to the exponential dependency of the Debye-Waller factor on the Huang-Rhys parameter [eq. (2.21)], $\alpha(T)$

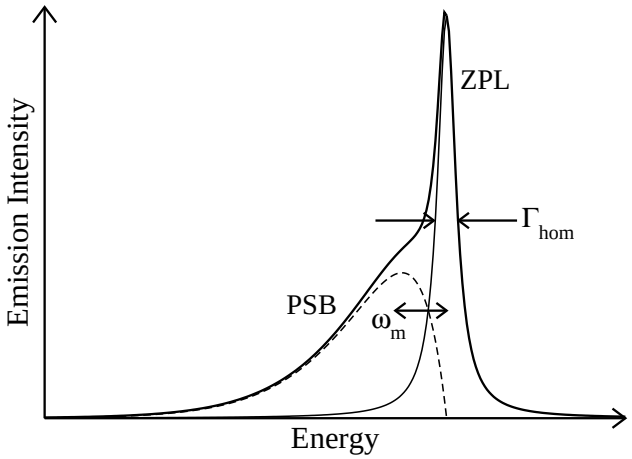

Figure 2.6: Schematic illustration of the fluorescence spectrum of a single chromophore at low temperatures (thick solid line): the homogeneously broadened (Γ_{hom}) zero phonon line (ZPL, thin solid line) is accompanied by a broad phonon side band (PSB, thin dashed line) in the low-energy wing, which is separated from the ZPL by the mean phonon energy ω_m.

and the intensity of the ZPL decreases rapidly at elevated temperatures. As a consequence of this, ZPLs can only be observed at very low (liquid helium) temperatures.

For conjugated polymers ZPLs with accompanied PSBs have not been observed in optical spectra. So far the effect of linear electron-phonon coupling to low-energy phonons (ring torsions, longitudinal acoustic modes of the backbone) has only been included in theoretical work to model ensemble spectra of CPs. From this a mean phonon energy between $60\,\mathrm{cm}^{-1}$ and $160\,\mathrm{cm}^{-1}$ and Huang-Rhys parameters (mostly calculated for room-temperature ensemble spectra) between 1 and 20 can be expected [20, 22, 76, 81, 88, 103], see also chapter 6.

2.2.4 Inhomogeneous Line Broadening and Spectral Diffusion

Conjugated polymers typically form amorphous samples [28], which are highly disordered and feature a random potential energy surface (sometimes CPs may be also partially crystalline or form crystals [28], such cases, however, are not relevant for this work). Therefore, each individual chromophore in such a sample has its own local environment which varies slightly from site to site. This causes a statistical distribution of the energy levels of the chromophores, reflecting the locally varying interaction potentials between the sites and their environments [106, 132, 133]. In addition, the HOMO – LUMO transition energy of a chromophore depends on its conjugation length. Hence, the distribution of conjugation lengths in a CP sample gives rise to statistically distributed HOMO – LUMO transition

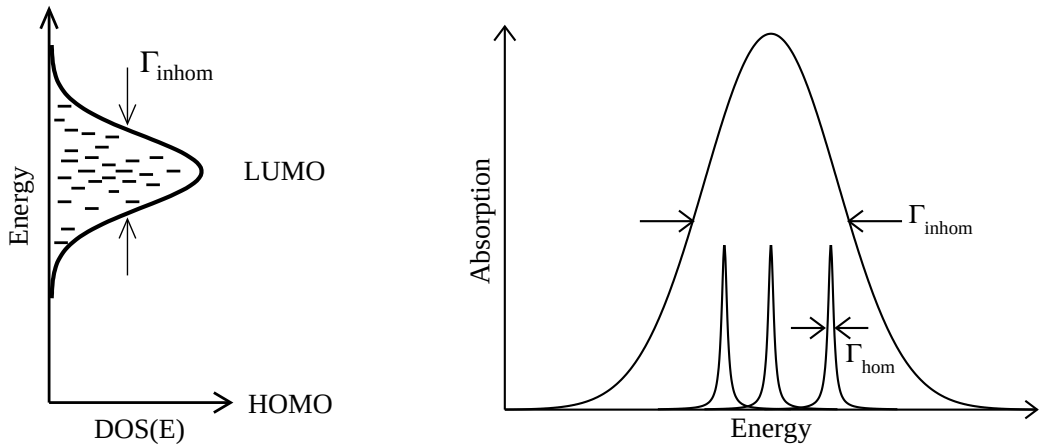

Figure 2.7: Varying local environments and a distribution of conjugation lengths lead to an inhomogeneously broadened distribution (density) of states (DOS) with a width of Γ_{inhom} (left). This causes a random shift of the absorption lines of the chromophores and gives rise to inhomogeneous broadening of an ensemble absorption spectrum (right).

energies (see section 2.1.3).

Both effects, the varying environments and the distribution of conjugation lengths, leads to an inhomogeneous distribution of site energies in the ground state and in the lowest electronically excited state (as well as in the higher excited levels). The inhomogeneously broadened bands observed in the absorption (and emission) spectra of bulk CP samples reflect the convolution of the site energy distributions in the ground and lowest excited state. This is schematically shown in Fig. 2.7, where the distribution of LUMO levels depicted on the left-hand side represents for simplicity the convolution of the distributions of the site energies in the HOMO and LUMO levels. For this the term *inhomogeneously broadenend distribution (density) of states* (DOS) has been established [29, 84, 85].

At low temperatures the width of the inhomogeneously broadened absorption (or emission) line is typically several orders of magnitude broader with respect to the width of the homogeneous line. At higher temperatures the increasing homogeneous line widths of individual chromophores [54, 134] significantly contribute to the observed line width of the ensemble spectra as well.

In addition to static processes as described above, dynamic processes in the local environment also influence the energy levels of the chromophores. These effects are especially important in amorphous solids, since these are not in thermodynamic equilibrium below the glass transition temperature and show structural relaxation processes even at very low temperatures. The standard model for amorphous solids at low temperatures [135,136] pro-

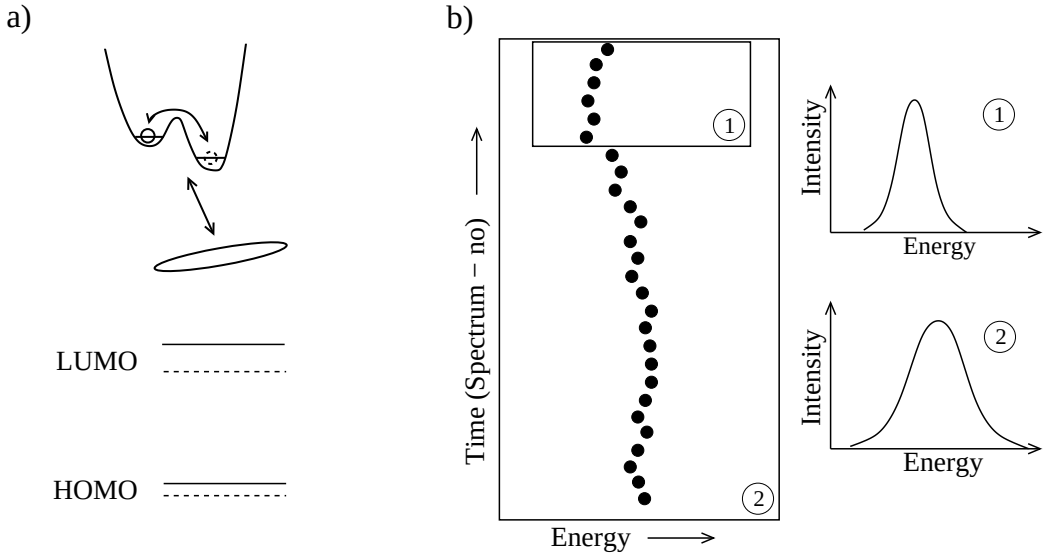

Figure 2.8: a) Schematic representation of a single chromophore interacting with a flipping two-level system (TLS) in its local environment (top). A flip between the metastable equilibrium positions of the TLS leads to a different shift of the HOMO and LUMO levels of the chromophore and consequently to a changed energy gap between these states (bottom). b) Spectral diffusion trail of the emission (absorption) line of a chromophore (left), which exhibits gradual drifts or sudden jumps of the spectral line due to interactions with flipping TLSs in the surrounding. Different temporal resolutions of a hypothetic single-molecule measurement are indicated by the boxes marked with ① and ②, and the resulting single-molecule spectra are shown to the right. Depending on the temporal resolution the spectra may differ in line widths and centre positions.

poses the existence of randomly distributed localised degrees of freedom to model the properties of amorphous systems (specific heat, thermal conductivity, etc.), which are markedly different from those of crystals. The localised low-energy vibrations are approximated by asymmetric double-well potentials, the so-called two-level systems (TLS, Fig. 2.8a). The nature of the TLSs is unknown for most materials. It is generally assumed that groups of atoms or molecules of the material flip between two metastable equilibrium positions. If such temporal fluctuations occur in the vicinity of a chromophore this leads to changes of the local interactions, which are typically assumed to be of dipole – dipole character, and as a consequence, this results in temporal variations of the energy levels of the chromophore (Fig. 2.8a).

In amorphous systems at liquid helium temperatures these fluctuations or TLS flips occur on all time scales up to several days or weeks. Generally, two time scales can be distinguished: (i) Fluctuations faster than the excited state lifetime T_1 of the chromophore contribute to the pure dephasing time T_2^* and thus to the homogeneous broadening of

the ZPL. (ii) Fluctuations slower than T_1 lead to sudden jumps or gradual drifts of the energy levels of a chromophore. In principle, this can be followed in a single-molecule experiment where many spectra of the same chromophore are recorded consecutively. If these spectra are stacked on top of each other, the spectral position of the ZPL (and the possibly associated PSB) can be followed as a function of time (Fig. 2.8b). This so-called "spectral diffusion trail" allows to derive information about the magnitude and time scales of the fluctuations of the energy levels of the chromophore.

Within the *sudden jump model* it is assumed that a TLS-flip leads instantaneously to a shift of the energy levels of a chromophore via a dipolar TLS – chromophore interaction [137]. This causes a relative change of the spectral position $\Delta\nu$ of the emission (or absorption) line of the chromophore, which is given by [137]

$$\Delta\nu = 2\pi K \frac{A}{E}\frac{\kappa}{R^3}. \tag{2.22}$$

Here, K is the chromophore – TLS coupling constant which is specific for the particular guest – host system, A and E are the asymmetry and energy splitting, respectively, of the TLS interacting with the chromophore, and κ accounts for the mutual orientation between the elastic or electric dipole moment associated with the fluctuating matrix unit and the dipole moment of the chromophore. R is the distance between the TLS and the chromophore. Therefore the analysis of the spectral diffusion trail of a single chromophore permits to gain insight into variations of the local interactions between the chromophore and the TLS and finally allows to retrieve information about the nano-environment of the chromophore.

However, the acquisition of each single-molecule spectrum requires an integration time of usually several hundreds of milliseconds up to several seconds due to a typically weak fluorescence signal of a single chromophore. Therefore, fluctuations faster than the temporal resolution of the measurement can not be resolved. This gives rise to an apparent line broadening of the ZPL of an individual chromophore, which is an inhomogeneous broadening mechanism. In a single-molecule experiment this shows up as a ZPL with a line width that depends on the temporal resolution of the measurement [56, 138], as sketched schematically in Fig. 2.8b.

Spectral diffusion processes can be theoretically described within the framework of the *spectral diffusion kernel* [139,140]. The spectral diffusion kernel is defined as the conditional probability distribution that the energy of an electronic transition (the spectral position of an emission/absorption line) is E at time t if it had an energy of E_0 at an earlier time t_0. Two limiting cases for the spectral diffusion kernel can be distinguished that predict a Lorentzian and Gaussian line shape for ZPLs, respectively. The first limit corresponds to

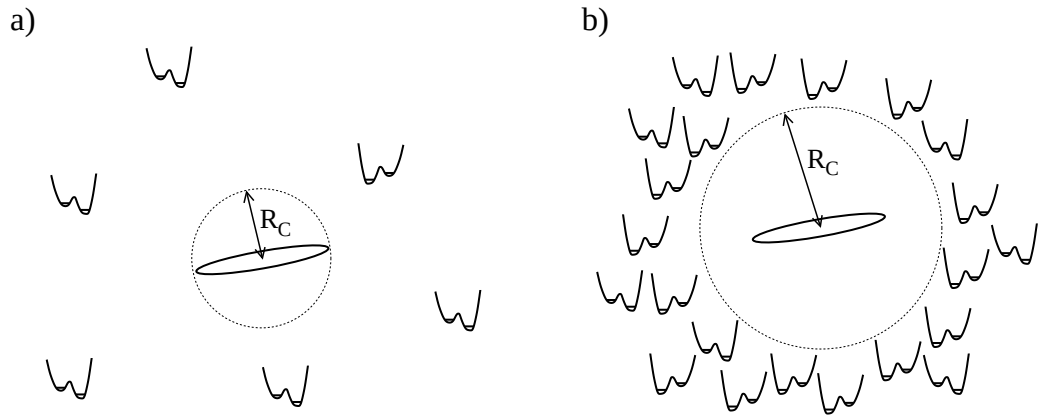

Figure 2.9: Limiting cases for the calculation of the spectral diffusion kernel. a) In the standard two-level system (TLS) model the chromophore resides in a cavity (dashed circle) with a radius R_c smaller than the average distance between the TLS. b) In the "Gaussian" limit the radius R_c of the excluded volume around a chromophore is large with respect to the average distance between the TLS.

the standard model for amorphous solids and it is assumed that the chromophore resides in a cavity which contains no TLSs (Fig. 2.9a). The radius of this excluded volume R_c is comparable to or smaller than the average distance between the TLSs. If the interaction between the TLSs and the chromophore is taken to be of dipole-dipole type, the ZPL line shape, broadened by spectral diffusion, is predicted to be Lorentzian [139–141]. In the second limit, the chromophore sits in a cavity with a radius R_c that is large with respect to the average distance between the TLSs (Fig. 2.9b). It was found that the resulting line shape of the ZPL is Gaussian irrespective of the form of the interaction potential between the TLSs and the chromophore [141].

Besides these predictions within the concept of the spectral diffusion kernel another peculiar *triangular* line shape was proposed for a situation where the measured emission (absorption) line results from averaging over ZPLs which exhibit a (inhomogeneous) distribution of line widths [132].

2.3 Excitation Energy Transfer

Excitation energy transfer within the inhomogeneously broadened distribution of excited states (DOS) is a very important process in conjugated polymers, see Refs. [21–23, 30, 75, 142] for reviews. This process is typically described by resonant energy transfer between pairs of chromophores, where one chromophore, initially in the lowest electronically excited

state S_1 (LUMO), is deactivated into the ground state S_0 (HOMO), while a second site, initially in the ground state, is excited into the lowest excited state. The excitation energy transfer between two chromophores n and m is mediated by Coulomb interactions

$$V(nm) = \frac{1}{4\pi\varepsilon_0} \sum_{\substack{j,k \\ j\neq k}} \frac{e^2}{|\mathbf{R}_{nm} + \mathbf{r}_j(n) - \mathbf{r}_k(m)|}, \tag{2.23}$$

where $\mathbf{R}_{nm} = \mathbf{R}_n - \mathbf{R}_m$ is the centre of mass distance between site n and m. $\mathbf{r}_j(n)$ $[\mathbf{r}_k(m)]$ stands for the position of the j^{th} (k^{th}) electron on site n (m) relative to the centre of mass position of site n (m).

A conjugated polymer sample is modelled by an assembly of N chromophores with an average excited state energy (HOMO – LUMO gap) of E_0. In Heitler-London approximation the Hamilton operator for this system reads

$$H = \sum_{n=1}^{N} E_0 |n\rangle\langle n| + \sum_{\substack{n=1,m=1 \\ n\neq m}}^{N} W_{nm} |n\rangle\langle m|, \tag{2.24}$$

where $|n\rangle$ describes the presence of an electronic excitation localised on site n and all other chromophores (1, 2, ... n-1, n+1, ... N) are in the ground state. The transfer integral W_{nm} is given by:

$$W_{nm} = \langle n|V(nm)|m\rangle = J_{nm} - K_{nm}. \tag{2.25}$$

Together with eq. (2.23) this shows that the direct or Coulomb transfer integral J_{nm} is responsible for the excitation energy transfer of singlet excitations, because the electronic ground state is a singlet state and the total spin is preserved. The exchange integral K_{nm} mediates the transfer of triplet excitations and charge carriers [23, 24]. Since this latter matrix element decreases exponentially with distance, its contribution to the total transfer integral is very small. Additionally, only the transfer of singlet excitations is considered in the following, and hence the exchange interactions are neglected.

If the size of a chromophore is much smaller than the distance between the sites, the dipole approximation is valid, i. e. the Coulomb potential (2.23) is expanded up to second order terms, and the direct transfer integral can be written as

$$J_{nm} = \kappa_{nm} \cdot \frac{{}_n\langle 0|\hat{\mathbf{p}}_n|n\rangle \cdot \langle m|\hat{\mathbf{p}}_m|0\rangle_m}{|\mathbf{R}_{nm}|^3}, \tag{2.26}$$

where $\hat{\mathbf{p}}_n$ ($\hat{\mathbf{p}}_m$) is the electronic dipole moment operator for site n (m), as defined in eq. (2.5). $|0\rangle_n$ ($|0\rangle_m$) denotes the ground state wave function of chromophore n (m). The orientational factor κ_{nm} reads

$$\kappa_{nm} = \mathbf{e}_n \cdot \mathbf{e}_m - 3(\mathbf{E}_{nm} \cdot \mathbf{e}_n)(\mathbf{E}_{nm} \cdot \mathbf{e}_m). \tag{2.27}$$

The units vectors $\mathbf{e}_n$ ($\mathbf{e}_m$) and $\mathbf{E}_{nm}$ point into the directions of the transition dipole moment $\hat{\mathbf{p}}_n$ ($\hat{\mathbf{p}}_m$) and the distance vector $\mathbf{R}_{nm}$, respectively. κ_{nm} accounts for different mutual orientations of the transition dipole moments of sites n and m and is between $\kappa_{nm} = 0$ for perpendicularly oriented transitions dipole moments and $\kappa_{nm} = 4$ for a collinear head-to-head arrangement of the transition dipole moments.

The direct transfer integral (2.26) describes the interaction between the transition dipole moments on sites n and m, both of which are non-zero only for dipole-allowed transitions, see section 2.2.2. An expansion of the Coulomb potential (2.23), which includes higher order multipole terms, accounts for the transfer of dipole-forbidden singlet excitations.

For the further discussion the limits of incoherent and coherent transfer will be distinguished. The former is a proper description if the excitation energy transfer (with time constant τ_T) is slower than inter- or intra-molecular relaxation processes (with time constant τ_{rel}) such as vibrational relaxation, i. e. $\tau_T \gg \tau_{\mathrm{rel}}$. For coherent energy transfer the opposite situation, $\tau_T \ll \tau_{\mathrm{rel}}$, applies. The transfer time τ_T can be shown to be proportional to $\hbar/J_{nm}$ [23]. Typically, the energy transfer in conjugated polymers with transfer times longer than about 200 fs, which corresponds to the vibrational relaxation time [39, 42, 108], can be modelled by incoherent transfer, while on shorter time scales coherent contributions have to be included [23, 143].

2.3.1 Incoherent Energy Transfer

In the incoherent limit the energy transfer is described by a rate equation, the (Pauli) master equation, which yields the time-dependent probability $P_n(t)$ of finding an excitation on chromophore n at time t [22–24, 41, 42, 144]

$$\frac{\partial P_n(t)}{\partial t} = -\sum_m \Big(k_{nm} P_n(t) + k_n P_n(t) - k_{mn} P_m(t) \Big). \tag{2.28}$$

k_n is the decay rate of chromophore n into the electronic ground state in the absence of transfer processes. The first (third) term on the right-hand side represents the decay of the probability $P_n(t)$ [$P_m(t)$] due to transfer of an electronic excitation from site n to m (m to n) with transfer rates k_{nm} (k_{mn}). The transfer rate k_{nm} is calculated by Fermi's Golden Rule

$$k_{nm} = \frac{2\pi}{\hbar} |J_{nm}|^2 \cdot I_{nm}, \tag{2.29}$$

where I_{nm} denotes the spectral overlap between the emission spectrum of the "donor" site n and the absorption spectrum of the "acceptor" site m.

Inserting the direct transfer integral in dipole approximation [eq. (2.26)] into eq. (2.29) leads to the well-known expression for the transfer rate derived by Förster [145]

$$k_{nm} = \frac{1}{\tau_{\mathrm{rad}}} \Big(\frac{R_F}{|\mathbf{R}_{nm}|} \Big)^6, \tag{2.30}$$

with the radiative excited state lifetime τ_{rad} and the Förster radius R_F, that defines the inter-site distance at which the transfer efficiency is 50 %.

The master equation approach with Förster-type transfer rates has been widely used to model the energy transfer within the DOS in conjugated polymers [40–42, 142, 144]. The excitation energy of each chromophore E_n ($n = 1, \ldots \mathrm{N}$) was randomly chosen from a Gaussian distribution centred around the average value E_0 to consider the influence of static disorder and the distribution of conjugation lengths on the excitation energy of individual chromophores (Fig. 2.10, left). In order to account for thermally activated transfer of excitations to energetically higher lying chromophores within the DOS at elevated temperatures ("uphill" transfer), the transfer rates as defined in eq. (2.30) are additionally weighted by a Boltzmann factor ϑ, i. e. $k_{nm} \rightarrow \vartheta k_{nm}$ with

$$\vartheta = \begin{cases} \exp\Big(-\frac{E_m - E_n}{k_B T} \Big) & \text{for} \quad E_m > E_n, \\ 1 & \text{for} \quad E_m \leq E_n. \end{cases} \tag{2.31}$$

The results of this modelling in the incoherent regime can be visualised by an energy dispersive hopping of electronic excitations towards energetically lower lying sites within the DOS prior to radiative or non-radiative decay into the electronic ground state (Fig. 2.10). In particular, it was found that the transfer within the DOS is a function of both the time and the energy of the excitation within the DOS. That is, the transfer process slows down (the transfer rate decreases) the longer an excitation "survives" in the DOS due to a decreasing number of possible lower energy sites in its local environment. Finally, at the lowest energies within the DOS the decay into the ground state is the dominating process because the transfer rate becomes smaller than the decay rate into the ground state. Hence, an energy-dependent excited state lifetime as well as a transient red-shift of the fluorescence spectrum is expected.

These intra-DOS relaxations of electronic excitations prior to the emission process were found to give rise to the narrower line widths observed for the emission spectra of bulk CP-samples with respect to the corresponding line widths of the absorption spectra. In addition, a large contribution to the Stokes shift between the purely electronic transitions in the absorption and emission spectra of CPs comes from intra-DOS excitation energy transfer processes to lower lying sites within the DOS [29, 30, 39, 47].

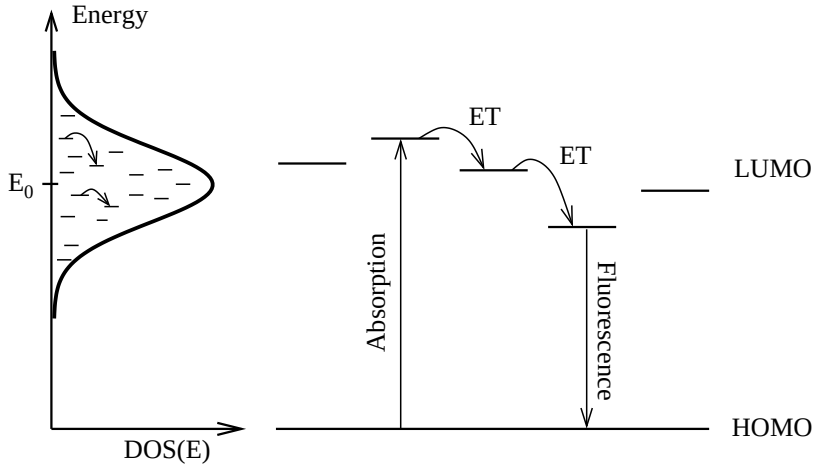

Figure 2.10: Schematic illustration of the excitation energy transfer (ET) within the inhomogeneously broadened distribution of electronically excited states (DOS). For details see text.

However, calculating the transfer rates by the Förster expression [eq. (2.30)] has two shortcomings. First, for CPs the size of the chromophores is not small with respect to the inter-site distances and therefore the point-dipole approximation is not appropriate. The spatial extend of the wave functions of the electronic states has to be included in the calculation of the transfer integral and hence of the transfer rates in eq. (2.29) [20,22,77,82,146]. Recent theoretical work beyond the point-dipole approximation accounted for the size and quasi one-dimensional structure of the chromophores by several approaches, such as the distributed monopole method [20,22,82] and the line dipole method [77]. Second, the spectral overlap I_{nm} in eq. (2.29) between the emission spectrum of the donor and absorption spectrum of the acceptor site is unknown and has to be estimated. Since the spectral overlap between the corresponding homogeneously broadened spectra is required [23, 24] and the homogeneous line width in CPs is still a matter of debate [20,54,56,91,134], single-molecule spectroscopy can yield important insights and provide more precise numbers (see chapter 6). Note that calculations based on the more sophisticated methods (distributed monopole and line dipole methods) also suffer from the basically unknown spectral overlap between donor and acceptor sites.

Despite these shortcomings the simple approach as discussed above (using Förster-type transfer rates in the master equation) was found to describe the intra-DOS relaxation processes reasonably well [146] and all experimental results from time-resolved spectroscopy could be modelled successfully [40–42, 142, 144]. Some predictions of this model have not been observed so far (see chapter 5).

Very important parameters, that are crucial to achieve a detailed understanding of

excitation energy transfer processes and that strongly influence the efficiency of these processes, are the electron-phonon coupling strength as well as the energies of the vibrational and phonon modes that are coupled to the electronic states [20, 22, 24, 147]. Especially the so-called relaxation or reorganisation energy ϵ, defined as

$$\epsilon = S\hbar\omega, \tag{2.32}$$

governs the excitation energy transfer rates, which are the higher the smaller this energy is [22, 24, 147]. In eq. (2.32) S is the Huang-Rhys parameter and $\hbar\omega$ is the energy of the vibration or phonon mode that couples to the electronic level. If several vibrational modes couple to the electronic states, the total reorganisation energy can be expressed as the sum of the relaxation energies of all modes [22, 24]. The reorganisation energy arises from electronic and nuclear relaxation of the chromophore or the surrounding medium into a new equilibrium configuration after photoexcitation of the chromophore, or *vice versa* relaxation into the ground state configuration after transition into the electronic ground state [22, 24]. In recent theoretical work low-energy phonon modes (ring torsions or longitudinal acoustic modes with energies $\lesssim 160\,\mathrm{cm}^{-1}$) have been included to model the excitation energy transfer processes in CPs [22, 103]. It has been found that significant electron-phonon coupling strength of these modes strongly reduces the transfer rates as compared to the situation where these phonons are absent [22]. However, the Huang-Rhys parameters and the energies of these low-frequency phonon modes and hence their relaxation energies have not been determined experimentally for conjugated polymers (see chapter 6).

2.3.2 Coherent Energy Transfer

In contrast to the incoherent regime, where the excitation energy transfer was described by a rate equation [eq. (2.28)], in the coherent limit the dynamics has to be determined from the solution of the time-dependent Schrödinger equation

$$i\hbar\frac{\partial|\Psi(t)\rangle}{\partial t} = H|\Psi(t)\rangle, \tag{2.33}$$

with the Hamiltonian defined in eq. (2.24) and the wave function

$$|\Psi(t)\rangle = \sum_n a_n(t)|n\rangle. \tag{2.34}$$

The square magnitude of the time dependent coefficients, $|a_n(t)|^2$, then yields the probability of finding the excitation on chromophore n at time t.

Only very recently these coherent motions of excitations in conjugated polymers have been investigated theoretically to account for ultra-fast intra-DOS relaxation processes on time scales $\lesssim 200\,\mathrm{fs}$, for which the modelling by incoherent transfer processes failed [143].

Chapter 3

Experimental

In this chapter the properties of the investigated π-conjugated polymer, methyl-substituted ladder-type poly(*para*-phenylene) (MeLPPP), will be briefly reviewed and the sample preparation for the various experiments will be described. Then an overview of the versatile setup will be given that was realised during this work to perform two-photon fluorescence excitation, time-resolved, as well as single-molecule fluorescence spectroscopy on MeLPPP.

3.1 Sample

3.1.1 Methyl-Substituted Ladder-Type Poly(*para*-Phenylene)

The π-conjugated polymer investigated in this work is a methyl-substituted ladder-type poly(*para*-phenylene) (MeLPPP) with a number average molecular weight of $M_n = 55300$ and a polydispersity of 3, which was synthesised by Prof. U. Scherf (Universität Wuppertal) [7, 64]. The chemical structure of MeLPPP together with the absorption and emission spectra of a thin MeLPPP-film both at room temperature and at 1.5 K are depicted in Fig. 3.1.

MeLPPP is an ideal model system for the study of conjugated polymers, because it features high thermal, chemical, and mechanical stability with a high degree of intra-chain order owing to the rigid, rod-like ladder-type backbone. This ladder-structure is characterised by two bonds, a carbon – carbon bond and a methylene bridge between neighbouring phenylene-rings in the polymer backbone (see Fig. 3.1a). Therefore, this polymer is also referred to as *double stranded* polymer [7]. The ladder-structure leads to a well-defined geometry with few chemical and/or conformational defects and thus to a narrow distribution of conjugation lengths between 5 and 10 repeating units [33, 148–151].

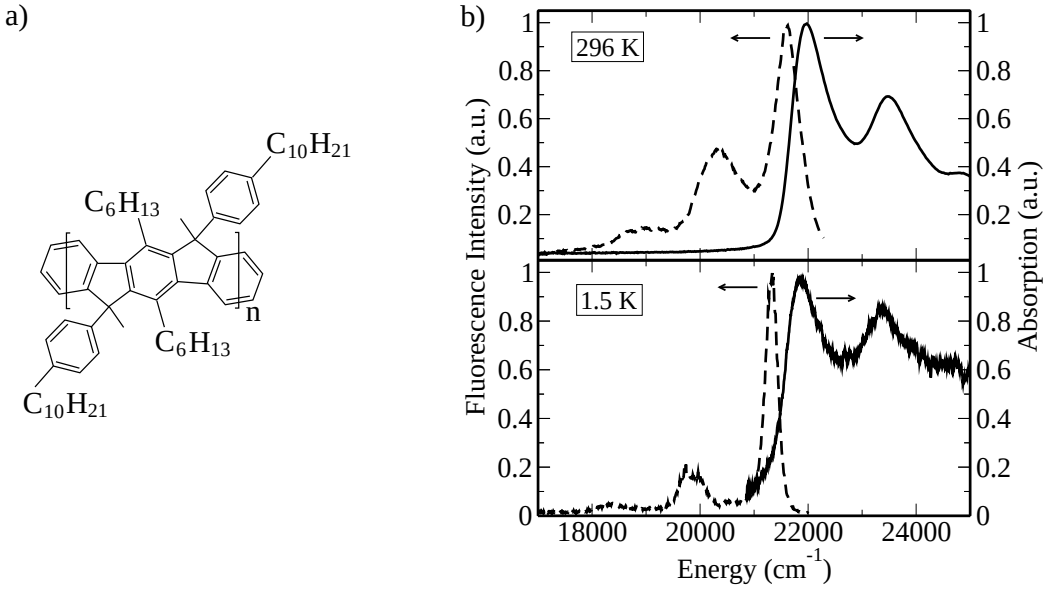

Figure 3.1: a) Chemical structure of methyl-substituted ladder-type poly(*para*-phenylene) (MeLPPP). b) Absorption (solid lines) and emission spectra (dashed lines) of an MeLPPP-film measured at room temperature (top) and at 1.5 K (bottom).

From the number average molecular weight of $M_n = 55300$ of the investigated MeLPPP-samples it can be estimated that an MeLPPP-chain comprises about 70 – 80 repeating units. Given the mean conjugation length of about 7 – 8 repeating units, each polymer chain contains about 10 chromophores.

As a consequence of the narrow distribution of conjugation lengths, a relatively narrow inhomogeneous line width of 690 cm^{-1} (FWHM) at room temperature and 635 cm^{-1} (FWHM) at 1.5 K is determined from the corresponding absorption spectra (Fig. 3.1b). Owing to the narrow inhomogeneous ensemble line widths a well-resolved vibronic progression can be observed in both the absorption and fluorescence spectra of MeLPPP-films. The vibronic bands arise from carbon – carbon stretching modes with an energy of about 1500 cm^{-1} [152] and their overtones that are coupled to the electronic states.

The fluorescence spectra of MeLPPP exhibit line widths of 600 cm^{-1} (FWHM) at room temperature and 230 cm^{-1} (FWHM) at 1.5 K, respectively. The narrower line width of the low-temperature emission spectrum with respect to the room-temperature emission spectrum is ascribed to fast intra-DOS relaxation processes of electronic excitations prior to the emission process (see chapter 5).

Additionally, MeLPPP is characterised by high fluorescence quantum yields of 25 % in films and 80 % in solution [62, 63] (both at room temperature) and 60 % in films at

5 K [62]. This makes MeLPPP an excellent candidate for applications as active material in blue-green organic light-emitting diodes and optically pumped organic polymer lasers [5,7].

The Stokes shift, i. e. the energy difference between the purely electronic transitions of the absorption and emission spectra, is only about 300 cm^{-1} at room temperature and about 500 cm^{-1} at 1.5 K. This Stokes shift is small with respect to other conjugated polymers and reflects the rigid, ladder-type structure of MeLPPP which does not allow for large structural changes between the ground and excited states (Ref. [7] and chapter 6).

The long and flexible side groups bound to the MeLPPP-backbone ensure a high degree of solubility in most organic solvents and hence this polymer can be easily processed from solution [7]. In addition MeLPPP features an excellent miscibility with inert polymers such as polystyrene. The attachment of the CH_3 (methyl) group instead of an hydrogen substituent in the methylene bridge (i. e. going from hydrogen-substituted LPPP to methyl-substituted LPPP) turned out to have a major influence on the optical spectra of ladder-type polymers. This substitution strongly suppresses the formation of emissive keto-defects [7, 153, 154], that lead to a dominant, structureless defect emission band in the yellow-green spectral region superimposed onto the fluorescence spectrum of the polymer [7, 108, 153, 155, 156]. However, even methyl-substituted LPPP has still a slight tendency to form emissive keto-defects under continuous illumination in the presence of molecular oxygen [153, 154], which prevented to elucidate many intrinsic optical and electronic properties of this ladder-polymer as yet (see e. g. chapter 5). Therefore, the exposure of the MeLPPP samples to molecular oxygen was avoided during the sample preparation and in particular during the measurements to prevent the formation of keto-defects. In the optical spectra presented in Fig. 3.1b indications of a broad and structureless defect emission band do not appear.

3.1.2 Sample Preparation

For the two-photon fluorescence excitation measurements MeLPPP was dissolved in toluene at a concentration of 10^{-6} mol/L. Thin films were prepared by drop-casting 10 μl from this solution onto a quartz substrate. These samples were mounted on the piezo-stage of a home-built inverted confocal microscope and held under a nitrogen atmosphere in order to avoid photodegradation during the measurements.

The samples for the time-resolved experiments were prepared analogously by drop-casting 10 μl from the 10^{-6} mol/L MeLPPP/toluene solution onto a quartz substrate. These films were mounted in a liquid-helium bath-cryostat and either cooled to 1.5 K or held in a helium atmosphere at room temperature to avoid sample degradation during the

experiment.

For the single-molecule experiments MeLPPP was predissolved in toluene at typical concentrations of 20 nM and dispersed in an inert matrix. As matrix materials either *n*-hexadecane (HD), which usually forms a Shpol'skii matrix upon fast cooling [157–159], or polystyrene (PS), which provides an amorphous host, has been chosen. For the preparation of the MeLPPP-HD samples the MeLPPP-toluene solution was further diluted in HD by a factor of about 100 and a drop of this solution was sandwiched between a quartz substrate and a quartz cover slip. Adhesion forces lead to the formation of a thin film with a thickness of several μm. This sample was quickly inserted in a liquid-helium bath-cryostat, that was precooled to about 80 – 90 K with liquid nitrogen, and further cooled to 1.5 K with liquid helium. For the MeLPPP-PS samples at first PS was dissolved in toluene and then the MeLPPP-toluene solution was diluted with this PS-toluene solution by a factor of 100. The resulting MeLPPP-PS-toluene solution was spin-coated on a quartz-substrate, which produces high-quality amorphous films with a thickness of several hundred nm. Finally, this sample was mounted in a liquid-helium bath-cryostat and cooled to 1.5 K.

3.2 Experimental Setup

3.2.1 General Remarks

The spectroscopic techniques applied in this work comprise two-photon (2P) fluorescence excitation spectroscopy, time-resolved spectroscopy, and single-molecule (SM) fluorescence spectroscopy. Employing these techniques to characterise the electronic states of MeLPPP requires different prerequisites to be fulfilled: for the 2P experiments a tunable light source in the near infrared spectral region (about twice the absorption wavelength of MeLPPP, Fig. 3.1b) is necessary. In addition, the light source must provide high (peak) powers to induce the 2P absorption process due to the low 2P absorption cross-sections (see section 2.2.2). The time-resolved experiments are performed with a pulsed excitation light source. Finally, time-resolved as well as single-molecule fluorescence spectroscopy necessitates an excitation source operating below 440 nm for excitation into the first vibronic transition of MeLPPP (see Fig. 3.1). This allows for sufficient spectral separation between excitation and fluorescence light to acquire the whole fluorescence spectrum (of single chains in SM experiments).

Both 2P and SM experiments require tight focussing of the excitation light into the sample. For 2P spectroscopy this allows to achieve the high excitation intensities at the sample, whereas in single-molecule experiments this permits to reduce the background

signal, because this is proportional to the illuminated sample volume. Therefore the experimental setups are based on confocal microscopes with objectives with high numerical apertures (NA ≥ 0.85). This permits to focus the excitation light to a diffraction limited spot size of about 300 – 680 nm (FWHM) depending on the excitation wavelength and the NA of the objective. Given the thickness of the samples used in this work of about 1 μm this corresponds to a focal volume of the order of 1 μm^3.

All spectroscopic techniques employed in this work rely on the detection of the fluorescence signal of MeLPPP. Therefore, the detectors have to be sensitive in the spectral region between 450 – 550 nm. In particular, single-molecule fluorescence spectroscopy requires very sensitive detectors to observe the weak and additionally spectrally dispersed fluorescence signal.

Additionally, the experiments were conducted both at room temperature and at cryogenic temperatures (1.5 K), and thus a liquid-helium bath cryostat had to be integrated in the setup as well. Going to low temperatures has several advantages particularly for SM spectroscopy. First, the photophysical and photochemical stability of the conjugated polymers is strongly enhanced. This allows to record the fluorescence signal of single chains for several minutes up to hours. Second, the homogeneous broadening of the spectral lines of single chromophores is significantly reduced due to a freezing-out of dephasing processes at cryogenic temperatures.

Because all experiments described in this thesis were performed on a single experimental setup, except for the two-photon measurements described in chapter 4, a flexible and versatile setup based on a confocal microscope was realised. The primary light source was a Titanium:Sapphire laser, that was either used directly for excitation of the sample with light in the near infrared spectral region. Alternatively, this laser was used to pump various frequency doubling units that provide excitation light in the blue/near ultraviolet spectral region. For the detection an avalanche photodiode, a sensitive charge-coupled device (CCD) camera in combination with spectrographs, or a streak camera system was available. The use of mirrors attached to flip mounts permitted to switch between the various excitation and detection schemes within short time (typically several minutes), and therefore allowed to characterise the same sample with different methods.

3.2.2 Excitation Light Sources

The excitation light sources with the corresponding optical path is presented in Fig. 3.2. The elements will be described in more detail below.

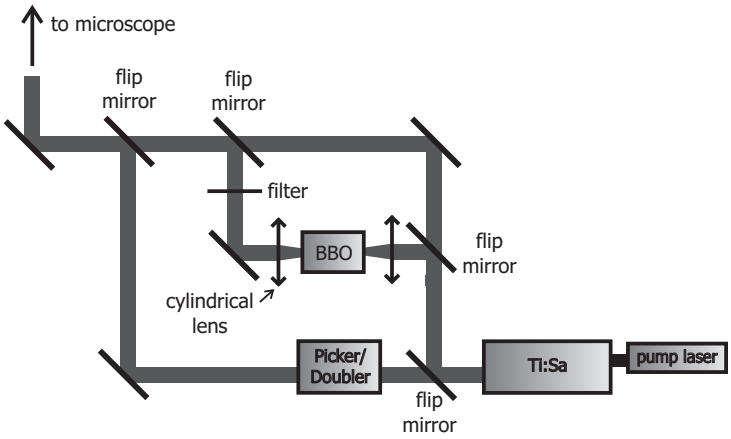

Figure 3.2: Schematic illustration of the excitation light path with the Titanium:Sapphire (Ti:Sa) laser system and the two frequency doubling units.

Titanium:Sapphire Laser System

The main excitation source was a Titanium:Sapphire (Ti:Sa) laser system (Tsunami, Spectra Physics) which is pumped by a continuous-wave Neodymium-Yttrium-Vanadate ($Nd:YVO_4$) laser (Millennia Xs, Spectra Physics) at 532 nm with up to 10 W. This permitted to achieve (time averaged) output powers of the Ti:Sa of about 3 W at the peak wavelength ($\approx$ 780 nm) of the Ti:Sa gain curve. The Ti:Sa laser is equipped with a broadband mirror set and any emission wavelength in the near infrared spectral region between 700 nm and 1000 nm is accessible. The emission wavelength can be adjusted by rotating the intra-cavity birefringent filter with a motorised, computer-controlled micrometre screw (M-227 DC-Mike, Physik Instrumente). The wavelength dependent output power of the Ti:Sa-laser was monitored with a powermeter (Model 407A, Spectra Physics). The laser system can be operated in both pulsed and continuous-wave mode.

Pulsed Mode: For time-resolved (chapter 5) and single-molecule (chapter 6) experiments the Ti:Sa was operated in pulsed mode, where pulses with a width of 1.5 ps (FWHM) and a repetition rate of 80.75 MHz are provided. In the picosecond mode the passive mode-locking by the optical Kerr-effect in the Ti:Sa crystal is rather inefficient, because the peak power is too low. Therefore, mode-locking is actively supported by an acousto-optical modulator (AOM). To ensure stable pulsing at any given wavelength in the tuning range (700 – 1000 nm) the pulse width can be adjusted with a Gires-Tournois interferometer (GTI). The GTI introduces a negative group velocity dispersion and therefore compensates for the positive group velocity dispersion that is introduced by the optical elements in the Ti:Sa

cavity (mirrors, Ti:Sa crystal, birefringent filter, acousto optical modulator) and that would lead to a continuous broadening of the output pulses until pulsing breaks down. The pulse width is measured with an external optical autocorrelator (PulseCheck, APE).

Furthermore, a femtosecond option for the Ti:Sa-laser is available (pulse widths of 80 – 100 fs, FWHM), which requires a change of optical elements in the cavity. However, this mode was not used during this work.

Continuous-Wave Mode: Despite the fact that the Ti:Sa is designed as a pulsed laser system, a stable continuous-wave (cw) operation can be achieved in this system by reducing the pump power close to the lasing threshold. In this way the number of oscillating longitudinal modes in the laser resonator is not sufficient to allow for pulsed operation. The Ti:Sa laser system has been operated in cw mode for the acquisition of fluorescence excitation spectra (see chapter 4), where the emission wavelength is tuned in a given wavelength interval by continuously rotating the birefringent filter with the motorised micrometre screw. The wavelength is checked with a wavemeter (WaveMaster, Coherent), which is also used to verify a reproducibility of the laser frequency of better than $1\,\mathrm{cm}^{-1}$.

Frequency Doubling Units

In this work two different frequency doubling units have been used. First, a home-built unit was realised, which allows to frequency double either the cw-output or the full 81 MHz pulsed output of the laser. In this unit the fundamental laser light is focused into a β-barium borate (BBO) crystal (Döhrer Elektrooptik) by an achromatic lens with a focal length of $f = 50\,\mathrm{mm}$. The BBO crystal is cut at an angle of 26.1 ° which allows to achieve the highest doubling efficiency at 450 nm. The crystal was mounted on a rotation stage to satisfy the phase matching condition (type I phase matching) for a given fundamental wavelength, and therefore second harmonic generation of light between 410 nm and 490 nm was possible. The frequency doubled light passed a cylindrical lens ($f = 50\,\mathrm{mm}$) to correct its astigmatism, and colour glass filters (BG39, Schott) blocked residual fundamental laser light. Due to the rather simple realisation of this unit the frequency doubling efficiency is only about 1 % for pulsed fundamental light and about 0.1 % for cw pumping.

Second, for the pulsed picosecond output of the Ti:Sa-laser a frequency doubler/pulse picker (Model 3980, Spectra Physics) was also available. In this doubler/picker at first the repetition rate of the fundamental infrared laser light is reduced from 81 MHz to 8.1 MHz, 4.05 MHz, etc. by a Bragg cell containing an AOM crystal, in which an acoustic wave travels. The acoustic wave generates a refractive index grating that diffracts the laser

beam, and the first diffracted order ("picked light") is frequency doubled by a temperature stabilised lithium triborate (LBO) crystal. The LBO is mounted on a rotation stage and allows second harmonic generation of light in the spectral region between about 430 nm and 520 nm (type I phase matching). In this unit the picking efficiency is about 50 % per pulse and the frequency doubling efficiency is about 5 – 10 %.

3.2.3 Photodetectors

As for the excitation sources a flexible modular concept was realised for the detection path, which is shown schematically in Fig. 3.3.

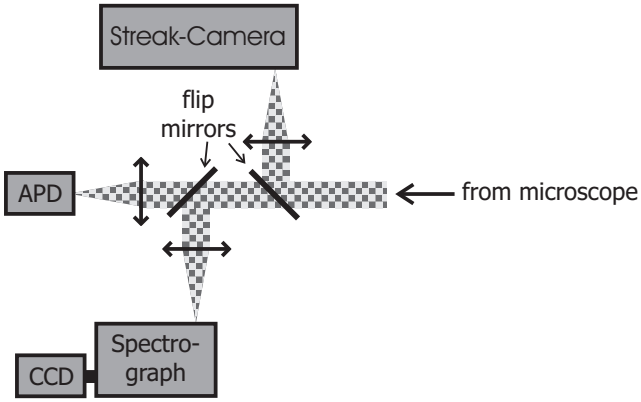

Figure 3.3: Schematic illustration of the detection light path and the photodetectors.

Avalanche Photodiode

For the acquisition of fluorescence excitation spectra (chapter 4) and time-correlated single photon counting measurements (TCSPC, see Ref. [160]) an avalanche photodiode (APD, SPCM-AQR-14, EG&G) with a dark count rate of less than $100\,s^{-1}$ has been utilised. The quantum efficiency of the APD exceeds 70 % at 700 nm and is 40 – 60 % in the spectral region of the MeLPPP emission (450 – 550 nm, see Fig. 3.1b). The active element of the APD is cooled and temperature stabilised by a Peltier element and has a diameter of 180 μm. This chip is a silicon p^+pn-structure biased above the breakdown voltage and therefore every impinging photon generates an electron avalanche, which is then actively quenched. Each detected photon generates a TTL pulse (2.5 V amplitude and 30 ns duration in a 50 Ω load). The single photon arrival time can be measured with an accuracy of about 350 ps. Further digital signal processing of the TTL pulses is performed by a computer-based multifunctional counter board (NI 6024E, National Instruments) and home-made programmes

in the graphical language LabView (National Instruments).

CCD Camera and Spectrographs

Widefield images and fluorescence spectra (see chapters 4 and 6) have been recorded with the combination of an imaging spectrograph (SpectraPro-150, Acton Research Corporation or 250 IS, Bruker) and a sensitive charge coupled device (CCD) camera (SensiCam QE, PCO).

The SpectraPro-150 spectrograph has a focal length of 150 mm and is equipped with a turret containing a 600 lines/mm grating for the acquisition of emission spectra and a mirror for imaging. The 250 IS spectrograph has a focal length of 250 mm and is equipped with three gratings (150, 300, and 1800 lines/mm) mounted on a turret. For this device imaging can be performed in 0^{th} order diffraction by the gratings. The blaze wavelength of all gratings is 500 nm and the diffraction efficiencies are about 70 % in the spectral range of the MeLPPP emission. The signals in both spectroscopy and imaging mode are acquired with the CCD camera which is connected to the spectrographs by a standard C-mount. This ensures that the CCD chip is precisely positioned in the focal plane of the spectrographs. Depending on the gratings and the widths of the entrance slits of the spectrographs spectral resolutions of $3.5\,\mathrm{cm}^{-1}$ (SpectraPro-150) and better than $1\,\mathrm{cm}^{-1}$ (250 IS), respectively, can be achieved.

The CCD chip has a size of 1376 × 1040 pixels each with an area of $6.45 \times 6.45\,\mu\mathrm{m}^2$. In order to reduce the dark counts, the chip is cooled to -12°C by a two-stage Peltier cooler. The dark current at -12°C is 0.1 electrons per second per pixel and the A/D (analogue/digital) conversion factor is 2 electrons per count. The peak quantum efficiency of the CCD camera is 65 % at 520 nm, and 55 – 65 % in the spectral region of the MeLPPP emission. The CCD camera is controlled by a software provided by PCO (Camware) and the images are saved in a binary format. Further data processing was done by home-made LabView and Perl programmes.

Streak Camera System

The streak camera system, that was utilised for the time-resolved measurements (chapter 5), is a combination of a 250 mm imaging spectrograph (250 IS, Bruker) and a streakscope (C5680-24C Synchroscan, Hamamatsu Photonics). The basic idea behind the streak system is to translate both the temporal and the wavelength information into spatial information that can be detected with high precision and allows to acquire both the temporal and the spectral information of a fluorescence decay simultaneously. To this end, the

fluorescence light from the sample is focused onto the entrance slit of the spectrograph where the light is spectrally dispersed by a grating (50 lines/mm, blaze wavelength 600 nm; 150 lines/mm, blaze wavelength 500 nm; 1200 lines/mm, blaze wavelength 500 nm), i. e. the spectral information is converted into a spatial (horizontal) information. The spectrally resolved light is imaged onto the horizontal entrance slit of the streak scope and hits a photocathode where the light is converted into photoelectrons. These are accelerated and pass a pair of horizontally arranged deflection plates where a high-speed sweep voltage is applied with a frequency that is synchronised with the repetition rate of the Ti:Sa-laser system (80.75 MHz). Thus the photoelectrons are the stronger deflected the later they pass the deflection plates, i. e. the later they are generated at the photocathode by the impinging photons. In this way the temporal information is converted into a spatial (vertical) information. Finally, the photoelectrons are multiplied by a factor of about 10^4 in a microchannel plate (MCP) and hit a phosphor screen. The resulting image on this screen is referred to as "streak image" where the horizontal axis corresponds to wavelength and the vertical axis corresponds to time. This image is read out by a CCD camera (C4742-92 Orca-ER, Hamamatsu Photonics) and integrated in computer memory, which allows measurements with a high signal-to-noise ratio. The streak system and the CCD camera is controlled by a commercial software (HPD-TA, Hamamatsu Photonics). The integrated streak images are stored in a binary file format and are further processed by home-made LabView programmes.

The temporal resolution of the streak system depends on several factors, such as the time range (i. e. the length of the time axis of the streak images), the trigger method for the synchroscan unit (optical triggering by a pin-diode or electronic triggering by a TTL-signal output from the AOM-electronics of the Ti:Sa-laser), and the chosen grating in the spectrograph. The best temporal resolution that can be achieved with this streak system is about 2 ps (optical triggering, 50 lines/mm grating). In the configuration used in the experiments described in chapter 5 (electronic trigger, 1200 lines/mm grating) a temporal resolution of about 5 ps was obtained. The overall detection efficiency of the streak system can be estimated to about 3 %. The losses arise mainly from the diffraction efficiencies of the gratings of about 70 %, the quantum efficiency of the photocathode of 15 % (both in the spectral region of the MeLPPP emission), and from the electron optics in the streak tube with about 70 % loss.

The spectral resolution of the streak system depends on the width of the entrance slit of the spectrograph and the grating, and a spectral resolution of about 3 cm^{-1} was achieved.

3.2.4 The Optical Microscope

The optical microscopes used in this work are based on the confocal principle [161], which is schematically shown in Fig. 3.4. In a confocal microscope the excitation light is focused onto an excitation pinhole, directed to an objective with a high numerical aperture, and focused to a diffraction limited spot in the focal plane of the objective. Reflected light or fluorescence is collected by the same objective and imaged onto a second pinhole, the detection pinhole, after which it can be detected. Scattered light (or fluorescence) from a region outside the focal volume of the objective can not pass the detection pinhole (dashed and dotted light path in Fig. 3.4). Therefore the confocal principle ensures that only photons from the focal spot of the objective receive the detector and out-of-focus light is efficiently blocked. This is the reason for the higher signal-to-background ratio that can be achieved with confocal microscopy as compared to conventional microscopic techniques [161, 162].

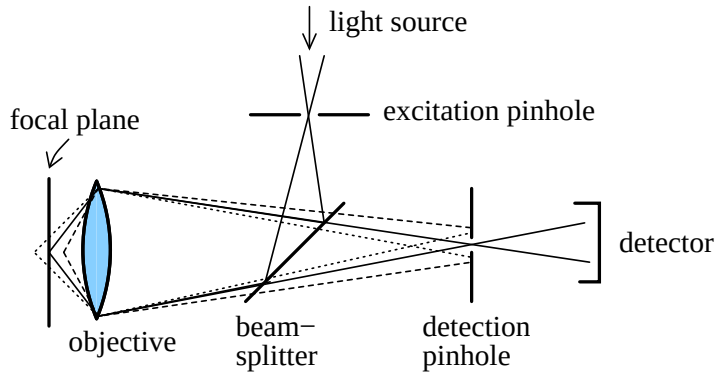

Figure 3.4: Schematic illustration of the confocal principle. The light paths depicted as dotted and dashed lines represent light emitted or scattered from a region outside the focal volume of the objective. This light is effectively blocked by the detection pinhole, and only light emitted or scattered from the focal volume of the objective can be detected.

For the experiments described in this thesis two home-built microscopes were utilised: a combined confocal and widefield microscope including a liquid-helium bath cryostat for measurements at 1.5 K (Fig. 3.5a), and additionally an inverted confocal microscope for room-temperature experiments (Fig. 3.5b). The low-temperature setup was realised during this work and is based on the room-temperature microscope, that was built during a Diploma thesis [163].

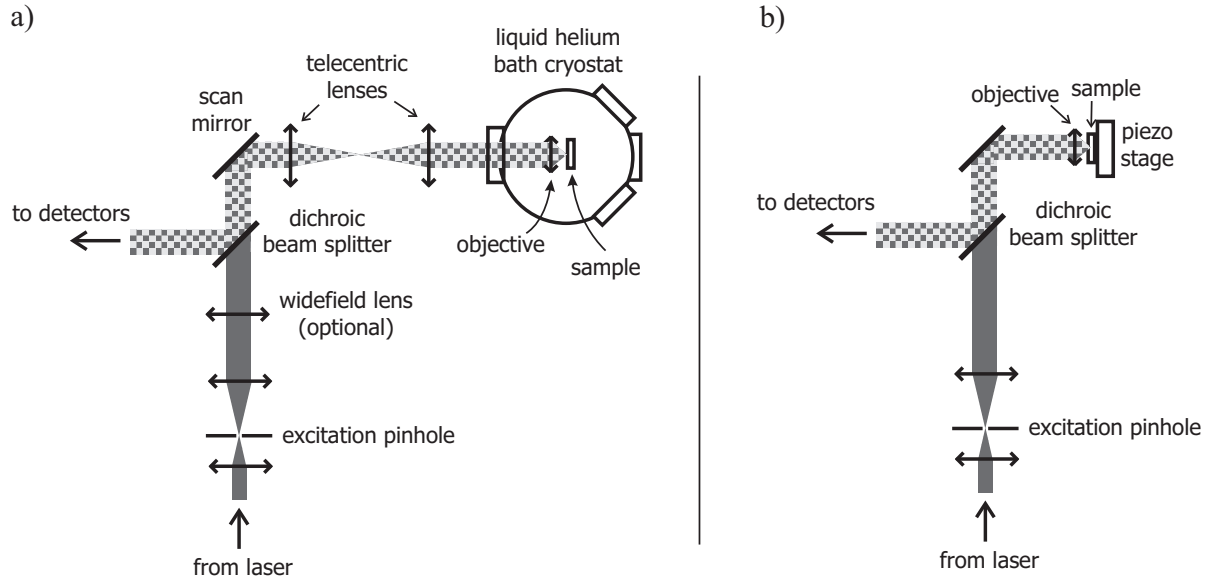

Figure 3.5: Sketch of the confocal microscopes used in this work. a) Low-temperature microscope. b) Room-temperature microscope. For details see text.

Low-Temperature Setup

A schematic illustration of the low-temperature setup is shown in Fig. 3.5a. In confocal mode the excitation light passes a telescope consisting of two achromatic lenses with focal lengths of 40 mm and 160 mm and a pinhole with a diameter of 50 μm to expand the beam diameter with concomitant beam shaping by the pinhole. The light is transmitted through a dichroic beamsplitter (DC670 or z440DCSP, AHF), directed into a home-built cryostat, and focused to a diffraction limited spot on the sample by an objective (NA = 0.85, Microthek). Both the objective and the sample are mounted in an insert that is immersed in suprafluid helium at 1.5 K in a home-built liquid-helium bath cryostat. The fluorescence light is collected with the same objective and reflected by the dichroic beam splitter. After passing suitable filters (BG 39 colour glass, Schott; HQ 500/100 bandpass filter, AHF; HQ467LP long pass filter, AHF), to suppress residual scattered laser light, the fluorescence is focused onto the detectors by achromatic lenses each with $f = 100$ mm. The detection pinholes in this microscope are either the small active area of the APD or the entrance slits of the spectrographs in front of the CCD camera and the streak tube, respectively.

One limitation in confocal microscopy is that only light from a small diffraction limited spot on the sample is detected and therefore only molecules in this volume can be investigated at any given time. To overcome this, either the laser spot has to move across

the sample (beam scanning) or the sample has to move across the focus of the objective (sample scanning). For the low-temperature microscope the former technique has been chosen and the laser spot is moved across the sample by tilting the scan mirror with a pair of computer-controlled, motorised micrometre screws (SM 440, Owis). To avoid vignetting the laser beam passes a pair of telecentric lenses (with $f = 100\,\mathrm{mm}$); in other words, the telecentric arrangement of lenses ensures that the parallel laser beam is always perfectly directed into the back aperture of the objective without being truncated [161]. Furthermore, a widefield option is also available for this microscope. In this mode an additional lens ($f = 200\,\mathrm{mm}$) is positioned in the excitation path in front of the dichroic mirror, which permits to illuminate a large area of about $20 \times 20\,\mu\mathrm{m}^2$ on the sample through the objective. The fluorescence light from this region is again collected by the same objective and imaged through the spectrographs (in imaging mode) onto the CCD camera.

The complete low-temperature setup, which was mainly used for the work described in this thesis, is displayed in Fig. 3.6 with the confocal and widefield option and the various

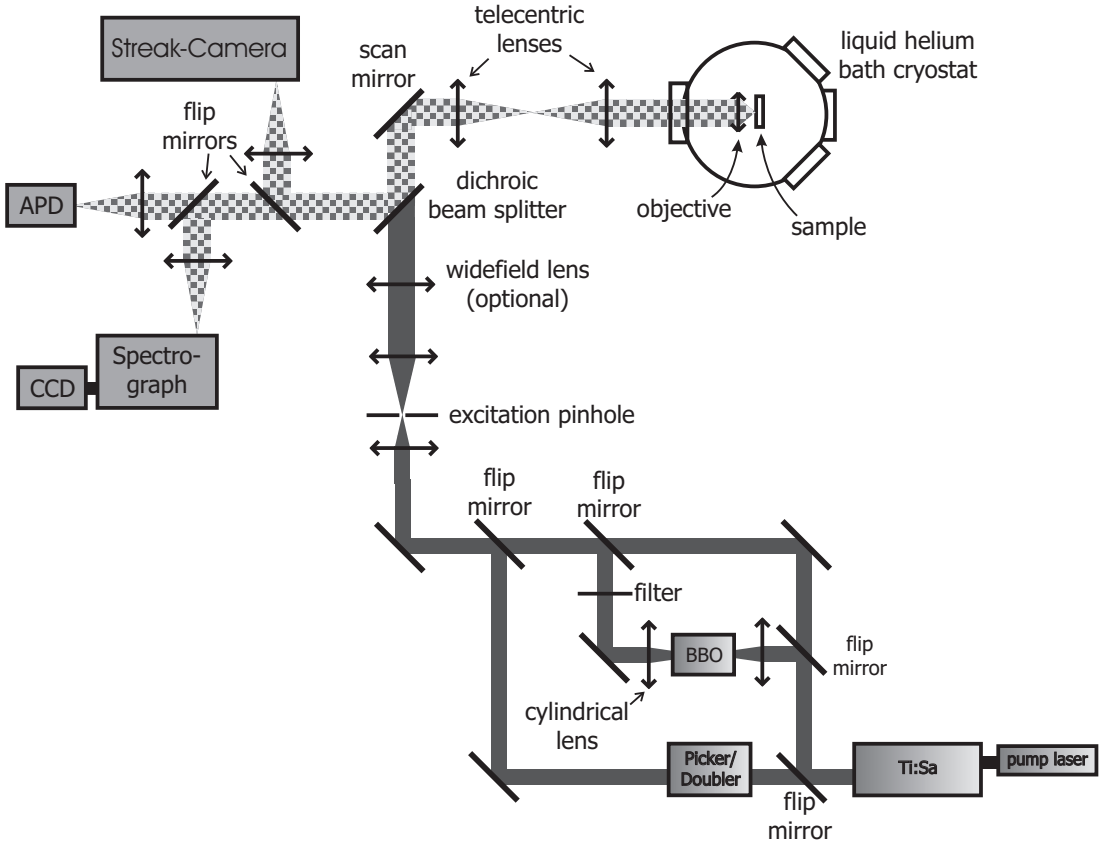

Figure 3.6: Experimental setup for the low-temperature measurements with all excitation light sources and photodetectors.

excitation and detection schemes realised for this microscope.

Room-Temperature Setup

For room-temperature measurements a home-built inverted confocal microscope was also available (Fig. 3.5b). The main difference with respect to the low-temperature microscope, as described above, is the objective and the sample holder. Here, the excitation light was focused by an objective with an NA of 0.95 (PLAPO40X, Olympus) onto the sample that was mounted on a xyz piezo-stage (Tritor 102 SG, piezosystem jena). This stage allows to apply the sample scanning technique, where the sample can be positioned in three dimensions with a maximum displacement of 100 μm and a resolution of about 2 nm for each axis. Therefore a telecentric system was not required for this microscope. A more detailed description of the room-temperature microscope can be found in Ref. [163].

3.2.5 Detection Efficiency and Spatial Resolution

In the following the detection efficiency of the low-temperature setup, i. e. the probability that an emitted photon from the sample is actually detected, will be estimated. The first factor is the collection efficiency of the microscope objective, which is determined by its numerical aperture. The NA is defined as NA $= n \cdot \sin\alpha$, with the refractive index n of the surrounding medium and the angle α corresponding to half of the aperture angle of the cone of light that can be collected by the objective. From NA = 0.85 and under the (simplifying) assumption of a spherical emission characteristic of the sample, the collection efficiency of the objective can be estimated to about 25 %. Further losses of the emitted light arise from the non-perfect transmission of the optical elements in the light path, i. e. the objective, the cryostat windows, and the lenses, where each surface gives rise to 1 – 4 % loss depending on whether the elements are covered with anti-reflection coatings or not. The dichroic beam splitter and the dielectric filters lead to further losses of 5 % each. Hence, the total transmission of the microscope (objective and other optical elements) can be estimated to about 10 %. Finally, the detection efficiency of the detectors have to be considered (see section 3.2.3). This leads to a total detection efficiency of the setup of about 5 % (APD as detector), 4 % (CCD camera combined with spectrographs as detector), and 0.3 % (streak system as detector).

The spatial resolution of the low-temperature setup has been determined by detecting the back-reflected excitation light from the sample substrate with a wavelength of 430 nm through a spectrograph (in imaging mode) with the CCD camera. The lateral width of the focal spot on the substrate was determined to 286 nm (FWHM) by a Gaussian fit.

Theoretically, the width (FWHM) of this spot is given by [161]

$$0.51\frac{\lambda}{\mathrm{NA}} = 258\,\mathrm{nm} \tag{3.1}$$

for a wavelength $\lambda = 430\,\mathrm{nm}$ and an NA $= 0.85$. The agreement between experiment and theory within 10 % is excellent given the fact that the measurement was performed at 1.5 K and without a cover slide between the objective and the sample, whereas the objective is designed for use at room temperature and with a cover slide.

In a similar way the detection efficiency of the room-temperature setup has been estimated to about 3 %, and the spatial resolution is also diffraction limited and close to the theoretical value. A detailed discussion of these issues for the room-temperature setup can be found in Ref. [163].

Chapter 4

Continuous-Wave Two-Photon Spectroscopy

Employing continuous-wave two-photon fluorescence-excitation spectroscopy on MeLPPP-films at room temperature the symmetry properties of the vibronic wave functions of the lowest electronically excited states were studied. It was found that the symmetry selection rules for optical transitions are rather strictly fulfilled in this rigid, rod-like conjugated polymer. Additionally, these data allowed to show that the energies of the predominant vibrational modes, the inter-ring stretching vibration and the aromatic ring CC stretching mode, are significantly lower in the second excited singlet state with respect to the corresponding energies in the first excited singlet state and in the electronic ground state.

4.1 Introduction

Two-photon (2P) materials have attracted considerable attention owing to possible applications for three-dimensional (3D) optical data storage [164], 3D micro-structuring by 2P lithography [165], nonlinear confocal microscopy with intrinsic 3D resolution [166, 167], and optical power limiting [168]. The principle of these applications is based on the 2P absorption process, i.e. the quasi-simultaneous absorption of two photons by atoms or molecules (see section 2.2.2). In order to reduce degradation effects due to irradiation with high intensities that are required to induce this nonlinear process, materials with high 2P absorption cross-sections are crucial. The efficiency of a 2P process is determined by the imaginary part of the 3^{rd} order susceptibility $\chi^{(3)}$, which strongly depends on the electronic properties of the materials [23, 111, 112]. Therefore, organic (macro-)molecules are very promising candidates for efficient 2P materials, because their electronic properties can

be tailored by chemical synthesis. A particularly interesting class of functional materials in this respect are π-conjugated polymers with their extended π-electron system. Because the 3rd order susceptibility $\chi^{(3)}$ increases with the conjugation length [23, 122] conjugated polymers are ideal candidates for 2P-materials.

Despite numerous 2P-studies on various conjugated polymer systems [32–38, 169] to elucidate the energetic location of the lowest lying 2P-allowed electronic singlet levels and the properties of these levels, many questions still remain. For example the issue, to which extend the symmetries of electronic wave functions are determined by the structure of the polymer backbone, has not been discussed as yet. Additionally, the symmetries of the vibrational modes that couple to the electronic states have not been considered in the description of vibronic 2P transitions. Here, these issues are addressed by room-temperature continuous-wave two-photon fluorescence-excitation spectroscopy on thin MeLPPP-films with high spectral resolution.

4.2 Experimental

For the room-temperature 2P experiments thin MeLPPP-films were prepared as described in section 3.1.2. These samples were mounted on the piezo-stage of the home-built inverted confocal microscope and held under a nitrogen atmosphere in order to avoid photodegradation during the measurements. The excitation source was the Titanium:Sapphire (Ti:Sa) laser that was operated in continuous-wave (cw) mode and tuned between 700 nm and 1000 nm (14300 and 10000 cm^{-1}). This tuning range is only limited by the mirror set that was used (see section 3.2.2). The scan speed of the laser was 2.3 nm/s corresponding to about 40 cm^{-1}/s. The laser light was coupled into the confocal microscope and focused to a spot size of 680 nm (FWHM) by an objective with a numerical aperture of 0.95 (PLAPO40X, Olympus) which allowed to achieve excitation intensities up to about 100 MW/cm^2 at the focal spot with cw-excitation. The 2P-excited fluorescence was collected by the same objective, passed a set of colour glass filters (BG39, Schott) that blocked residual scattered laser light, and was then focused onto the avalanche photodiode which also served as detection pinhole. The room temperature absorption spectrum of the MeLPPP-film was measured with an UV/VIS/NIR spectrophotometer (Lambda 9, Perkin-Elmer).

The samples for single-molecule fluorescence spectroscopy on MeLPPP-chains were prepared as described in section 3.1.2. This sample was mounted in the cryostat and cooled to 1.5 K. Single MeLPPP-chains were excited by the frequency-doubled output of the Ti:Sa-

laser (frequency-doubler: Model 3980) at a wavelength of 430 nm with a repetition rate of 81 MHz and a pulse width of 1.5 ps (FWHM) through the low-temperature confocal microscope. The fluorescence light passed through a set of dielectric filters (HQ500/100, AHF) and was spectrally dispersed in a spectrograph (SpectraPro-150). The spectrally resolved light was then imaged onto the CCD camera. More details on the single-molecule measurements and the spatial selection of individual chains can be found in the experimental section of chapter 6.

4.3 Results

Fig. 4.1 shows the (1P) absorption spectrum (dashed line) and the 2P fluorescence-excitation spectrum (solid line) of an MeLPPP-film at room temperature. For better comparison both spectra are displayed on a 1P scale. The excitation energy on a 2P-scale is given on the upper horizontal axis. The excitation intensity for the acquisition of the 2P spectrum was about 2 MW/cm^2. In order to verify that the fluorescence excitation spectrum in Fig. 4.1 (solid line) indeed reflects a 2P-absorption process, the integrated fluorescence intensity I_{Fl} was measured as a function of the 2P-excitation intensity I_{Exc} at an excitation energy of 13240 cm^{-1} (755 nm, corresponding to 26480 cm^{-1} on the 1P-scale) and it was found that $I_{\mathrm{Fl}} \propto I_{\mathrm{Exc}}^{m}$ with $m = 2.02 \pm 0.05$, see Fig. 4.2.

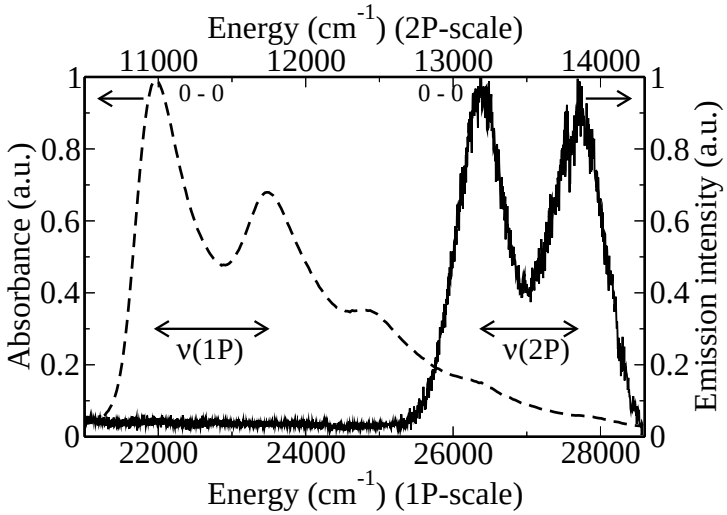

Figure 4.1: Room-temperature absorption spectrum (dashed line) and two-photon fluorescence excitation spectrum (solid line) of an MeLPPP-film. For better comparison both spectra have been normalised. The first vibronic transitions are offset from the corresponding 0-0 transitions by $\nu(1\mathrm{P}) = 1510\,\mathrm{cm}^{-1}$ (1P-spectrum) and $\nu(2\mathrm{P}) = 1290\,\mathrm{cm}^{-1}$ (2P-spectrum), respectively.

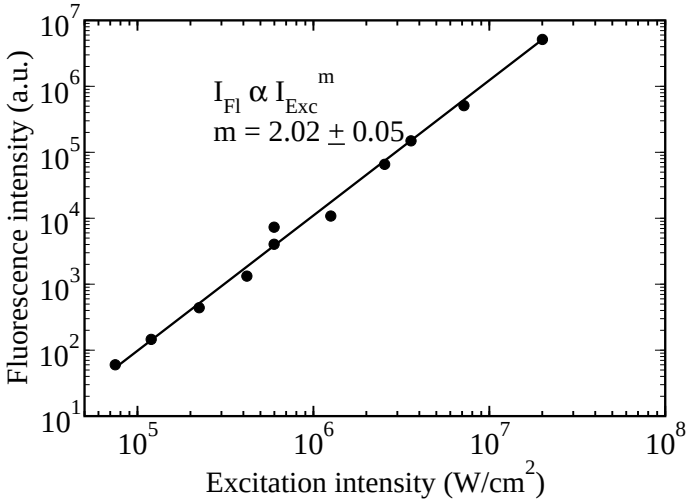

Figure 4.2: Fluorescence intensity, I_{Fl}, for an excitation energy of 13240 cm^{-1} (755 nm, 2P-scale) as a function of the excitation intensity, I_{Exc}, on a log-log scale (dots). The solid line corresponds to a fit $I_{\mathrm{Fl}} \propto I_{\mathrm{Exc}}^{m}$ and yields $m = 2.02 \pm 0.05$.

The (1P) absorption spectrum (Fig. 4.1, dashed line) features a peak at 21970 cm^{-1} (455 nm) with a width of 690 cm^{-1} (FWHM) which is ascribed to the purely electronic (0-0) transition into the lowest excited singlet state [7, 13]. This band is accompanied by a vibronic progression reflecting the coupling of intra-molecular vibrations and their overtones of the MeLPPP-chains to the electronically excited state. The first vibronic (1-0) transition peaks at 23480 cm^{-1} and hence the energy of this vibration is $\nu(1\mathrm{P}) = 1510\,\mathrm{cm}^{-1}$. Overtones of this fundamental mode are observed at 24870 cm^{-1} and 26040 cm^{-1}. The 2P-spectrum features maxima at 26380 cm^{-1} and 27670 cm^{-1} with widths of 830 cm^{-1} and 890 cm^{-1} (FWHM), respectively, which have been assigned to an electronic transition into a higher excited singlet state and a vibronic band [33]. Consequently, this band is offset from the purely electronic transition by $\nu(2\mathrm{P}) = 1290\,\mathrm{cm}^{-1}$. For 2P-excitation energies between 10000 cm^{-1} and 12500 cm^{-1} (20000 cm^{-1} and 25000 cm^{-1} on the 1P-scale) a 2P-induced fluorescence signal with cw-excitation could not be detected (Fig. 4.1, solid line).

Fig. 4.3 displays the low-temperature emission spectrum of an individual chromophore on a single MeLPPP-chain embedded in *n*-hexadecane. This spectrum features the purely electronic (0-0) transition at 21638 cm^{-1} with a width of 75 cm^{-1} (FWHM) and two vibronic lines at 20089 cm^{-1} and 20351 cm^{-1}, which are offset from the (0-0) band by $\nu_1(\mathrm{E}) = 1287\,\mathrm{cm}^{-1}$ and $\nu_2(\mathrm{E}) = 1549\,\mathrm{cm}^{-1}$ (Fig. 4.3, arrows).

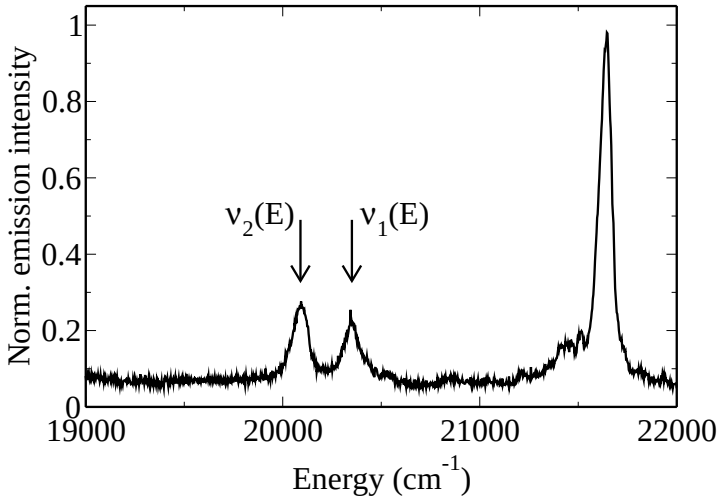

Figure 4.3: Low-temperature fluorescence spectrum of an individual chromophore on a single MeLPPP-chain embedded in *n*-hexadecane. The arrows indicate the spectral positions of the inter-ring and the aromatic ring CC stretching vibration, with energies of $\nu_1(\mathrm{E}) = 1287\,\mathrm{cm}^{-1}$ and $\nu_2(\mathrm{E}) = 1549\,\mathrm{cm}^{-1}$ with respect to the centre energy of the purely electronic (0-0) transition of the emission spectrum.

4.4 Discussion

In section 2.2.2 it has been demonstrated that the *ideal* structure of LPPP belongs to the point group C_{2h}. Inspection of the structure of MeLPPP (Fig. 3.1a) yields that the side groups bound to the backbone do not break this symmetry. The polymer still contains a centre of inversion and the symmetry of the MeLPPP-structure can be described by the C_{2h} point group as well. Following the common classification scheme for conjugated polymers (see section 2.2.2) the wave functions of the electronic states of MeLPPP are also classified according to the irreducible representations (symmetry species) of this point group, which yields states of alternating A_g and B_u symmetry for the manifold of singlet states [23, 25, 26, 34].

Since neither absorption spectroscopy nor 2P fluorescence excitation spectroscopy revealed an additional singlet state in the spectral region between $21970\,\mathrm{cm}^{-1}$ and $26380\,\mathrm{cm}^{-1}$, the data presented in Fig. 4.1 provide significant evidence that for MeLPPP the transition from the electronic ground state into the lowest excited singlet state is 1P-allowed but 2P-forbidden and *vice versa* for the transition into the second excited singlet state. This mutual exclusion of the 1P and 2P transitions is consistent with the parity selection rules for optical transitions between states of A_g and B_u symmetry, described in section 2.2.2, and corroborates the common classification for the singlet states of MeLPPP. This find-

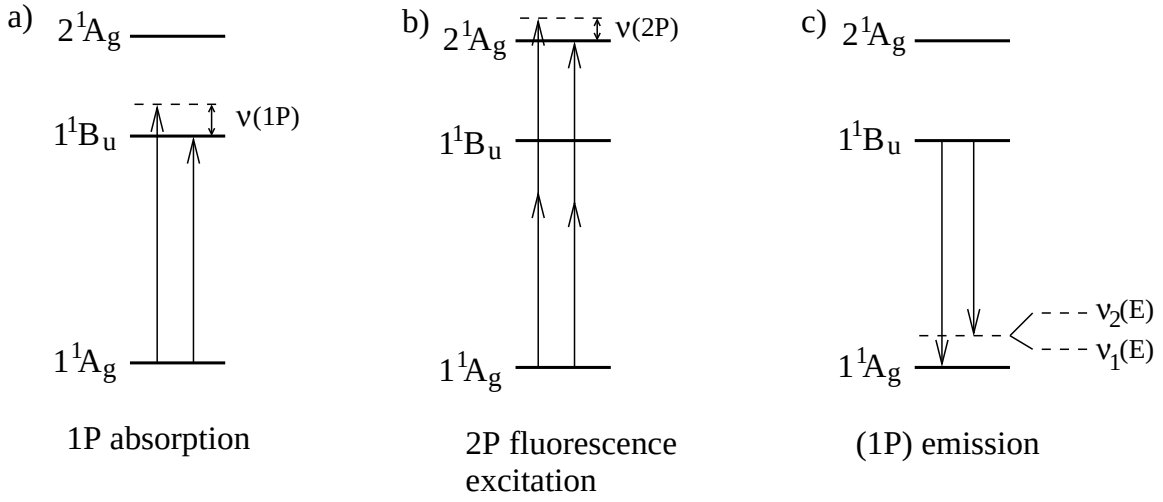

Figure 4.4: Simplified energy level scheme of MeLPPP with the vibronic one- and two-photon transitions observed in the optical spectra presented in Figs. 4.1 and 4.3. a) 1P absorption process, b) 2P absorption process, c) (1P) emission process.

ing is rather surprising. Given the bulky and flexible side groups bound to the MeLPPP backbone and the disordered sample morphology, one would expect that a bending of the side chains gives rise to stress or strain and thus to a slight distortion of the backbone. Consequently, the symmetry would be lowered and the symmetry selection rules would not be strictly fulfilled. However, the data in Fig. 4.1 indicate that this is not the case. The inversion symmetry of the MeLPPP backbone, and thus the inversion symmetry of the electronic wave functions, that are localised on the backbone, is well maintained. This is also reflected by the rather low excitation intensities of only $2\,\mathrm{MW/cm^2}$, that were necessary to induce the 2P absorption process in MeLPPP.

The optical spectra depicted in Figs. 4.1 and 4.3 allow the following assignment of electronic transitions, which is illustrated in Fig. 4.4 in simplified Jablonski diagrams with the lowest electronic singlet states of MeLPPP together with the optically allowed 1P and 2P transitions. The 1P (0-0) resonance at $21970\,\mathrm{cm^{-1}}$ is ascribed to the electronic $1^1B_u \leftarrow 1^1A_g$ transition, and accordingly the single-molecule emission spectrum comes from the $1^1B_u \rightarrow 1^1A_g$ transition (see also sections 2.2.1 and 2.2.2). Additionally, the data presented in Fig. 4.1 indicate that the 2P resonance at $26830\,\mathrm{cm^{-1}}$ corresponds to the transition into the *second* excited singlet level of MeLPPP, which is located $4410\,\mathrm{cm^{-1}}$ above the lowest excited 1^1B_u singlet state. Accordingly, this 2P-allowed level is labelled 2^1A_g in accordance with theoretical studies on poly(*para*-phenylenes) [170]. Hence, the 2P (0-0) resonance can be assigned to the electronic $2^1A_g \leftarrow 1^1A_g$ transition.

For the appearance of the higher-energy peak at 27670 cm^{-1} in the 2P spectrum of MeLPPP (Fig. 4.1) there are in principle two possible interpretations. First, this band may correspond to an additional even parity (A_g) electronic state located $\nu(2P) = 1290\,cm^{-1}$ above the 2^1A_g level, i. e. 5700 cm^{-1} above the lowest excited 1^1B_u singlet state. For a PPV-derivative (dioctyloxy-PPV, DOO-PPV) two energetically closely spaced A_g levels were identified about 4800 cm^{-1} above the lowest excited 1^1B_u state by 2P absorption experiments and quantum chemical calculations [169, 171]. However, the relative intensities of these two A_g states in the 2P spectra of DOO-PPV are significantly different and the 2P absorption cross-sections for the transitions from the A_g ground state into these "adjacent" 2P-allowed levels were shown to differ strongly [169, 171, 172]. In contrast, the two bands in the 2P spectrum of MeLPPP (Fig. 4.1) exhibit basically identical intensities (i. e. they have similar 2P absorption cross-sections). Additionally, for polyfluorene, a ladder-type pentamer, and particularly MeLPPP neither experimental results (from pump-probe and electroabsorption spectroscopy) nor quantum chemical calculations indicate signatures of a manifold of even parity singlet states, only a single A_g level is found [34, 170, 173, 174] in the energy region accessible with the 2P experiments described in this work. Therefore, the interpretation, that two (or more) A_g singlet states lying between 4000 cm^{-1} and 6000 cm^{-1} above the lowest excited singlet (1^1B_u) state are present, seems to be unlikely for MeLPPP.

Second, the band at 27670 cm^{-1} observed in the 2P spectrum of MeLPPP (Fig. 4.1) may be a vibrational level coupled to the electronic 2^1A_g state at 26830 cm^{-1} [33]. Then the vibrational energy determined from this 2P spectrum is $\nu(2P) = 1290\,cm^{-1}$ (Fig. 4.1), whereas the vibrational energy in the 1^1B_u state is $\nu(1P) = 1510\,cm^{-1}$, as retrieved from the 1P absorption spectrum (Fig. 4.1). These numbers are consistent with values found by others. Recent 1P and 2P absorption experiments on MeLPPP dissolved in toluene yielded vibrational frequencies of 1544 cm^{-1} and 1310 cm^{-1}, respectively [33]. Raman spectroscopy on MeLPPP-films revealed a strong double peak at 1568 cm^{-1}/1604 cm^{-1}, that was ascribed to an aromatic ring CC stretching vibration featuring a line splitting due to the side groups, and a strong line at 1319 cm^{-1}, that was attributed to an inter-ring stretching mode [152]. In Table 4.1 the frequencies of the vibrational modes coupled to the various electronic states together with the Raman data taken from the literature have been summarised.

A straightforward interpretation of these findings would be a mutual exclusion of the two vibrational modes in the 1P- and 2P-spectra [33] based on symmetry selection rules. However, as will be shown below this interpretation is not appropriate. In Born-Oppenheimer approximation the wave functions for the electronic ground (excited) state is denoted by $|e_i\rangle$ ($|e_f\rangle$) and for the vibrational state coupled to the electronic ground (excited) state

	excited singlet states		singlet ground state	
	ν(2P) (cm^{-1})	ν(1P) (cm^{-1})	ν_1(E) (cm^{-1})	ν_2(E) (cm^{-1})
SM emission			1287	1549
Raman			1319	1568/1604
1P absorption		1510		
2P absorption	1290			

Table 4.1: Energies of the vibrational modes in the lowest excited singlet states and the electronic ground state observed in the single-molecule (SM) emission spectrum (Fig. 4.3), Raman spectra, the one-photon (1P) absorption spectrum (Fig. 4.1), and the two-photon (2P) fluorescence excitation spectrum (Fig. 4.1). All data have been taken from room-temperature spectra, only the SM emission spectrum was recorded at 1.5 K. The Raman data have been taken from Ref. [152].

by $|\mu\rangle$ ($|\nu\rangle$). Then the total wave function for the vibronic state is written as a direct product of the corresponding electronic and vibrational wave functions, see section 2.1.2. With this the symmetry selection rules for a molecule of C_{2h} symmetry, derived in section 2.2.2 for purely electronic transitions, can be easily extended to vibronic transitions. For a 1P-allowed vibronic transition the selection rule reads [129]

$$\Gamma(|e_i\rangle) \times \Gamma(|\mu\rangle) \times \Gamma(\hat{p}_l) \times \Gamma(|e_f\rangle) \times \Gamma(|\nu\rangle) = A_g, \tag{4.1}$$

for at least one component of the transition-dipole moment operator $\hat{p}_l$ (l = x,y,z). $\Gamma(\ldots)$ denotes the symmetry species of the entity within parenthesis. A similar selection rule holds for a 2P-allowed transition involving the two-photon tensor S_{lm} (l, m = x,y,z) [129, 131]:

$$\Gamma(|e_i\rangle) \times \Gamma(|\mu\rangle) \times \Gamma(S_{lm}) \times \Gamma(|e_f\rangle) \times \Gamma(|\nu\rangle) = A_g. \tag{4.2}$$

In the point group C_{2h} the symmetry species of the components of the transition dipole moment operator and the 2P tensor, respectively, is given by [129, 131]

$$\Gamma(\hat{p}_l) = \begin{pmatrix} B_u \\ B_u \\ 0 \end{pmatrix} \quad \text{and} \quad \Gamma(S_{lm}) = \begin{pmatrix} A_g & A_g & 0 \\ A_g & A_g & 0 \\ 0 & 0 & 0 \end{pmatrix}, \tag{4.3}$$

see also eqs. (2.15) and (2.18). For the conditions in the experiments in this work the initial level for the 1P- and 2P-transitions is the vibrational ground state of the electronic ground state, which is a totally symmetric level, and thus $\Gamma(|e_i\rangle) \times \Gamma(|\mu\rangle) = A_g$. For the

1P transition the symmetry species of the excited electronic level is $\Gamma(|e_f\rangle) = B_u$, whereas for the 2P transition $\Gamma(|e_f\rangle) = A_g$, as shown above. Together with eq. (4.3) relations (4.1) and (4.2) reduce to

$$\begin{aligned} A_g \times B_u \times B_u \times \Gamma(|\nu\rangle) &= A_g \qquad \text{for 1P,} \\ A_g \times A_g \times A_g \times \Gamma(|\nu\rangle) &= A_g \qquad \text{for 2P,} \end{aligned} \tag{4.4}$$

revealing that a vibration that is observable in either the 1P- or 2P-spectrum has to belong to the totally symmetric a_g symmetry species (for multiplication rules for the symmetry species see Appendix A). Consequently, vibrational modes that contribute to the vibronic bands observed experimentally cannot be discriminated by symmetry selection rules via 1P- and 2P-spectroscopy.

According to the Raman data the inter-ring and aromatic ring CC stretching modes differ in energy by only $270\,\mathrm{cm}^{-1}$ [152], whereas the inhomogeneous line broadening is about $700 - 800\,\mathrm{cm}^{-1}$, as observed for the 0-0 bands of the 1P- and 2P-spectra, respectively. This prevents to observe the two vibronic transitions separately in the room-temperature spectra, which is demonstrated in Fig. 4.5, where the (1P) absorption spectrum (dashed line) together with the Raman spectrum (solid black line) of an MeLPPP-film is depicted. The Rayleigh line of the Raman spectrum has been shifted to an energy of $21970\,\mathrm{cm}^{-1}$, which corresponds to the centre energy of the 0-0 transition of the absorption spectrum. Note that this is only meant for illustration because the Raman lines arise from vibrational modes coupled to the electronic ground state, whereas the first vibronic band of the absorption spectrum results from vibrations coupled to the lowest electronically excited singlet state. However, this simplified approach shows that the strong Raman lines of the inter-ring and aromatic ring CC stretching modes are well within the envelope of the first vibronic (1-0) transition of the absorption spectrum and indicates that both vibrations may indeed contribute to the 1-0 band of the 1P spectrum. Therefore, the 1-0 transition of the absorption spectrum was modelled by a superposition of two Gaussian functions (Fig. 4.5, dotted lines), representing the two vibrational modes. The centre energies of these Gaussians are given by the spectral positions of the inter-ring and aromatic ring CC stretching modes in the *shifted* Raman spectrum, and their widths were chosen to $690\,\mathrm{cm}^{-1}$, corresponding to the inhomogeneous line width of the absorption spectrum. The sum of these two Gaussian functions is depicted by the solid grey line in Fig. 4.5, which does not show a sub-structure and reproduces the 1-0 transition of the 1P spectrum quite well given the strong simplifications of this modelling. From these data it is evident, that the two aforementioned vibrational modes can not be resolved in the room temperature ensemble spectra.

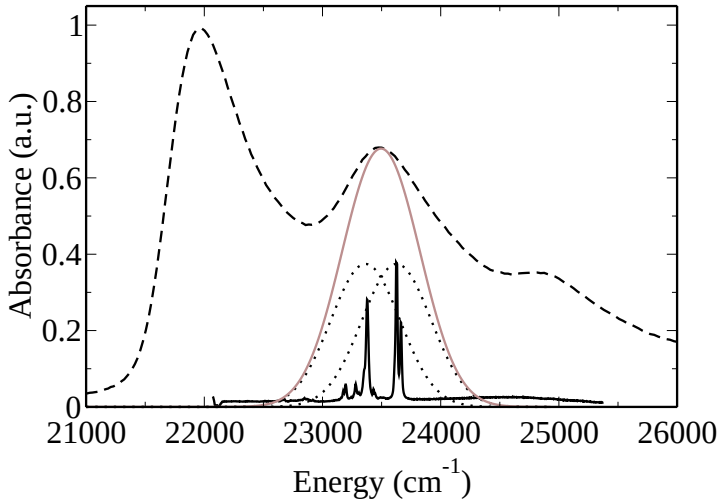

Figure 4.5: Room-temperature absorption spectrum (dashed line) and Raman spectrum (solid black line) of an MeLPPP-film. The Rayleigh line of the Raman spectrum has been shifted such that it coincides with the centre energy of the 0-0 transition (21970 cm^{-1}) of the absorption spectrum. The dotted and solid grey curves are simulated spectral lines. The dotted curves have been calculated by convoluting both strong lines of the *shifted* Raman spectrum with a Gaussian function with a width of 690 cm^{-1} (FWHM) that corresponds to the inhomogeneous line width of the absorption spectrum. The solid grey line is the sum of both Gaussians. Note that this is a highly simplified approach because the absorption spectrum yields the vibrational energies in the lowest electronically excited singlet state, whereas the energies determined from Raman spectra correspond to energies of vibrations in the electronic ground state.

An independent piece of information concerning this issue is provided by the low-temperature emission spectrum of an individual chromophore on a single MeLPPP-chain presented in Fig. 4.3. Employing single-molecule spectroscopy significantly reduces the inhomogeneous line width of the (0-0) emission and indeed allows to resolve two vibronic lines, which are offset from the (0-0) band by $\nu_1(\mathrm{E}) = 1287\,\mathrm{cm}^{-1}$ and $\nu_2(\mathrm{E}) = 1549\,\mathrm{cm}^{-1}$ (Fig. 4.3, arrows). This observation provides strong evidence for the interpretation that the vibronic bands in the 1P and 2P spectra correspond to a superposition of contributions from the interring stretching and the aromatic ring CC stretching mode.

Based on these findings and considering the different frequencies of the vibrational modes coupled to the various electronic levels (Table 4.1), it has to be concluded that the vibrational energies in the 2^1A_g level are significantly lower with respect to those in the 1^1B_u and 1^1A_g levels. This conclusion is consistent with the finding that for conjugated polymers small geometric and/or electronic perturbations may result in large changes of their vibrational or Raman spectra [98, 175–177].

The strong reduction of the vibrational energies in the 2^1A_g level might therefore reflect a larger delocalisation of the excitation energy in this electronically excited state with respect to the 1^1B_u and 1^1A_g levels, since Raman spectroscopy on a series of all-*trans* polyenes and oligo(*para*-phenylenevinylenes) revealed a significant decrease of the energy of the C=C stretching mode with increasing chain length [98, 176]. However, this interpretation seems to be unlikely for MeLPPP, because Raman experiments on ladder-type oligomers and polymers yielded only a small shift of several wavenumbers for the vibrational energies for increasing chain length [177].

Alternatively, the change of the energy of vibrational modes as a function of the electronic configuration might reflect significant changes of the equilibrium geometry of the polymer backbone in the 2^1A_g level with respect to the equilibrium geometry in the lower singlet states. Evidence for this interpretation comes from the observation that the relative intensity of the first vibronic (1-0) transition with respect to the purely electronic (0-0) transition is larger in the 2P spectrum as compared to the 1P spectrum (Fig. 4.1). This can be quantified in terms of an *apparent* Huang-Rhys parameter S_{app}, because in the 2P spectrum only the 0-0 and the 1-0 bands are observed due to the limited tuning range of the Ti:Sa-laser:

$$S_{\mathrm{app}} = -\ln\left(\frac{I_{0-0}}{I_{0-0}+I_{1-0}}\right). \tag{4.5}$$

Here, I_{0-0} (I_{1-0}) stands for the integrated intensity of the 0-0 (1-0) transition (see section 2.2.3). From the 2P spectrum an apparent Huang-Rhys parameter of 0.7 is derived for the 2^1A_g level, while from the 1P spectrum $S_{\mathrm{app}} = 0.6$ is determined for the 1^1B_u state. The higher apparent Huang-Rhys parameter for the 2^1A_g state implies a larger equilibrium value of the configuration coordinate in the potential energy surface along the normal coordinates of the inter-ring and aromatic ring CC stretching vibrations in the 2^1A_g level with respect to the 1^1B_u state (Fig. 4.6). This indicates a change in the equilibrium geometry with larger average interatomic distances [21] in the backbone for the 2^1A_g state. Therefore, it is reasonable to assume that the binding strength between the atoms is weaker and as a result the vibrational frequencies are lower in the second excited singlet state as compared to the lower singlet levels, as schematically sketched in Fig. 4.6. A qualitatively similar observation has been made for the C=C stretching mode in oligothiophenes, i. e. a change in the vibrational energy of this mode was found between 1P and 2P spectra, and was interpreted accordingly [37].

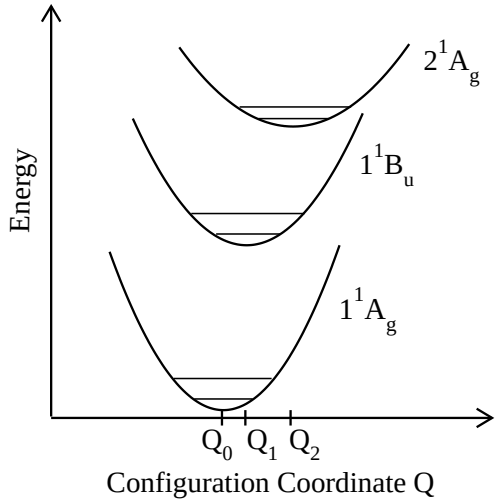

Figure 4.6: Schematic illustration of the potential energy surfaces in harmonic approximation along the configuration coordinate of the inter-ring (or aromatic ring CC) stretching vibrations for the three lowest electronic singlet states. Q_i $(i = 0, 1, 2)$ marks the equilibrium values of the potential energy surfaces in the electronic ground state (1^1A_g) and the first (1^1B_u) and second excited singlet levels (2^1A_g), respectively. The larger equilibrium value Q_2 and larger radius of curvature of the potential energy surface of the 2^1A_g state is the result of a substantial change in the equilibrium geometry of the MeLPPP backbone in this electronic level with respect to the lower singlet states. This leads to smaller vibrational energies in the 2^1A_g level as compared to those in the 1^1B_u and 1^1A_g levels as indicated by the horizontal lines which represent the vibrational levels.

4.5 Conclusions

In this chapter it has been shown that for MeLPPP the parity selection rules for optical transitions are well obeyed, which reflects the high degree of symmetry, particularly the presence of a centre of inversion, in the electronic wave functions in the lowest singlet states. This result is rather surprising because at first sight one would expect that the bulky and flexible side groups bound to the backbone would break the symmetry of the polymer. These findings for MeLPPP are in contrast with results from 2P-spectroscopy on polymers such as PPVs [36, 38]. The (2P-allowed) $2^1A_g \leftarrow 1^1A_g$ transition in PPV has a much lower 2P cross-section [38, 119] as compared to the $2^1A_g \leftarrow 1^1A_g$ transition of MeLPPP [33], which reflects the fact that PPVs are less rigid than MeLPPP. The strict validity of the symmetry selection rules for MeLPPP follows also from experiments where pulsed excitation intensities of about $100\,\mathrm{GW/cm^2}$ per pulse were required to induce the $1^1B_u \leftarrow 1^1A_g$ transition by a "forbidden" 2P process [32, 35]. Additionally, the energies

of the vibrational modes coupled to the electronic levels were found to differ by about $220\,\mathrm{cm}^{-1}$ between the first and second electronically excited singlet states of MeLPPP. This observation is ascribed to significant changes of the equilibrium geometry of the MeLPPP backbone in the 2^1A_g level with respect to the 1^1B_u and the 1^1A_g states. These data show that MeLPPP provides an excellent model system for conjugated polymers in general, and non-linear spectroscopy in particular.

Chapter 5

Picosecond Excitation Energy Relaxation Processes

The relaxation processes of electronic excitations in the lowest electronically excited singlet state in MeLPPP were studied employing picosecond time-resolved spectroscopy with high spectral resolution. An inverse Laplace transform of the fluorescence decay curves provides strong evidence that the relaxation dynamics can be described by a distribution of excited state lifetimes. At 1.5 K both the decay dynamics and particularly the rising component of the fluorescence transients from the low-energy tail of the distribution of excited states show a strong dependence on the emission wavelength. In contrast, at room temperature such a dependency is not observed. Finally, the data allow to retrieve the radiative lifetime of the lowest excited singlet state, which was determined to about 800 ps both at 1.5 K and 296 K.

5.1 Introduction

For the design and development of devices based on conjugated polymers it is of crucial interest to gain detailed understanding of the excitation energy transfer mechanisms and relaxation pathways both within the inhomogeneously broadened distribution of electronically excited states (DOS) and to the electronic ground state. On the one hand, intra-DOS migration of electronic excitations is an important prerequisite for efficient light harvesting employed in organic solar cells, on the other hand, migration to trap sites and subsequent fluorescence quenching is an undesired loss mechanism that limits the efficiency of light-emitting devices [45, 178].

Time-resolved fluorescence spectroscopy is a powerful tool to elucidate the relaxation

dynamics of electronic excitations both within the DOS and to the electronic ground state [39–48, 144, 155, 156, 178–181]. Experimental work and computer simulations allowed to model the intra-DOS relaxation dynamics of electronic excitations in terms of an energy dispersive incoherent hopping transfer mediated by a distance dependent electronic coupling between different sites within the DOS [40–43, 143, 144, 179]. The results indicated a time- and energy-dependent relaxation of electronic excitations towards lower energy sites which is manifested by a transient red-shift of the fluorescence spectrum and a strong dependence of the fluorescence decay kinetics on the emission wavelength.

However, as yet the experimental observation of the time- and energy-dependent relaxation processes was hampered by several factors. First, after photoexcitation fast trapping processes of electronic excitations at defect sites with concomitant fluorescence quenching may occur [41, 144]. Because trapping takes place on time scales that are of the same order of magnitude than intra-DOS relaxation [41, 108, 155, 156], a direct observation of intra-DOS processes was very difficult, if not impossible, to achieve. While fluorescence quenching at trapping sites is negligible for ladder-type polymers because the concentration of chemical defects is very low [7], the presence of molecular oxygen opens another relaxation channel for electronic excitations in these polymers. In this case both MeLPPP and its hydrogen-substituted analogue (LPPP) tend to form emissive keto-defects by oxidation of the chain [153,154], which show up as a broad, structureless, and red-shifted band superimposed onto the fluorescence spectrum [108, 153, 155, 156]. Therefore, the relaxation dynamics, that was observed in (Me)LPPP as yet, was dominated by fast excitation energy transfer to keto-defect sites and intra-DOS processes could not be resolved [108, 155, 156]. Second, in the time-resolved experiments the spectral resolution was rather low with about $150\,\mathrm{cm}^{-1}$ [39–45, 144, 178–181]. This resulted in a spectral averaging of the fluorescence decay curves over a large energy region within the DOS and consequently prevented a precise determination of the energy-dependent relaxation rates.

The interpretation of time-resolved data to describe the relaxation dynamics of electronic excitations in conjugated polymers is further complicated by the observation of non-exponential fluorescence decay kinetics [39–42, 45, 108, 144, 155, 156, 178, 181]. This finding indicates that the decay dynamics of electronic excitations is more appropriately described by a distribution of lifetimes rather than by a single time constant [41,42,108,144]. However, a clear picture of the decay rate distributions does not exist.

In this chapter the results of time-resolved spectroscopy on MeLPPP with enhanced spectral resolution are presented. Special care was taken to avoid the formation of emissive keto-defects in the investigated MeLPPP-films during the sample preparation and the experiments. These data allowed to uncover the energy dependence of the decay times

in great detail and, in particular, the energy dependence of the rising components of the fluorescence decay curves, which has not been observed as yet. Additionally, an inverse Laplace-transform (ILT) was applied to analyse the fluorescence transients, which allowed to directly calculate the lifetime distributions.

5.2 Experimental

The MeLPPP-films were prepared as described in section 3.1.2. These samples were mounted in the cryostat and either cooled to 1.5 K or held in helium atmosphere at room temperature to avoid sample degradation during the experiment. The films were excited at 430 nm into the first vibronic transition of MeLPPP (Fig. 3.1) to ensure a sufficiently large spectral separation between excitation and emission wavelengths. The Ti:Sa laser was operated at 860 nm with a repetition rate of 81 MHz and a pulse width of 1.5 ps (FWHM). The Ti:Sa output was frequency doubled in the home-built unit comprising a focusing lens, a BBO crystal mounted on a rotation stage, a cylindrical lens to correct the astigmatism of the frequency doubled light, and colour glass filters (BG39, Schott) that blocked residual fundamental laser light. The frequency doubled light was coupled into the home-built low-temperature confocal microscope, directed into the cryostat, and focused to a spot size of 430 nm (FWHM) by an objective (NA=0.85, Microthek) that was immersed in liquid (1.5 K) or gaseous (296 K) helium. The excitation intensity was kept at a moderate level of 88 W/cm^2. The fluorescence light was collected by the same objective and focused onto the entrance slit of a streak camera system, where the fluorescence was spectrally dispersed in a spectrograph with a 1200 lines/mm grating that allowed to monitor a spectral window of 680 cm^{-1} (corresponding to 15 nm at 470 nm) with a spectral resolution of 3 cm^{-1}. The spectrally resolved light was imaged onto the entrance slit of the streak scope. The resulting streak images were read out by a computer-controlled CCD camera and integrated with the photon counting method. The instrument response function (IRF) of the setup was determined by detection of the frequency doubled excitation pulses at 430 nm that were reflected from the sample substrate. The IRF had a width of 10 ps (FWHM), allowing for a temporal resolution of 5 ps when deconvolution techniques were applied during data analysis.

5.3 Results

Fig. 5.1 shows the high-resolution streak camera data of the 0-0 emission of MeLPPP recorded at 296 K. The right part of Fig. 5.1a depicts the room-temperature streak image, where the horizontal axis corresponds to time, the vertical axis corresponds to wavelength, and the fluorescence intensity is given by the grey scale. The left part of Fig. 5.1a shows the time-integrated spectrum which is obtained by numerical integration of the streak camera data. The time-integrated spectrum is identical to the respective part of the steady-state

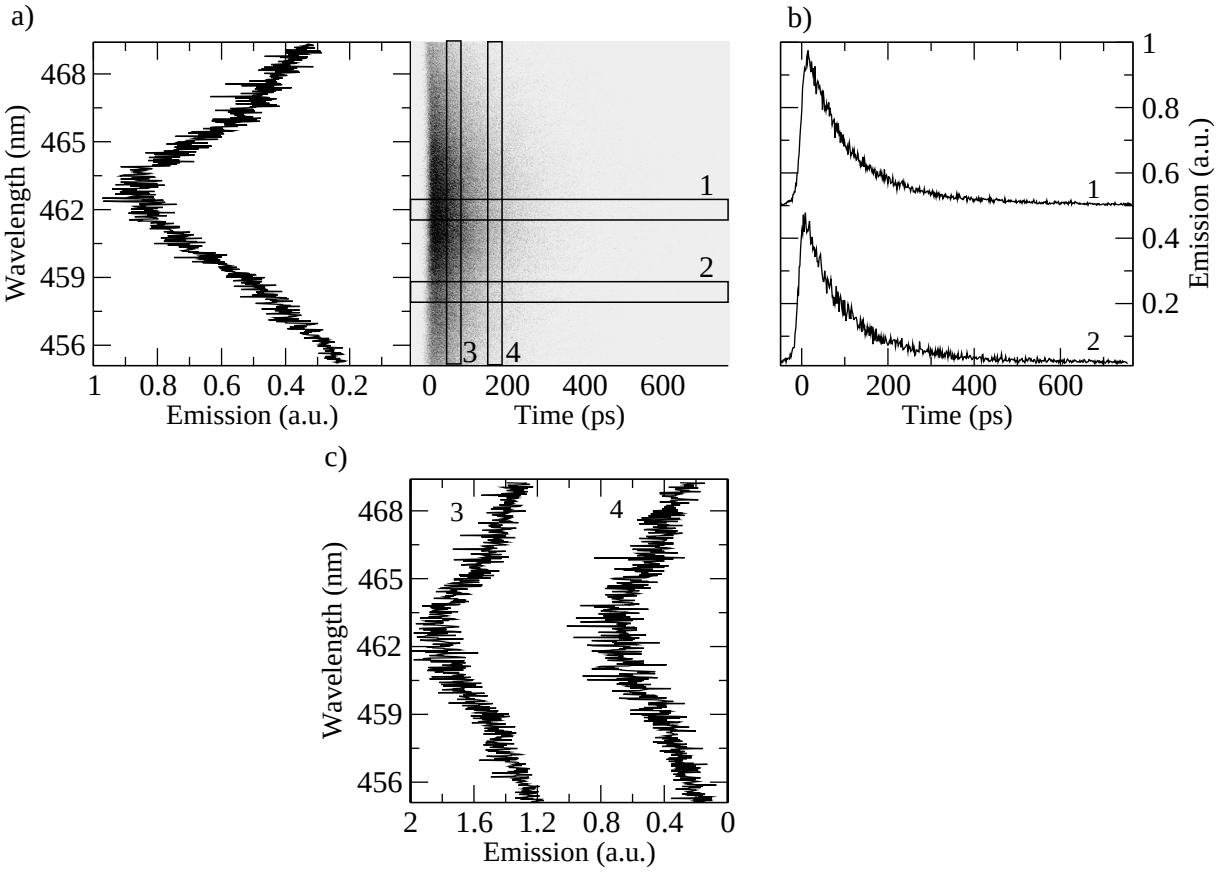

Figure 5.1: Room-temperature streak data: a) streak data with the fluorescence intensity given by the grey value (right) and the corresponding time-integrated emission spectrum (left). b) Two normalised fluorescence decay curves that were extracted from the streak image by spectral integration of the 20 cm^{-1} wide boxed regions at 21646 cm^{-1} (461.98 nm, curve 1) and 21861 cm^{-1} (457.44 nm, curve 2). c) Two normalised transient spectra extracted from the streak image by temporal integration of the 5 ps wide boxed regions at 63 ps (spectrum 3) and 160 ps (spectrum 4).

fluorescence spectrum depicted in Fig. 3.1b (top). In Fig. 5.1b two examples of normalised fluorescence decay curves are presented that were extracted from the streak image by integration of two spectral windows of 20 cm^{-1} width in the centre and the high-energy tail of the spectrum (Fig. 5.1a, boxes 1 and 2). In the following the centre energy of a particular spectral integration window (here: 21646 cm^{-1} and 21861 cm^{-1}) will be referred to as detection energy.

At room temperature the lifetimes show a strong dependence on the sample and vary between about 100 ps and 200 ps. This is in accordance with results reported in the literature, where lifetimes as short as several tens of picoseconds were observed in MeLPPP-

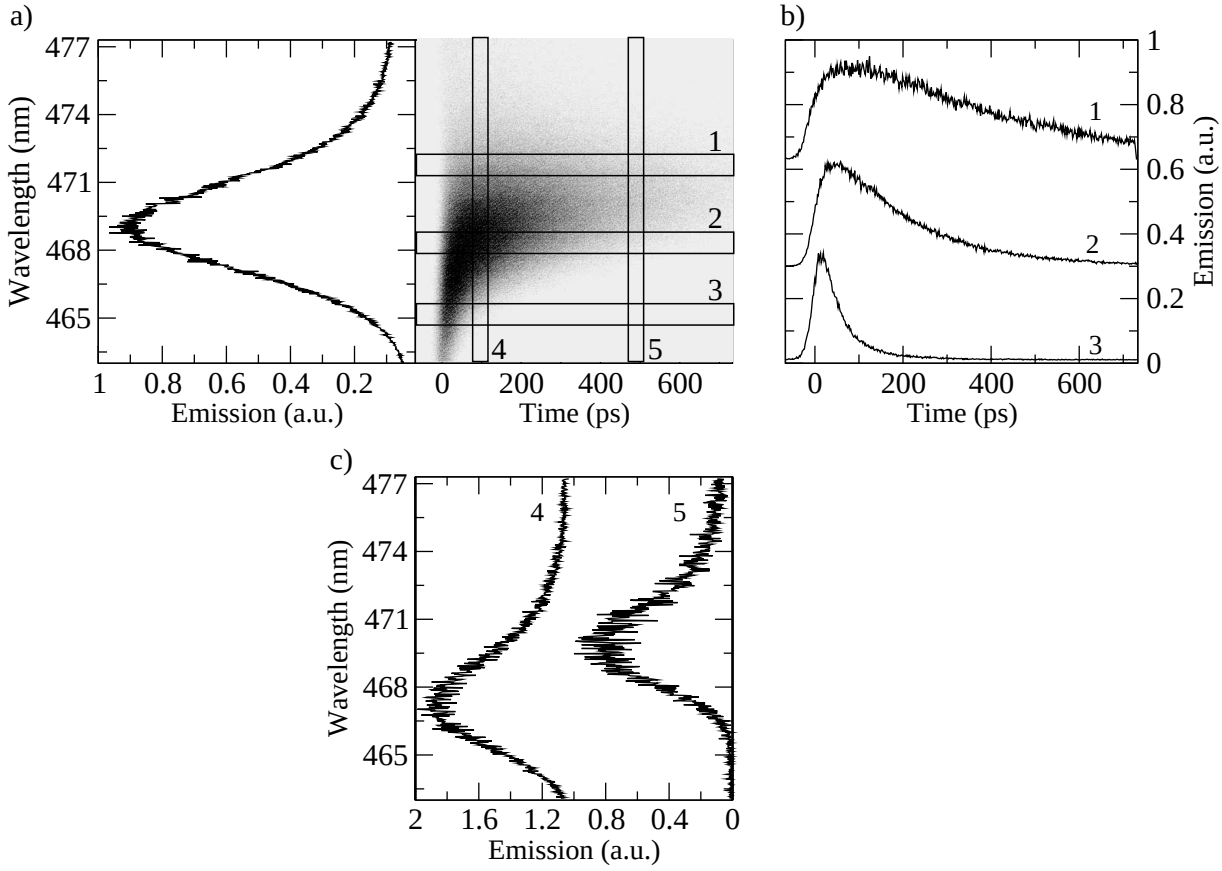

Figure 5.2: Low-temperature streak data: a) streak image (right) and the corresponding time-integrated spectrum (left). b) Three normalised fluorescence decay curves extracted by spectral integration of 20 cm^{-1} wide boxed regions at 21177 cm^{-1} (472.21 nm, curve 1), 21342 cm^{-1} (468.56 nm, curve 2), and 21488 cm^{-1} (465.38 nm, curve 3). c) Two normalised transient spectra extracted from the streak image by temporal integration of the 5 ps wide boxed regions at 96 ps (spectrum 4) and 480 ps (spectrum 5).

films [155, 182]. But as a rule, for MeLPPP at room temperature the decay times do not depend on the detection energy and the rise time of the fluorescence transients is determined by the onset of the IRF of the setup. As a typical example two fluorescence decay curves featuring a lifetime of about 100 ps are presented in Fig. 5.1b. Fig. 5.1c depicts two transient fluorescence spectra that were extracted from the streak image by integration of 5 ps wide time windows (Fig. 5.1a, boxes 3 and 4) at $t = 63$ ps (spectrum 3) and at $t = 160$ ps (spectrum 4). The transient spectra at room temperature are identical to the time-integrated spectrum (Fig. 5.1a, left) and do not depend on time.

The 1.5 K streak image and the respective time-integrated spectrum of the 0-0 transition are depicted in Fig. 5.2a. The latter is identical to the respective part of the steady-state emission spectrum acquired at 1.5 K (Fig. 3.1b, bottom). In Fig. 5.2b three examples of normalised decay curves are shown that were extracted by spectral integration of 20 cm^{-1} wide spectral windows in the centre and the high- and low-energy wings of the spectrum, respectively. A pronounced dependence of these fluorescence transients on the detection energy is apparent, and, in particular, the decay time strongly increases from tens of picoseconds to several hundreds of picoseconds for decreasing detection energy. In the high-energy tail of the spectrum the rising part of the decay curves is given by the onset of the IRF (Fig. 5.2b, curve 3), whereas a rise time of several tens of picoseconds was measured at low detection energies (Fig. 5.2b, curves 1 and 2). Additionally, the transient spectra from the 1.5 K streak data (Fig. 5.2c, spectra 4 and 5) uncover a spectral red-shift of about 200 cm^{-1} and a decrease in line width of about 50 cm^{-1} within several tens to hundreds of picoseconds after the exciting laser pulse.

5.3.1 Analysis of the Fluorescence Decay Curves

In order to study the dependence of the fluorescence transients on the detection energy in more detail, decay curves from the high-resolution streak images (Fig. 5.1a and Fig. 5.2a) were extracted as a function of the detection energy in steps of 20 cm^{-1} for the 1.5 K data and 110 cm^{-1} for the 296 K data. The spectral width of the integration window was always 20 cm^{-1}. The fit function $f(t)$ for these fluorescence transients was a sum of at most two exponential functions with reconvolution of the IRF $I(t)$:

$$f(t) = \int_{-\infty}^{t} \left[I(t') \cdot \sum_{i=1}^{2} A_i \exp\left(-\frac{t-t'}{\tau_i} \right) \right] dt', \tag{5.1}$$

where A_i and τ_i are the amplitudes and time constants, respectively, of the exponential function. The quality of the fits was evaluated by examination of the reduced χ^2-value,

the random distribution of the weighted residuals, and the autocorrelation of the weighted residuals.

Additionally, the fluorescence decay curves were analysed by means of an inverse Laplace transform algorithm which directly yielded the distribution of decay rates contained in the data. For this analysis the CONTIN programme by S. Provencher [183, 184] was utilised, which performed the Laplace inversion of the decay curves. Since an ILT is a so called *ill-posed* problem, i. e. for noisy data a very large number of solutions exists that all fit the experimental data, the CONTIN programme also imposes constraints on the ILT in order to compute a stable solution (for details see Appendix B and Ref. [183]). From the obtained decay rate distributions the expectation values were calculated and taken as a measure for the excited state lifetimes. The widths of these distributions were not evaluated, because this parameter is very sensitive to details of the fluorescence decay curves, in particular to the signal-to-noise and signal-to-background ratio.

Exponential Fitting

First, the results of the exponential fitting procedure will be presented. As an example, Fig. 5.3a shows the fluorescence decay curve (solid black line), that was extracted from the room-temperature streak image at a detection energy of 21646 cm^{-1}, together with the result of a bi-exponential fit to this curve (solid grey line). It is evident from the fit that the onset of the decay curve is determined by the onset of the IRF (Fig. 5.3a, dashed line). The bi-exponential function satisfactorily describes the data and a fast and slow component with time constants of 10 ps and 100 ps could be resolved. The amplitudes of the slow (A_{slow}) are larger than those of the fast (A_{fast}) decay component, $A_{slow} > A_{fast}$, i. e. the slow component is the dominating one. The (bi-)exponential fits to the remaining room-temperature decay curves gave similar amplitude ratios (i. e. $A_{slow} > A_{fast}$) and similar time constants of about 10 ps and 100 ps, both of which did not depend on the detection energy (Fig. 5.4a, open squares). However, at low detection energies a mono-exponential function with a lifetime of 100 ps and a positive amplitude is already compatible with the data. A bi-exponential fit did not improve the quality of the fit according to the criteria mentioned above (reduced χ^2-value, random distribution of the weighted residuals, autocorrelation of the weighted residuals). This is attributed to the low signal-to-noise ratio of the fluorescence transients extracted from this tail region of the emission spectrum.

The lifetimes of the low-temperature data determined by (bi-)exponential fits are presented in Fig. 5.4b, where the open squares depict decay times and the open diamonds show rise times. At the highest detection energies (21530 – 21600 cm^{-1}) a single exponential with

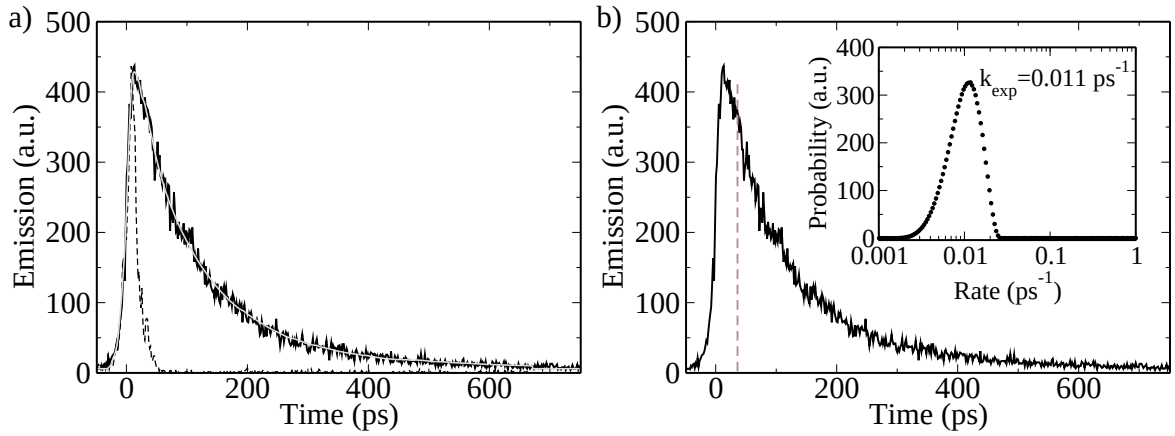

Figure 5.3: a) Fluorescence decay curve extracted from the room-temperature streak data in Fig. 5.1a at a detection energy of 21646 cm^{-1} (solid black line). The instrument response function is depicted by the dashed curve. The solid grey line represents a bi-exponential fit with convolution of the IRF to the data, which yielded time constants of 10 ps and 100 ps. b) The solid black line shows same decay curve as in part a). The inset displays the decay rate distribution calculated by an inverse Laplace transform of only the decaying part of the fluorescence transient (to the right of the dashed vertical line). The expectation value of the decay rate distribution was determined to $k_{exp} = 0.011\,ps^{-1}$ (corresponding to 91 ps).

a time constant of about 30 ps is compatible with the experimental data (open squares). Between 21440 cm^{-1} and 21530 cm^{-1} the data are fitted by a bi-exponential function with a fast component that increases from 30 ps to 40 ps for decreasing energy, and a slow component of about 100 ps that does not dependent on the detection energy (open squares). In this spectral region (21440 – 21600 cm^{-1}) the amplitudes of all exponentials are positive, i. e. the rising part of the fluorescence transients is determined by the onset of the IRF, and the amplitudes of the fast components are significantly larger than those of the slow (100 ps) components ($A_{fast} > A_{slow}$). Below a detection energy of 21440 cm^{-1} reasonable agreement with the data is obtained by a bi-exponential fit, where one component has a positive amplitude and the second component has a negative amplitude. For decreasing detection energy in this spectral region the lifetime that corresponds to the positive amplitude component increases from about 100 ps to 450 – 500 ps (open squares), whereas the rise time that corresponds to the negative amplitude component increases from 10 ps to 60 ps (open diamonds).

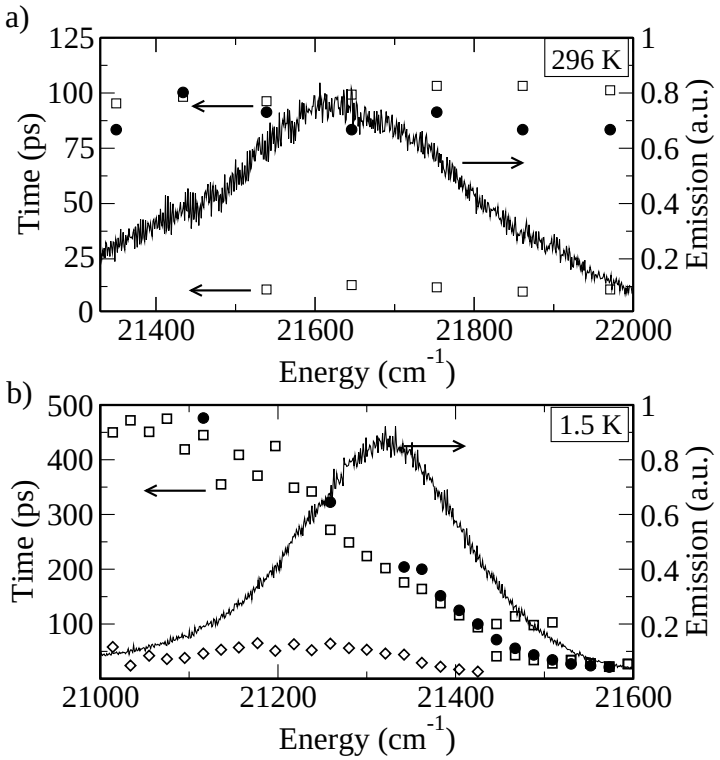

Figure 5.4: Excited state lifetimes of the 0-0 transition of an MeLPPP-film. a) room temperature fluorescence lifetimes as a function of the emission energy determined by (bi-) exponential fits to the decay curves (open squares). The filled circles correspond to the expectation values of the decay rate distributions that were computed by an inverse Laplace-transform of the fluorescence transients. b) Low temperature time constants as a function of the emission energy determined by (bi-)exponential fits to the decay curves (open symbols): the open squares show the decay components and the open diamonds the rise times. The expectation values of the decay rate distributions of the fluorescence transients as determined by an inverse Laplace-transform are depicted as filled circles. For illustration the respective time-integrated fluorescence spectra are overlaid in a) and b) as solid line.

Inverse Laplace Transform

Next, the results of the inverse Laplace transform of the fluorescence decay curves by means of the CONTIN programme will be detailed. Fig. 5.3b shows again the fluorescence transient extracted from the room-temperature streak data at a detection energy of $21646\,\mathrm{cm}^{-1}$. The inset of Fig. 5.3b depicts the decay rate distribution that was computed from the experimental data by an ILT at 200 grid points on a logarithmic scale between $0.001\,\mathrm{ps}^{-1}$ and $1\,\mathrm{ps}^{-1}$. Since deconvolution of the IRF is not implemented in the CONTIN programme, only data points with $t \geq 37\,\mathrm{ps}$ (marked by the dashed grey line in Fig. 5.3b)

were used for this analysis to avoid artefacts caused by the IRF. The resulting distribution has only a single peak with decay rates distributed around an expectation value of $0.011\,\mathrm{ps}^{-1}$. This value corresponds to a lifetime of 91 ps, which is in good accordance with the predominant slow component (100 ps) as determined by the bi-exponential fit. For the remaining fluorescence transients from the room-temperature streak image (Fig. 5.1a) similar results were obtained. All decays are consistently described by single-peaked rate distributions with expectation values between 80 ps and 100 ps (Fig. 5.4a, filled circles).

Since the ILT analysis is limited to the decaying part of the fluorescence transients, the rising components of the fluorescence decay curves that appear in the 1.5 K data below a detection energy of $21440\,\mathrm{cm}^{-1}$ could not be analysed with the CONTIN programme. The ILT analysis of the decaying components yielded single-peaked distributions of decay rates with continuously increasing expectation values from about 20 ps to about 500 ps for decreasing detection energies (Fig. 5.4b, filled circles). The expectation values are in accordance with the decay times (of the dominating decay components for detection energies between $21440\,\mathrm{cm}^{-1}$and $21530\,\mathrm{cm}^{-1}$) determined by the exponential fits. For detection energies below $21440\,\mathrm{cm}^{-1}$ only few distributions with the corresponding expectation values were computed, because the turnover from the rising to the decaying parts of the transients was difficult to determine due to the increasing decay and rise times.

5.3.2 Spectral Moments

Further information about the time- and energy-dependence of the relaxation processes of electronic excitations can be obtained from the temporal evolution of the centre energy and the line width of the spectra. For this analysis transient spectra were extracted from the streak images (Fig. 5.1a and Fig. 5.2a) by integrating 5 ps wide time windows of the streak data. At room temperature the transient spectra are identical to the time-integrated spectrum (Fig. 5.1a and c) and can be fitted by a Gaussian with reasonable agreement. The 1.5 K transient spectra, however, exhibit an asymmetric line shape, see Fig. 5.2c. Such complex line shapes can be analysed utilising spectral moments. For a discrete data set $\{I(\nu_i)\}$, with $I(\nu_i)$ being the intensity at the spectral position ν_i, the moments are defined as

$$M_1 = \frac{1}{N}\sum_i \nu_i I(\nu_i) \tag{5.2}$$

$$M_2 = \frac{1}{N}\sum_i (\nu_i - M_1)^2 I(\nu_i), \tag{5.3}$$

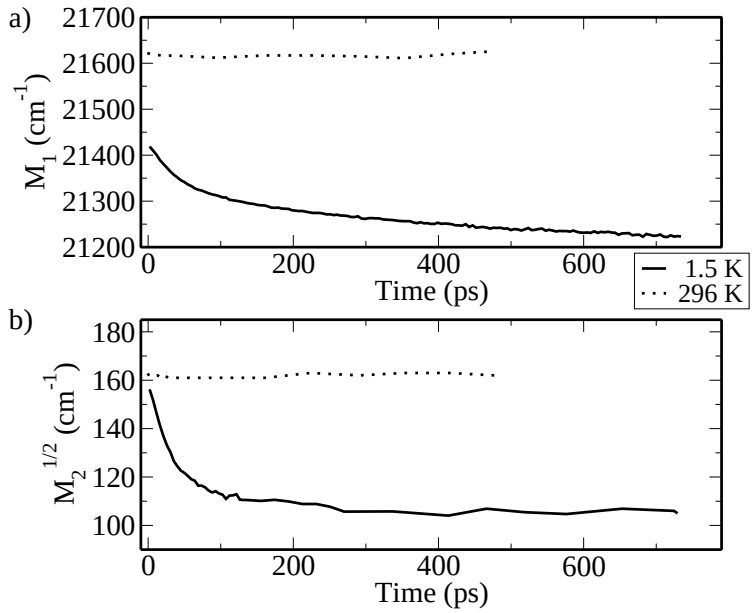

Figure 5.5: a) First spectral moment M_1 as a function of time. b) Square root of the second spectral moment $\sqrt{M_2}$ as a function of time. The dotted lines in a) and b) represent the moments calculated from the room-temperature streak image and the solid lines show the moments determined from the low-temperature streak data.

where $N = \sum_i I(\nu_i)$ is the integrated intensity of the spectrum. The first spectral moment M_1 corresponds to the expectation value of the data set and is a measure for the centre energy (the spectral centre of mass) of the transient spectra. The square root of the second moment $\sqrt{M_2}$ represents the standard deviation from the expectation value and can be considered as a generalised line width. In order to facilitate the comparison between the 1.5 K and 296 K results the spectral moments of the transient spectra were calculated for both data sets.

In Fig. 5.5 the first moment (a) together with the square root of the second moment (b) for both the 1.5 K (solid lines) and the 296 K data (dotted lines) is presented as a function of time. At room temperature (Fig. 5.5a,b, dotted lines) the moments do not depend on time and the mean values are $M_1 = 21620\,\mathrm{cm}^{-1}$ and $\sqrt{M_2} = 162\,\mathrm{cm}^{-1}$, respectively. The first moment is in excellent agreement with the centre energy of $21614\,\mathrm{cm}^{-1}$ of the time-integrated spectrum as determined by a Gaussian fit and demonstrates that this approach is applicable to the analysis of the transient spectra. For $t \geq 480$ ps the moments were not calculated because the fluorescence signal already decayed to the background level (see Fig. 5.1a,b).

From the low-temperature analysis (Fig. 5.5a,b, solid lines) a pronounced time de-

pendence for both spectral moments was found. M_1 shifts from 21419 cm^{-1} at $t = 0$ ps to 21224 cm^{-1} at $t = 750$ ps and reflects a transient red-shift of the spectra of about 200 cm^{-1}. The red-shift as a function of time can be satisfactorily described by a bi-exponential function with time-constants of 40 ps and 430 ps. $\sqrt{M_2}$ continuously decreases from 156 cm^{-1} at $t = 0$ ps to 105 cm^{-1} at $t = 750$ ps. This "decay" of the line width is compatible with a single exponential yielding a time constant of 40 ps.

5.4 Discussion

5.4.1 Distribution of Excited State Lifetimes

The observation of non-exponential fluorescence decays of MeLPPP both at room temperature and in the high-energy wing of the spectrum at cryogenic temperatures (Fig. 5.4) is in agreement with literature data on conjugated polymers [39–42, 45, 48, 108, 144, 155, 156, 178, 181, 185]. Two mechanisms have been identified that give rise to non-exponential fluorescence kinetics in conjugated polymer samples. The first is bimolecular annihilation of electronic excitations [21, 48, 182, 185], i. e. singlet-singlet, singlet-triplet, and triplet-triplet annihilation, that dominate the decay dynamics at high excitation intensities. Second, the deviation of the fluorescence decays from an exponential function may reflect the presence of a distribution of excited state lifetimes in conjugated polymers [41, 42, 46, 108, 144, 186].

For the time-resolved data presented in this work bimolecular annihilation can be ruled out because for MeLPPP these processes become important only for pulse energies per area of higher than 90 $\mu\mathrm{J/cm}^2$ [48, 182]. However, the streak data in this work were recorded with pulse energies per area of about 1 $\mu\mathrm{J/cm}^2$, which can be calculated from the excitation wavelength of 430 nm, the excitation intensity of 88 $\mathrm{W/cm}^2$, and the repetition rate of the exciting laser of 81 MHz. Therefore, it can be concluded that for MeLPPP a distribution of excited state lifetimes leads to the observed non-exponential fluorescence decays.

In order to calculate the distribution of decay rates from non-exponential fluorescence decay curves several approaches exist. One widely used method is to fit the fluorescence transients by a Kohlrausch-Williams-Watts (KWW) type stretched exponential function [41, 42, 108, 144, 186]

$$f(t) = \exp\Big[-\Big(\frac{t}{\tau}\Big)^{\beta}\Big], \tag{5.4}$$

where τ is a characteristic lifetime and $0 < \beta \leq 1$. For an exponent $\beta = 1$ eq. (5.4) reduces to a mono-exponential function with a single time constant τ, and $\beta < 1$ indicates a lifetime distribution, whose width increases for $\beta \to 0$ [142, 187]. However, for the

investigated conjugated polymer systems the parameter β was found to be a function of both the detection energy and time [41,42,108,144]. Whereas the energy dependence of β in principle would be consistent with the current understanding of excitation energy relaxation processes in conjugated polymers, the time dependence of the exponent demonstrates that the KWW function is not appropriate to model the data. This was attributed to the fact that a KWW type stretched exponential describes incoherent relaxation processes in (temporally, spatially, and energetically) random and infinite systems [142]. In contrast, a conjugated polymer sample clearly represents a finite, non-random system [28, 144].

Kersting *et al.* used another method and utilised a discrete pseudo Laplace transform [42]. In principle this approach directly yields the decay rate distributions contained in the data. However, the analysis of the non-exponential fluorescence transients of PPV revealed a trimodal decay rate distribution [42], which is difficult to interpret in terms of the present understanding of the photophysics of conjugated polymers. The trimodal structure of the distribution might be an artefact caused by the discretisation method used by Kersting *et al.*, because the number of grid points, i. e. the number of exponentials in the kernel of the Laplace transform, was only 60 [42]. In contrast, in this work stable solutions of the ILT were only found for more than 100 exponentials, and typically 200 exponentials were used (see Fig. 5.3 and Appendix B). The inverse Laplace transform of the (non-)exponential fluorescence transients of MeLPPP that was performed here demonstrates that a single-peaked distribution of decay rates indeed consistently describes the (non-) exponential fluorescence kinetics observed for MeLPPP. This strongly supports the interpretation that the deviation from an exponential decay comes from the presence of a distribution of excited state lifetimes [41, 42, 108, 144]. The expectation values of the lifetime distributions provide a measure for the excited state lifetimes.

The origin of the lifetime distributions can be ascribed to the fact that conjugated polymer samples are highly disordered systems [28,30,49]. Therefore the distances between the chromophores as well as the mutual orientations with respect to each other are broadly distributed ("spatial disorder" [41]). Since the transfer rates of electronic excitations within the DOS are a function of both the inter-site distances and their mutual orientations (see section 2.3), the distributions of these quantities directly translate into a distribution of transfer rates and consequently lead to a distribution of excited state lifetimes.

Moreover, by time-resolved spectroscopy on a series of oligomers [oligo(fluorenes), oligo(phenylene vinylenes), ladder-type oligo(phenylenes)] it was shown that the transition dipole moment (lifetime) is the larger (shorter) the longer the oligomer [116–118]. Because an oligomer can be considered as a model system for a chromophore on a polymer chain [30, 85], it is reasonable to assume that chromophores on a polymer with different conjugation

lengths have different oscillator strengths as well [93, 150, 151]. Additionally, the width (and spectral position) of the DOS of a conjugated polymer is determined by statistical variations of the conjugation length as well as fluctuations in the local environment of the chromophores [29, 30, 84, 85]. Hence, in a given detection energy window (e. g. box 1 in Fig. 5.1a) chromophores with different conjugation lengths (oscillator strengths) contribute to the emission signal which leads to a distribution of lifetimes in this interval. Further support for this notion comes from a very recent single-molecule/ensemble study on a short-chain PPV derivative, which contains only 2 – 3 chromophores per chain [93]. By single-molecule spectroscopy it was shown that only one chromophore per chain emits at any given time. Additionally, the fluorescence decay of each individual chromophore followed an exponential function and the lifetime of the emitting site varied with its conjugation length. In contrast, the fluorescence decay of an ensemble of this short-chain polymer (i. e. in the presence of a distribution of conjugation lengths) exhibited a bi-exponential decay [93]. This resembles the situation found for J-aggregates, where a non-exponential fluorescence decay was shown to result from a disorder induced broad distribution of oscillator strengths in each exciton state [188].

5.4.2 Relaxation Dynamics of Electronic Excitations

In the following the expectation values of the decay rate distributions (or alternatively the time constants of the predominant decay components as determined by bi-exponential fits) will be referred to as excited state lifetimes for clarity.

Low Temperature

In the high-energy regime of the DOS (detection energies above 21440 cm^{-1}, Fig. 5.4b) the low-temperature dynamics of electronic excitations is dominated by fast nearest-neighbour transfer processes to energetically lower lying sites within the DOS (see also Fig. 2.10 in section 2.3). Hence, the measured lifetimes of 30 – 40 ps (Fig. 5.4b, open squares and filled circles) provide a lower boundary for the nearest-neighbour transfer times at 1.5 K. This approach is in agreement with earlier studies on PPV and LPPP [42, 108, 144]. Since the onset of the fluorescence transients is determined by the IRF it is concluded that the rising component, resulting from a delayed population from energetically higher lying sites, is beyond the temporal resolution of the streak setup. Additionally, the states located at high energies within the DOS have a low statistical weight and are barely populated. Therefore, the rising components have only small amplitudes and the transients are dominated by the much larger amplitudes of the decay components.

The time constants of the rising components that appear in the intermediate energy regime (21160 cm^{-1} – 21440 cm^{-1}, Fig. 5.4b, open diamonds) are in good accordance with the time constants of the fast decay components in the high-energy regime (above 21440 cm^{-1}), both of which are of the order of several tens of picoseconds. Additionally, the fast initial transient red-shift of the spectrum as well as the narrowing of the line width of the transient spectra occur on the same time scale of several tens of picoseconds (Fig. 5.5, solid lines). These findings provide strong evidence that the rising components result from delayed population of low-energy states from energetically higher lying sites through intra-DOS transfer processes of electronic excitations prior to decay to the electronic ground state.

For the lowest detection energies (below 21160 cm^{-1}) slightly increasing decay times are still observed that can be attributed to very slow intra-DOS relaxation processes occurring on time scales of 450 – 500 ps (Fig. 5.4b, open squares and filled circles), which compete directly with the decay to the electronic ground state. This interpretation is corroborated by the observation of the slow transient red-shift within 430 ps (Fig. 5.5a, solid line).

The continuously increasing decay and rise times towards lower detection energies reveal the energy- and time-dependence of the intra-DOS relaxation processes. This is particularly pronounced in the region between 21440 and 21160 cm^{-1}, where the decay times increase from 100 ps to about 400 ps (Fig. 5.4b, open squares and filled circles). The relaxation behaviour in this region of the DOS can be understood in terms of a growing number of non-nearest neighbour transfer processes due to a continuously decreasing number of available sites at still lower energy in the low-energy tail of the DOS. Since the relaxation of electronic excitations within the DOS is mediated by a distance dependent electronic coupling [40–42, 82, 144, 146, 179], non-nearest neighbour jumps are characterised by a prolonged waiting time before such transfer processes take place and give rise to a continuous increase in the transfer times (and hence in the measured lifetimes). Moreover, it has been shown that the intra-chain transfer rates are at least one order of magnitude smaller than the inter-chain transfer rates [82, 180, 189]. Therefore, the growth of the time constants for decreasing energy may reflect at least in part the crossover from inter-chain transfer predominating at short times (tens of ps) to intra-chain transfer processes occurring on significantly longer time scales (hundreds of ps).

Room Temperature

At room temperature neither energy-dependent relaxation rates (Fig. 5.4a) nor a transient red-shift of the emission spectra (Fig. 5.5a, dotted line) were observed for the investigated

MeLPPP-films. This is in contrast to findings on polyfluorenes and PPV and its derivatives, where a rise time of 1 – 2 ps in the low-energy tail of the DOS [39,181] as well as a red-shift of the transient emission spectra on a time scale of tens of picoseconds [39, 40, 181] was detected. Missing rise times of the order of 1 ps could still be attributed to the limited temporal resolution of the streak setup in this work. However, the absence of a transient red-shift of the emission leads to the conclusion that at room temperature differences in the thermally assisted population of energetically higher lying sites within the DOS in combination with differences in the photophysical parameters between MeLPPP and the other polymers are responsible for the room-temperature observations on MeLPPP in this work.

For MeLPPP the lifetime of the excited state is relatively short (≤ 200 ps), whereas for PPV and derivatives the lifetime exceeds 1 ns [39, 45, 178]. Additionally, if the inhomogeneous line width of the absorption spectrum is taken as a measure for the width of the DOS, then for MeLPPP the width of the DOS is 690 cm^{-1} (FWHM, Fig. 3.1b, top). For PPV and derivatives the width of the DOS amounts to 750 – 1220 cm^{-1} [41, 144]. An upper limit for the homogeneous line width of MeLPPP is given by the line width of about 260 cm^{-1} (FWHM) of an individual chromophore, which was measured by single-molecule fluorescence spectroscopy [54], i. e. a significant contribution to the ensemble line width of MeLPPP comes from homogeneous broadening. The homogeneous line width of MEH-PPV was determined to be about 210 cm^{-1} at room temperature by a photon echo technique [134]. These parameters are summarised in Table 5.1.

	τ (ns)	Γ_{DOS} (cm^{-1})	Γ_{hom} (cm^{-1})
MeLPPP	≤ 0.2	690	260 [54]
PPV	> 1 [39, 45, 178]	750 – 1220 [41, 144]	210 [134]

Table 5.1: Photophysical parameters for MeLPPP and PPV at room temperature. τ is the excited state lifetime, Γ_{DOS} denotes the width (FWHM) of the DOS, and Γ_{hom} stands for the homogeneous line width (FWHM).

The absence of transient behaviour in MeLPPP is interpreted to reflect the differences in the excited state lifetimes as well as the differences in the ratio between the homogeneous line widths and the widths of the DOS with respect to PPV and derivatives. Given the thermal energy present at room temperature (corresponding to about 200 cm^{-1}), it is reasonable to assume that for MeLPPP intra-DOS relaxation processes and thermally assisted uphill transfer [40] within the narrower DOS are counterbalanced within the rel-

atively short excited state lifetime. In contrast, the slower decay and the larger width of the DOS in PPVs lead to less effective thermally assisted processes, and consequently the excitations may equilibrate within the DOS during the longer lifetime of the excited state.

5.4.3 Excited State Lifetime

Finally, the issue of the radiative lifetime τ_{rad} of the electronically excited states of MeLPPP will be addressed. The unambiguous determination of the fluorescence lifetime is hampered by several factors. At room temperature one often observes a bi-exponential decay. The ILT analysis permitted to retrieve the excited state lifetime from the fluorescence transients despite their non-exponential behaviour. Moreover, the lifetimes, that were measured for different samples, varied between 100 ps and 200 ps. Such variations have been observed previously [155, 182] and were attributed to trapping processes of mobile electronic excitations at randomly distributed defects with subsequent non-radiative quenching of the excitation energy [178, 182]. Since MeLPPP is characterised by a very low concentration of chemical impurities [7], it is likely that the defects are introduced by the film preparation [30] which may slightly vary from sample to sample. Accordingly, the longest lifetime of 200 ps is interpreted to result from an MeLPPP-film that comes closest to an ideal, nearly defect free sample. Thus the lifetime of 200 ps provides a lower boundary for the actual excited state lifetime in MeLPPP. Taking into account the room-temperature fluorescence quantum yield of 0.25 [62] a radiative lifetime of $\tau_{\mathrm{rad}} = 800\,\mathrm{ps}$ is obtained.

An independent piece of information concerning this issue is provided by the low-temperature experiments. Due to the strongly reduced mobility of electronic excitations at 1.5 K [178] the effect of trapping processes can be neglected for excitations in the low-energy tail of the DOS. Therefore, the decay times of about 450 – 500 ps in the low-energy wing (Fig. 5.4b, open squares and filled circles) provide a lower boundary for the lifetime of the excited state. Together with the low-temperature fluorescence quantum yield of 0.6 [62] this results in an estimate for the radiative lifetime of $\tau_{\mathrm{rad}} = 750 - 830\,\mathrm{ps}$ which is in excellent agreement with the room-temperature value.

5.5 Conclusion

In summary, picosecond time-resolved spectroscopy with high spectral resolution was employed on MeLPPP-films both at 1.5 K and at 296 K. An inverse Laplace transform of the fluorescence decay curves extracted from the high-resolution streak images demonstrated that a single-peaked distribution of decay rates, rather than a single time constant, con-

sistently describes the relaxation dynamics both at low and at room temperatures. This is ascribed to a broad distribution of nearest-neighbour transfer rates of electronic excitations caused by a distributions of nearest-neighbour distances due to the disordered sample morphologies. In addition, a distribution of oscillator strengths arising from a distribution of conjugation lengths contributes to this effect. At 1.5 K the detection energy dependence of the expectation values of the decay rate distributions and the time dependence of the spectral moments of the transient emission spectra permitted detailed insight into the time- and energy-dependent population of chromophores in the low-energy wing of the DOS from energetically higher lying sites. For the first time the rising components of the fluorescence decay curves could be retrieved from the low-temperature streak data as a function of the detection energy. In contrast, at room temperature a time- and energy-dependence of the relaxation processes was not observed. This is attributed to thermally assisted uphill migration of electronic excitations within the DOS and a substantial contribution of the homogeneous line width to the width of the DOS. Finally, the radiative lifetime (i. e. the expectation value of a lifetime distribution) of the lowest excited electronic state was determined to about 800 ps both at 1.5 K and at 296 K.

Chapter 6

Single-Molecule Spectroscopy

The combination of low-temperature single-molecule spectroscopy on MeLPPP and statistical pattern recognition techniques allows to retrieve the profile of the electronic spectra in great detail. These data allow to calculate the Debye-Waller factor, i. e. the electron-phonon coupling strength, and weak electron-phonon coupling for MeLPPP at low temperatures is found. Moreover, there is strong evidence that the low-frequency vibrational modes, which are coupled to the electronic transitions, stem from vibrations of the surrounding host matrix indicating an even weaker intra-chain electron-phonon coupling. The analysis of the zero phonon line shape of the purely electronic emission lines reveal that these lines are inhomogeneously broadened by fast unresolved spectral diffusion processes. Finally, from a detailed study of the vibronic emission lines of single MeLPPP-chains the vibrational relaxation time of the inter-ring stretching and aromatic ring CC stretching mode in the electronic ground state is determined to about 230 fs at low temperatures.

6.1 Introduction

It is consensus that the electronic properties of π-conjugated polymers are determined to a large extend by the conformation of the polymer chain [29, 30] and the prediction of such properties is of key importance for the design of novel polymers for optoelectronic devices. However, the prediction of these properties for a random chain conformation in a disordered matrix is very difficult. Hence, it would be of crucial interest to obtain detailed information about the relevant parameters that describe the electronic structure of the electronic states in conjugated polymers, i.e. the spread in the site energy of individual chromophores, the interaction strength between the chromophores, and, in particular, the strength of the electron-phonon interaction. The electron-phonon coupling strength is a

measure for the rigidity of the polymer backbone upon electronic excitation or injection of charge carriers into the polymer chain and strongly influences the mobility of electronic excitations and charge carriers [22–24, 147].

Typically, the purely electronic (0-0) transition of an organic molecule embedded in a matrix gives rise to a homogeneously broadened zero-phonon line (ZPL) accompanied by a relatively broad phonon-side band (PSB) [190]. The ZPL results from the purely electronic transition and the PSB from an electronic transition and the simultaneous excitation of vibrational modes (phonons) in the local environment of the emitting chromophore. The intensity ratio between the ZPL and the PSB, i.e. the profile of the electronic spectrum, is determined by the electron-phonon coupling strength. A measure for the electron-phonon coupling strength is provided by the Debye-Waller factor α (see section 2.2.3).

Another issue that is subject to controversial debate concerns the homogeneous line width of optical transitions in conjugated polymers. This is an important factor to calculate the spectral overlap and hence the excitation energy transfer rates between chromophores as discussed in section 2.3. On the one hand, resonant Rayleigh scattering and fs-fluorescence interferometric measurements on bulk samples of PPV revealed total dephasing times of the order of 200 – 500 fs at low temperatures [191, 192]. These dephasing times translate into a homogeneous line width of about 20 – 50 cm^{-1} (see section 2.2.3). Such widths of emission lines of individual chromophores were indeed observed by low-temperature single-molecule fluorescence spectroscopy on various conjugated polymers (MEH-PPV, MeLPPP, and polyfluorenes), and interpreted to represent the homogeneous line width [52,54,91,130, 193]. On the other hand, for MeLPPP with an excited state lifetime of about 500 ps (see chapter 5), a lifetime-limited homogeneous line width of 0.01 cm^{-1} is expected at very low temperatures. Given the widely accepted molecular picture of conjugated polymers [21,29, 30], such narrow lines should be observable at very low temperatures, where pure dephasing processes are suppressed. In addition, the lifetimes of the vibrational levels in the electronic ground state and the lowest electronically excited state (i. e. the homogeneous line widths of vibronic transitions) in conjugated polymers are also controversially discussed. From time-resolved measurements a vibrational relaxation of the order of 200 fs has been found for the lowest electronically excited singlet state [39, 42, 108]. However, for the electronic ground state recent single-molecule fluorescence spectroscopy experiments suggested significantly longer vibrational relaxation of the order of several picoseconds [130, 194].

The great difficulty in determining the various parameters that play a role for the description of the electronic structure of conjugated polymers is the fact that the optical ensemble spectra are inhomogeneously broadened as a result of the large heterogeneity in the polymer samples [21, 29, 30, 49]. Therefore, conventional optical spectroscopy, which

averages over large ensembles, provides only limited information about the properties of the electronic states. To avoid this complication single-molecule techniques have been employed by several groups [49, 52–55, 57–61, 130, 194]. However, any variation in the local environment of the emitting chromophore leads to changes of the local interactions and concomitantly to fluctuations of the electronic levels. In the optical spectra these fluctuations show up as spectral shifts of the optical transition on various time scales (spectral diffusion, see section 2.2.4). As a consequence of this, even for single polymers, the PSB and the homogeneous line width of the ZPL can not be retrieved due to temporal averaging during data acquisition.

In order to reveal the electron-phonon coupling strength and to address the issue of the homogeneous line width in conjugated polymers low-temperature single-molecule fluorescence spectroscopy on MeLPPP-chains in combination with a multivariate statistical pattern recognition algorithm [195,196] was employed. This allowed to resolve the spectral profile of the 0-0 as well as of the vibronic emission lines and to determine the electron-phonon coupling strength in MeLPPP directly despite strong spectral diffusion processes and noisy single-molecule spectra.

6.2 Experimental

In order to perform fluorescence spectroscopy on individual MeLPPP-chains, these were embedded in either *n*-hexadecane (HD) or polystyrene (PS) as described in section 3.1.2. The single MeLPPP-chains were excited by the frequency doubled Titanium:Sapphire laser (frequency doubler: Model 3980) operating at 430 nm with a repetition rate of 81 MHz and a pulse width of 1.5 ps (FWHM) through the home-built low-temperature microscope. This microscope can be operated either in confocal or in widefield mode. The fluorescence of individual MeLPPP-chains passed through a set of dielectric filters (HQ 500/100, AHF), was spectrally dispersed in a spectrograph (SpectraPro-150 or 250 IS), and was imaged onto the sensitive CCD camera. The spatial selection of individual MeLPPP-chains took place as follows. First, the microscope was operated in widefield mode, where an area of 20 $\times$ 20 μm^2 of the sample is illuminated. The fluorescence from this region was imaged onto the CCD camera through the spectrographs in imaging mode (mirror in the SpectraPro-150 spectrograph; 0^{th} order diffraction by the grating in the 250 IS spectrograph). A spatially well-isolated chain was chosen from this image. Then the microscope was switched to the confocal mode, i. e. the widefield lens was removed from the excitation light path and the spectrographs were operated in spectroscopy mode (SpectraPro-150: 600 lines/mm grating,

250 IS: 1800 lines/mm grating). Additionally, the focus of the objective was moved by means of a telecentric lens system such that the excitation volume and the position of the isolated polymer chain coincided. Finally, several hundreds to thousands of fluorescence spectra from this chain were successively acquired with an integration time of 1 s, which allows to obtain information on the spectral dynamics.

6.3 Results

For a detailed study of the spectral profiles of the 0-0 and vibronic transitions several hundreds of emission spectra from an individual chromophore were recorded successively with an integration time of 1 s. Examples are shown in Fig. 6.1, where stacks of 1000 and 200 consecutively acquired fluorescence spectra of a single MeLPPP-chain either embedded in HD (Fig. 6.1a, top) or PS (Fig. 6.1b, top) are displayed. The most intense features in these spectra are identified as the purely electronic (0-0) transitions of individual chromophores and their "spectral trails" can be followed throughout the stacks of spectra (Fig. 6.1, boxed regions labelled I). In addition, a less intense doublet of lines is observed in Fig. 6.1 (boxed regions II and III). These lines are offset to lower energies from the corresponding 0-0 transitions by about 1300 cm^{-1} and 1560 cm^{-1}, respectively, and are ascribed to vibronic transitions involving the inter-ring stretching vibration (1300 cm^{-1}) and the aromatic-ring CC stretching mode (1560 cm^{-1}).

The individual spectra are typically extremely noisy, as evidenced by the examples presented in the insets of Fig. 6.1 (bottom), and do not allow for a quantitative analysis of the profile of the electronic and the vibronic transitions. The averages of all 1000 and 200 individual spectra are shown at the bottom of Fig. 6.1 and feature relatively broad and structureless bands. The line widths of the 0-0 transitions amount to 75 cm^{-1} (FWHM) for MeLPPP in HD and to 45 cm^{-1} for MeLPPP in PS, respectively. The line widths of the vibronic transitions are slightly broader with about 80 – 120 cm^{-1}. These findings are in agreement with recent results on MeLPPP obtained by others, where line widths of the 0-0 and vibronic emission lines of individual chromophores of several tens of wavenumbers were found [52,54]. From the data presented in Fig. 6.1 it is apparent that the main contribution to the line width of the time-averaged spectra stems from spectral diffusion processes reflecting fluctuations in the local environment of the emitting site (see section 2.2.4). As a consequence of the spectral fluctuations, a quantitative analysis of the individually recorded spectra within a stack as well as of the time-averaged spectra is very difficult.

In order to overcome these limitations the stacks of spectra were divided into three spec-

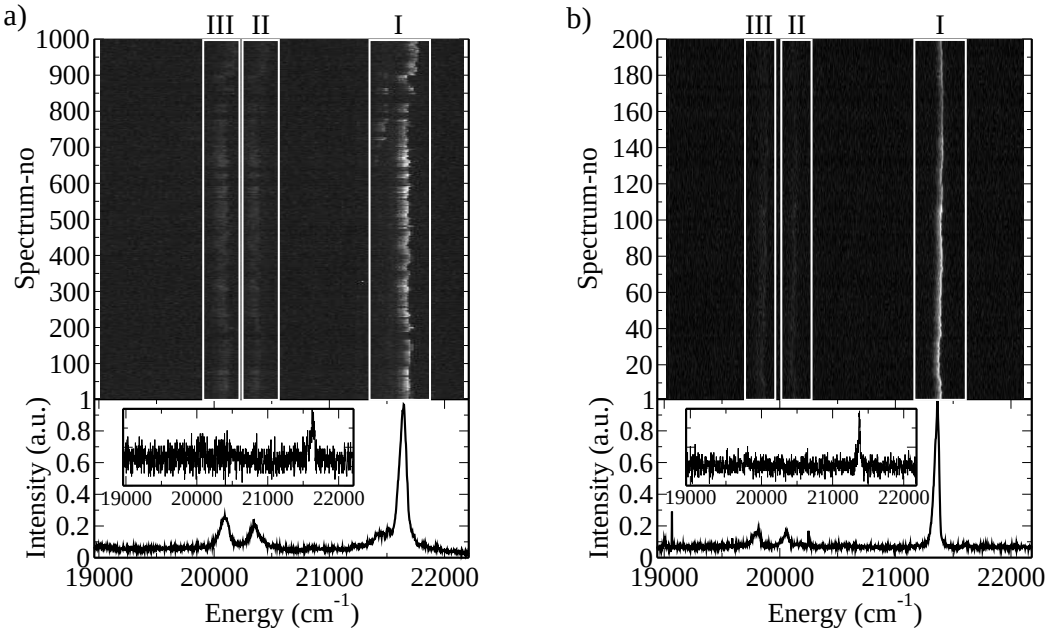

Figure 6.1: Two-dimensional representation of 1000 and 200 fluorescence spectra of individual MeLPPP-chains embedded in *n*-hexadecane (a) and polystyrene (b), respectively. The individual spectra have been recorded consecutively with an integration time of 1 s at a temperature of 1.5 K. The horizontal axis corresponds to energy, the vertical axis to the spectrum number or equivalently to time, and the emission intensity is given by the grey scale. The corresponding total averages of all 1000 and 200 spectra, respectively, are depicted at the bottom of each pattern. The insets show examples of individual spectra extracted from the respective stacks of spectra (spectrum no. 265 for MeLPPP in HD and spectrum no. 160 for MeLPPP in PS). a) MeLPPP in HD: the intense line at 21640 cm^{-1} corresponds to the purely electronic transition of an individual chromophore (enclosed in the boxed region I), and the lines between 20000 cm^{-1} and 20500 cm^{-1} are ascribed to vibronic transitions of this site (boxed regions II and III). b) MeLPPP in PS: the 0-0 transition is centred at 21360 cm^{-1} (boxed region I), and the corresponding vibronic transitions of this chromophore are between 19700 and 20200 cm^{-1} (boxed regions II and III).

tral regions (Fig. 6.1, boxes I – III). The emission lines in each region were analysed separately by means of a multivariate statistical pattern recognition algorithm (MSA; IMAGIC, ImageScience). This approach has been demonstrated to be a valuable tool to retrieve the profiles of electronic spectra from individual objects in disordered systems [197, 198]. In the MSA-analysis each individual spectrum in a stack of spectra (e.g. Fig. 6.1a, top) is interpreted as a one-dimensional image. By pattern recognition these spectra are grouped into a predetermined number of classes (here typically 5 – 10) according to their statistical similarity, such that the variance between the classes is maximised and the total intra-class

variance is minimised (in a mathematical least-squares sense). From this procedure the class-averaged spectra (CAS) are obtained, i.e. the average of only those individual spectra that have been assigned to a particular class. In simple words, this algorithm ensures that only those individual spectra are averaged which are "sufficiently similar". Further details about this algorithm can be found in Refs. [195, 196] and its applicability to spectroscopy has been discussed in detail in Refs. [197, 198]. The achievement of this approach is that contributions to the line width from spectral diffusion processes, occurring on time scales slower than the integration time for the individual spectra (here: 1 s), are eliminated. Hence, the spectra from an individual chromophore can be registered with a drastically reduced spectral line width without the usual trade-off between spectral and/or temporal resolution versus signal-to-noise ratio.

6.3.1 Statistical Analysis of the Purely Electronic Emission Lines

An expanded view of the purely electronic emission lines (Fig. 6.1a and b, boxes labelled I) for MeLPPP embedded in HD and PS is shown in Fig. 6.2a and c (top), respectively. Strong spectral diffusion processes of the optical transitions are apparent for both matrix materials. Looking at the spectral diffusion patterns in more detail reveals that relative changes of the spectral position of the 0-0 emission between two consecutively acquired individual spectra occur mainly on an energy scale of about $1 - 5\,\mathrm{cm}^{-1}$. Larger spectral changes of up to $70\,\mathrm{cm}^{-1}$ are also found, although much less frequently (e. g. between spectra 10 and 30 in Fig. 6.2c, top).

For the MSA-analysis of the stacks of 1000 and 200 spectra presented in Fig. 6.2a,c (top) the IMAGIC software was set to classify the individual spectra into 10 and 5 classes, respectively. This results in about 40 – 100 spectra per class and the signal-to-noise ratios of the class-averaged spectra are increased by a factor of more than 6 with respect to the individual spectra. Three examples of the corresponding electronic CAS are shown in Fig. 6.2b and d, respectively. The recurrent motif in the spectral profiles of the CAS is a sharp line and a shoulder in the low-energy wing. Accordingly, the narrow feature is assigned to the ZPL and the broad feature in the low-energy tail of the ZPL to the PSB of the transition.

For a quantitative analysis of the spectral profile of the electronic CAS the high-energy tail of the ZPLs was fitted by either a Lorentzian or a Gaussian function, whichever was appropriate (see below). This procedure allowed to determine the line shape as well as the line width (FWHM) of the ZPL. In the next step the corresponding fit function was subtracted from the CAS to uncover the remaining PSB, as shown in the insets of Fig. 6.2b

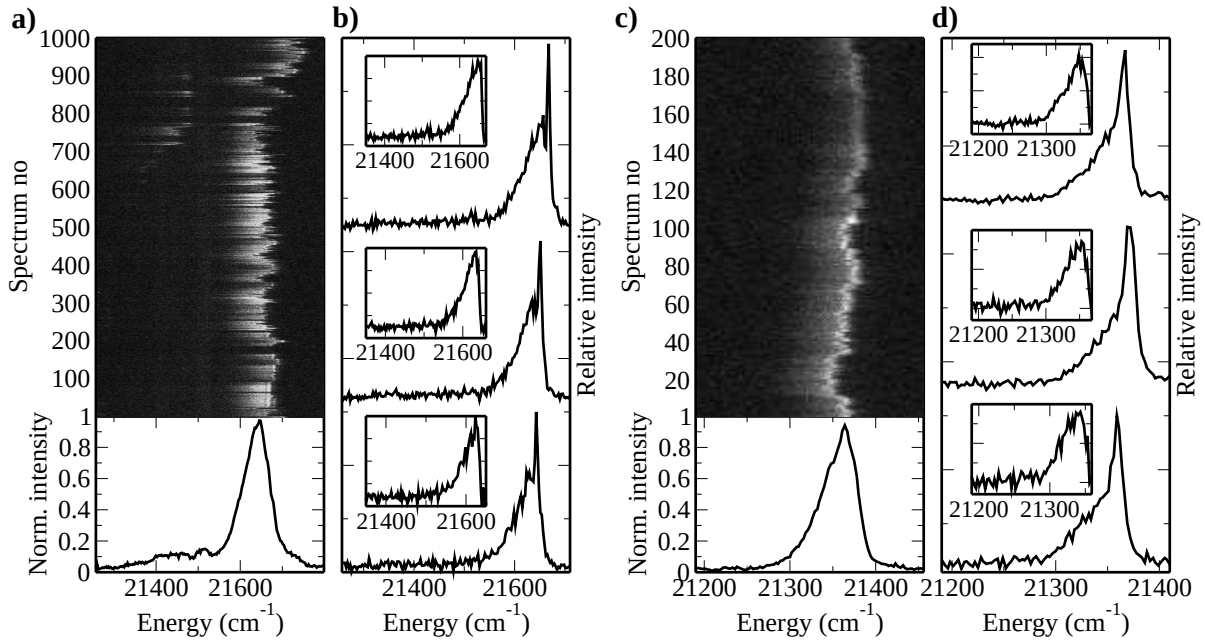

Figure 6.2: a) and c) Enlarged views of the purely electronic (0-0) transitions of the single-molecule emission spectra (Fig. 6.1, boxed regions labelled I) for MeLPPP embedded in *n*-hexadecane and polystyrene, respectively. The corresponding total averages of all 1000 and 200 spectra are depicted at the bottom of each pattern and feature line widths (FWHM) of $75\,\mathrm{cm}^{-1}$ (MeLPPP in *n*-hexadecane, Fig. 6.2a) and $45\,\mathrm{cm}^{-1}$ (MeLPPP in polystyrene, Fig. 6.2c). b) and d) Results of the statistical analysis. Three examples of normalised class-averaged spectra that have been obtained by the application of the MSA-algorithm to the stacks of fluorescence spectra. The insets show an expanded view of the phonon side bands after subtraction of a Lorentzian or Gaussian (see text) that has been fitted to the high-energy tail of the zero-phonon lines.

and d, and the PSB was then numerically integrated. From these data the Debye-Waller factor α and the mean phonon energy ω_m were determined. The latter is the peak energy of the PSB with respect to the centre energy of the ZPL (see section 2.2.3). In principle the analysis of the line shapes and line widths of the PSBs would allow to retrieve e. g. the spectral density of phonon states [199, 200]. However, as will be shown below this provides information about the host matrix (HD and PS), which is not of interest in this context.

The analysis of the ZPL line shapes of the CAS revealed that these are not always Lorentzian, but also a significant fraction of Gaussian as well as triangular shapes of the ZPLs was found. In Fig. 6.3 three examples of CAS (black line) with a Lorentzian (a), Gaussian (b), and triangular line shape (c) are presented together with the corresponding fit functions (red and blue curves). Lorentzian (blue) and Gaussian line shapes (red) can be

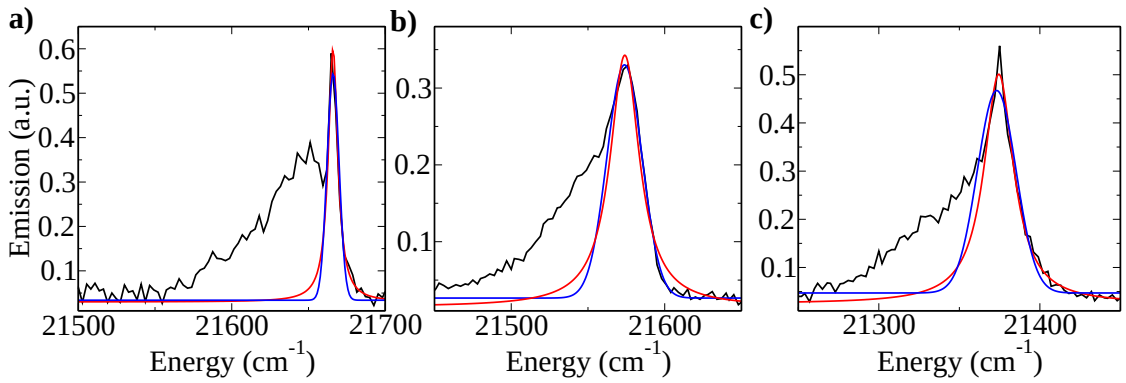

Figure 6.3: ZPL line shapes observed in the class-averaged spectra of the 0-0 emission of MeLPPP. The black line represents the CAS and the red and blue curves show Lorentzian and Gaussian fits, respectively, to the high-energy tail of the CAS. a) Lorentzian ZPL, b) Gaussian ZPL, and c) triangular ZPL line shape.

		Line shape		
host	total # of CAS	Lorentzian	Gaussian	triangular
HD	147	86 59 %	49 33 %	12 8 %
PS	321	158 49 %	131 41 %	32 10 %

Table 6.1: Total number of investigated class-averaged spectra of the 0-0 emission together with the numbers and ratios of the observed ZPL line shapes for MeLPPP embedded in HD and PS, respectively.

discriminated by a comparison of particularly the highest-energy tails of the CAS with the respective fit functions (Fig. 6.3a,b). The triangular ZPLs show a distinct deviation from the fit function at the peak position of the ZPL, while the high-energy tail regions of such ZPLs are usually compatible with a Lorentzian function (Fig. 6.3c). For MeLPPP embedded in HD in total 147 CAS were analysed, where 86 CAS (59 %) exhibited a Lorentzian ZPL line shape, 49 CAS (33 %) had a Gaussian ZPL line shape, and for 12 CAS (8 %) we found a triangular ZPL shape. The data for MeLPPP in PS revealed similar percentages. Here, a total of 321 CAS was analysed and 158 CAS (49 %) showed a Lorentzian ZPL line shape, 131 CAS (41 %) exhibited a Gaussian shape, and 32 CAS (10 %) had a triangular ZPL shape. These numbers are summarised in Table 6.1.

The distributions of the line width of the ZPL, the Debye-Waller factor, and the mean phonon energy are shown in Fig. 6.4 for MeLPPP embedded in HD (top) and PS (bottom), respectively. For MeLPPP in HD (PS) the line widths of the ZPLs are distributed between 1.4 and 38 cm^{-1} (7 and 45 cm^{-1}), and both distributions peak at 12 cm^{-1} (Fig. 6.4a). Note that the lower boundaries of these distributions are not determined by the spectral resolution of the setup. These ZPL line widths of the electronic CAS are significantly smaller than the line widths of the time-averaged spectra (e. g. Fig. 6.2a,c, bottom), which is a result of the application of the MSA-algorithm for data analysis. The distributions of the Debye-Waller factor α (Fig. 6.4b) feature a peak at about 0.5 and cover a range from 0.25 – 0.9 irrespective of the host material, which is in general indicative of weak electron-phonon coupling. In contrast to the histograms of the line widths of the ZPLs and the Debye-Waller factors, the distributions of the mean phonon energies ω_m, depicted in Fig. 6.4c, are clearly different for the two host materials. The distribution of ω_m for MeLPPP in HD (Fig. 6.4c, top) has a bimodal structure with maxima at 20 cm^{-1} and 38 cm^{-1}, whereas for MeLPPP in PS (Fig. 6.4c, bottom) this distribution is centred at 30 cm^{-1} and appears broader as compared to the distribution for MeLPPP in HD.

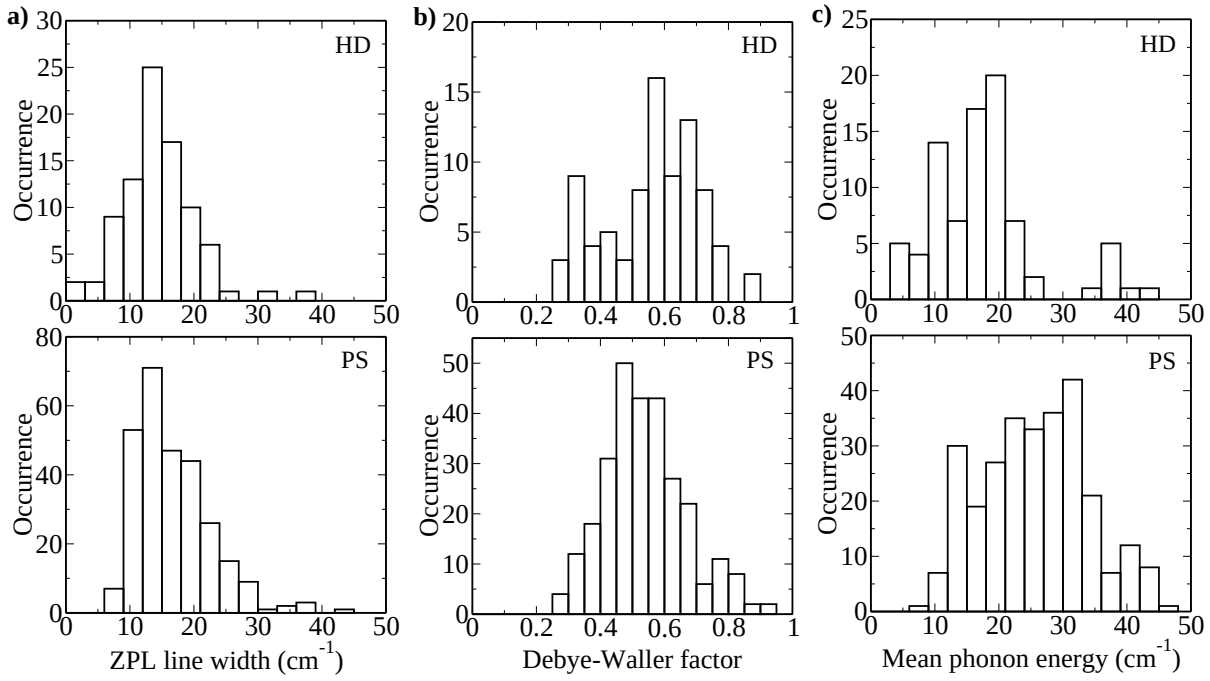

Figure 6.4: Histograms of the parameters determined from the class-averaged spectra for MeLPPP embedded in HD (top) and PS (bottom). a) Line width of the ZPL. b) Debye-Waller factor α. c) Mean phonon energy ω_m.

6.3.2 Statistical Analysis of the Vibronic Emission Lines

The vibronic emission lines (Fig. 6.1a,b, boxed regions II and III) of single chromophores are presented in an enlarged view in Fig. 6.5 (top) for MeLPPP embedded in HD (a) and PS (c), respectively, and the corresponding time-averaged spectra are shown below.

The MSA-analysis was performed separately for each of the stacks of fluorescence spectra enclosed in the boxed regions II and III and examples of the resulting vibronic class-averaged spectra for the transitions II and III are shown in Fig. 6.5b,d. The CAS of the two vibronic transitions show distinct differences. For the high-energy vibronic lines (Fig 6.5 bands II) about 50 % of the CAS exhibit the same recurrent motif as the electronic (0-0) CAS, as presented above, and comprise a (more or less) sharp line and a shoulder in the low-energy tail (e. g. Fig. 6.5b, II). This shape is assigned to the zero phonon line and the phonon side band of the vibronic transition. However, the remaining 50 % of the vibronic CAS of the high-energy vibronic lines are rather symmetric and a sub-structure (ZPL with

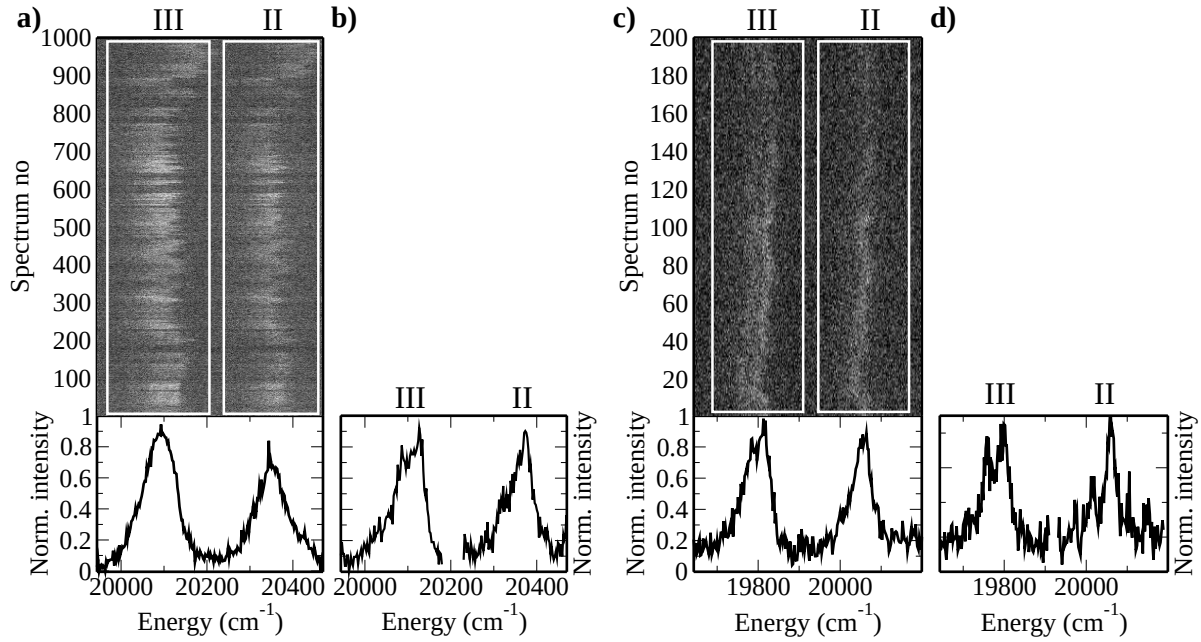

Figure 6.5: a) and c) Expanded views of the vibronic transitions of the single-molecule emission spectra displayed in Fig. 6.1 (boxes marked with II and III) for MeLPPP embedded in HD (a) and PS (c), respectively, and the results of the multivariate statistical analysis. The corresponding total averages are shown at the bottom of each stack of spectra. b) and d) Examples of normalised vibronic class-averaged spectra of the bands labelled II and III that have been calculated with the IMAGIC programme from the stacks of fluorescence spectra. The CAS have been obtained for each transition (II and III) separately.

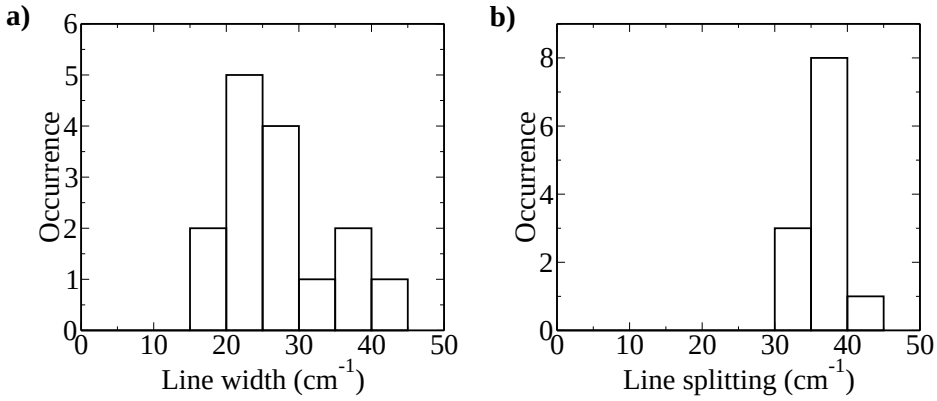

Figure 6.6: a) Histogram of the line widths of the vibronic class-averaged spectra. b) Distribution of the line splitting observed in the low-energy vibronic transitions (bands III in Fig. 6.5b,d). Both distributions contain the data for MeLPPP in both HD and PS.

PSB) can not be resolved (e. g. Fig. 6.5d, II). This may be ascribed to the rather low signal-to-noise and signal-to-background ratio of these vibronic CAS. In contrast, the vibronic CAS of the low-energy vibronic emission lines *always* feature a shoulder in their low-energy wings (Fig. 6.5b,d, III).

Owing to the low signal-to-noise and signal-to-background ratio of the vibronic CAS a simpler approach for their quantitative analysis has been chosen as compared to that for the electronic CAS. Debye-Waller factors and mean phonon energies were not evaluated for the vibronic CAS, because these data exhibit a high degree of uncertainty. Only the line widths of the CAS of both vibronic lines (II and III) were determined by fitting a Lorentzian function to the respective high-energy tails. For the lower-energy vibronic CAS (labelled III) additionally the sum of two Lorentzian functions was fitted. From this the spectral separation between the centre energies of the two Lorentzians was obtained, which is referred to as line splitting in the following for reasons that will be discussed in section 6.4.3.

The results of the quantitative analysis are presented in Fig. 6.6, where the line widths of the vibronic CAS (a) and the line splitting of the low-energy CAS (b) are displayed. Since the vibronic lines of single chromophores are typically very weak with a small signal-to-background ratio, this procedure could be performed for the spectra of only few chromophores. Therefore the distributions in Fig. 6.6 contain the data for MeLPPP in both HD and PS. The line widths of the vibronic CAS are distributed between 15 and 45 cm^{-1} and peak at 23 cm^{-1} (Fig. 6.6a). Thus the line widths of the vibronic lines are on average about 10 cm^{-1} broader with respect to the ZPLs of the 0-0 emission (see Fig. 6.4a). The distribution of the line splitting has a maximum at 38 cm^{-1} and covers a range from

$30\,\mathrm{cm}^{-1}$ to $45\,\mathrm{cm}^{-1}$ (Fig. 6.6b).

6.4 Discussion

6.4.1 Electron-Phonon Coupling

The most striking feature observed in the class-averaged spectra of the purely electronic 0-0 emission lines of MeLPPP (Fig. 6.2b,d) is their spectral profile comprising a sharp ZPL and an accompanied PSB in the low-energy wing. In principle, this profile can be also recorded by means of line narrowing ensemble techniques at low temperatures, such as site-selective fluorescence (SSF) or hole burning (HB) spectroscopy [106, 132, 133, 201]. For short chain oligomers [oligo(*p*-phenylene) and oligo(*p*-phenylenevinylene)] with up to 4 repeating units narrow ZPLs with associated PSBs could indeed be resolved by low-temperature SSF, which indicates weak electron-phonon coupling in the oligomers [29, 202]. However, for longer oligomers and the corresponding polymers [(Me)LPPP, PPV] both SSF and HB yielded broad and structureless bands with line widths of the order of $100\,\mathrm{cm}^{-1}$ [29,148,149, 202–204]. This finding for the polymers can be attributed either to strong electron-phonon coupling, for which a ZPL can not be observed in the optical spectra (see section 2.2.3), or to unresolved spectral diffusion processes of the optical transitions, which leads to a line broadening and thus to a washing-out of the spectral profile. The data presented in this work (Fig. 6.2a,c) clearly demonstrate that the optical transitions in conjugated polymers are subject to strong spectral diffusion processes causing relatively broad and unstructured time-averaged spectra of single chromophores (Fig. 6.2a,c, bottom). Given the fact that both SSF and HB are ensemble techniques, this leads to the conclusion that the latter interpretation for the broad bands observed in SSF and HB spectra holds, i. e. the spectral profile recorded in these experiments is washed out by strong spectral diffusion processes. Hence, a ZPL with PSB in the optical spectra of conjugated polymer samples can not be resolved by ensemble methods.

The approach presented in this work, low-temperature single-molecule fluorescence spectroscopy in combination with a statistical pattern recognition technique, allowed to resolve the spectral profile of the optical transitions of individual chromophores in great detail. This permitted to determine the Debye-Waller factor (the electron-phonon coupling strength) for low-energy phonon modes coupled to the electronic states in conjugated polymers for the first time. The distributions of the Debye-Waller factor α both for MeLPPP in HD and for MeLPPP in PS (Fig. 6.4b) yield a mean value of $\alpha = 0.5$ independent of the matrix material. This indicates weak electron-phonon coupling strength in MeLPPP

at low temperatures.

The obvious question that arises concerns the origin of the low-frequency vibrations coupled to the electronic transition. On the one hand, from HB, SSF, and single-molecule studies on low-molecular weight molecules in inert matrices it was found that low-energy vibrational modes of the host are excited in combination with an electronic transition of the chromophore [104–107]. On the other hand, a conjugated polymer constitutes a multichromophoric macromolecule, where the emitting site is localised on a rather small subunit of the polymer. Additionally, the chains exhibit typically a coiled conformation [28, 30,49]. For that reason it has been suggested that the remainder of the conjugated polymer chain might form an effective matrix for the emitting site and the host matrix has only a limited effect [52, 130]. In order to address this issue the distributions of the mean phonon energies for MeLPPP in HD and PS, respectively, have been analysed, which exhibit distinct differences for the two host materials (Fig. 6.4c).

Insight into the nature of the phonon modes of the matrix materials can be obtained from inelastic neutron scattering on pure HD and PS samples, respectively [205–208]. In order to facilitate comparisons with the results from those experiments, the histograms of the mean phonon energies are shown again in Fig. 6.7, where the distributions have been divided by ω_m^2 for this presentation.

For HD, unfortunately, neutron scattering experiments at 25 K did not allow for the detection of vibrational modes with energies below $20\,\mathrm{cm}^{-1}$ and only a vibrational mode at about $37\,\mathrm{cm}^{-1}$ could be detected [205]. However, such experiments on *n*-octadecane (OD), an *n*-alkane that is slightly longer than HD, revealed two modes with energies of $17\,\mathrm{cm}^{-1}$ and $45\,\mathrm{cm}^{-1}$ at 25 K which were assigned to intra-molecular modes of the *n*-alkane chain [205,208]. The frequencies of the modes obtained by neutron scattering are indicated in Fig. 6.7a by the full arrow for HD and the dashed arrows for OD. Taking into account the different length of OD with respect to HD, which is reflected by the frequency shift of the mode at higher energy from $45\,\mathrm{cm}^{-1}$ to $37\,\mathrm{cm}^{-1}$, the phonon frequencies found by neutron scattering are in good agreement with the mean phonon frequencies obtained by the single-molecule experiments.

For amorphous materials, such as PS, a universal feature that can be observed in neutron scattering as well as in Raman spectroscopy is the so called Boson peak at energies between $10 - 70\,\mathrm{cm}^{-1}$ [104,206,207,209]. This peak corresponds to a maximum in the ratio $\mathrm{G}(\omega)/\omega^2$, where $\mathrm{G}(\omega)$ denotes the density of phonon states and ω the phonon frequency. The microscopic origin of the Boson peak was suggested to be due to the presence of interacting quasi-localised low-frequency modes in amorphous materials [104, 209]. In Fig. 6.7b the distribution of mean phonon energies derived from the single-molecule experiments

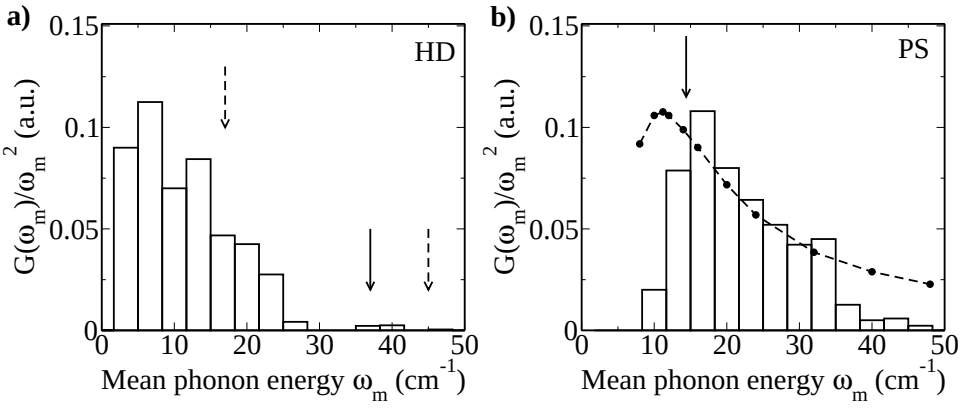

Figure 6.7: Distributions of the mean phonon energy ω_m, which have have been divided by ω_m^2 for better comparison with literature data. $G(\omega_m)$ denotes the density of phonon states. a) The distribution of ω_m for single MeLPPP-chains embedded in *n*-hexadecane (bars). The arrows indicate the energetic positions of low-frequency modes that have been obtained by inelastic neutron scattering on *n*-alkanes at 25 K: the full arrow marks the position of a low-energy mode at 37 cm^{-1} in *n*-hexadecane [205] and the dashed arrows indicate two low-energy modes at 17 and 45 cm^{-1} in *n*-octadecane [205, 208]. b) The distribution of ω_m for single MeLPPP-chains in polystyrene (bars). The filled circles reproduce the boson peak of polystyrene which has been obtained by inelastic neutron scattering at 80 K [207]. The arrow marks the peak position (14.4 cm^{-1}) of the boson peak measured by inelastic neutron scattering on polystyrene at 10 K [206].

on individual MeLPPP-chains in PS (bars) are compared with the Boson peak of PS obtained by inelastic neutron scattering experiments at 80 K (filled circles, from Ref. [207]). Note that the two data sets are superimposed without adjusting any parameters. The arrow in Fig. 6.7b marks the position of the maximum of the Boson peak for PS obtained at 10 K [206] which is closer to the experimental conditions in this work. As evidenced by Fig. 6.7b the data from the two independent experimental approaches, i.e. neutron scattering and single-molecule spectroscopy, are in reasonable quantitative accordance.

These comparisons both for MeLPPP in HD and MeLPPP in PS provide strong evidence that the phonons giving rise to the PSB in the optical spectra of individual MeLPPP-chains correspond to low-energy vibrational modes of the host matrix rather than to intramolecular modes of MeLPPP and its side groups. However, from these data it can not be fully ruled out that low-frequency vibrational modes of MeLPPP contribute to the observed PSBs as well. Quantum chemical calculations for ladder-type *para*-phenylene oligomers yielded an intra-molecular longitudinal acoustic mode with significant electron-phonon coupling strength [81, 103]. The energy of this mode varied between 60 – 160 cm^{-1} de-

pending on the oligomer length and the computational method [81, 103]. In addition, a low-frequency mode with an energy of about $100\,\mathrm{cm}^{-1}$ has been observed in some Raman spectra of MeLPPP-films (however, the assignment of this vibration is unclear) [29, 148].

In order to exclude this option single-molecule fluorescence spectroscopy has been recently performed at 1.5 K on MeLPPP-chains that were directly spin-coated onto a quartz-substrate without any matrix [210]. In these data the CAS of the 0-0 emission lines of single sites appeared very symmetric and these lines were assigned to the ZPL of the purely electronic 0-0 transitions [210]. In other words, in the absence of a host matrix only purely electronic transitions without simultaneous excitation of low-frequency modes are observed within experimental accuracy.

An important consequence of the weak electron-phonon coupling strength in MeLPPP concerns the structural relaxation of the polymer backbone or the environment of the chromophore when going from the ground state to the electronically excited state or *vice versa* going from the electronically excited state to the ground state (see section 2.3). The reorganisation or relaxation energy associated with this process is given by $\epsilon = S\hbar\omega$ [see eq. (2.32)], with the Huang-Rhys parameter $S = -\ln\alpha$ and the phonon energy $\hbar\omega$. From a mean Debye-Waller factor of $\alpha = 0.5$ (Fig. 6.4b) it follows $S = 0.7$, and together with a mean phonon energy of about $25\,\mathrm{cm}^{-1}$ taken from the distributions in Fig. 6.4c a relaxation energy of $\epsilon \approx 17\,\mathrm{cm}^{-1}$ is calculated for MeLPPP at 1.5 K. This value is very small for a conjugated polymer [20, 22, 76, 81] and arises from relaxation of the surrounding medium, because S and $\hbar\omega$ describe the coupling with matrix phonons rather than with intra-molecular modes of the MeLPPP-backbone. This reflects the structural rigidity of this double-stranded ladder-type polymer, which does not allow for large changes of its equilibrium geometry upon electronic excitation into the lowest electronically excited state or decay into the electronic ground state. These findings are in contrast to conjugated polymers with librational/torsional degrees of freedom of phenylene- or thiophene-rings in the backbone, such as PPVs and PTs. In these systems the coupling to intra-molecular low-energy torsional modes with an energy of about $100\,\mathrm{cm}^{-1}$ is predicted to lead to significant structural changes in the lowest electronically excited state as compared with the electronic ground state. In particular, a planarisation of the polymer backbone in the electronically excited state upon photoexcitation is expected [20, 22, 46, 76, 81].

As mentioned in section 2.3, particularly low-energy phonon modes, that couple to the electronic states, strongly influence the transfer rates of electronic excitations [22, 24]. Owing to the very small reorganisation energy ϵ found in this work for MeLPPP at low temperatures, the Stokes shift between the donor and acceptor site, involved in the energy transfer process, is small as well. Therefore the spectral overlap between these

chromophores is large and enhances the rates for excitation energy transfer [22, 24]. This is also consistent with the fast energy migration processes that have been described in chapter 5.

6.4.2 Spectral Diffusion

Origin of the Spectral Diffusion Processes

As discussed above the strong spectral diffusion processes of the optical transitions prevented to resolve the PSB in the optical spectra of MeLPPP (see e. g. Fig. 6.1) and other conjugated polymer systems by line narrowing techniques as yet [29, 52, 148, 149, 194, 202–204, 211]. The spectral diffusion trails found for MeLPPP in both HD and PS (Fig. 6.1) closely resemble those found for a small organic molecule [terrylenediimide (TDI)] embedded in the amorphous matrix poly(methylmetacrylate) (PMMA) by low-temperature single-molecule fluorescence spectroscopy [138, 212]. In these experiments changes of the spectral position of the emission lines of TDI between subsequent spectra of several wavenumbers were observed [138, 212], which is in agreement with the numbers found here for MeLPPP in both HD and PS. Since the spectral diffusion processes are caused by fluctuating matrix units in the local environment of the emitting sites (see section 2.2.4), these observations lead to the conclusion that for MeLPPP the immediate environment of the emitting chromophores exhibits a highly disordered (amorphous) structure leading to strong spectral diffusion processes independent of the host material.

Whereas for MeLPPP in PS this is not surprising, because PS-films as prepared in this work are amorphous, for the HD host a different behaviour could be expected at first sight. Because the MeLPPP/HD samples were rapidly cooled to 1.5 K (see section 3.1.2), HD might form a Shpol'skii matrix [158, 159]. Irrespective of the detailed structure of a Shpol'skii matrix, which is still not entirely clear [157–159], such a host usually provides a reasonably well-defined local surrounding for the chromophores insofar as the number of fluctuating matrix units in HD in the immediate environment of an emitting chromophore is significantly reduced with respect to an amorphous host [138, 158, 159, 212]. Hence, for MeLPPP in HD the spectral diffusion processes of the optical transitions should be absent or at least less pronounced [138, 212] as compared with the system MeLPPP in PS. However, this is obviously not the case for MeLPPP in HD and may be attributed to the long and flexible side groups bound to the MeLPPP-backbone that prevent the formation of a Shpol'skii matrix at least in the immediate surrounding of emitting chromophores (besides other factors that influence the formation of a Shpol'skii matrix [158, 159], which

will not be discussed here).

To shed some light on the nature of the TLS, that cause the spectral diffusion processes of the optical transitions, an estimation based on the sudden jump model [137] will be done, which was introduced in section 2.2.4. For simplicity, it is assumed that the interaction between the TLS and the chromophore is only a function of their respective distance R and is of dipole – dipole type (see section 2.2.4). All further parameters that enter the expression describing this interaction [137] will be neglected, i. e. the TLS – chromophore coupling constant, specific properties of the TLS (asymmetry, energy splitting), as well as the mutual orientation between the elastic or electric dipole moment associated with the fluctuating matrix unit and the dipole moment of the chromophore. These latter parameters are unknown and not accessible from the experiments presented in this work. Then the relative changes of the spectral position of the emission lines $\Delta\nu$ between consecutively recorded individual spectra (spectral jumps) are given by a R^{-3} distance dependence [see eq. (2.22)].

The vast majority of the observed spectral jumps was found to be of the order of several wavenumbers (1 – 5 cm^{-1}) and consequently stem from interactions with distant TLS in this approximation. Possible candidates for such TLS are fluctuating units in the PS or HD matrix, which is shielded from the emitting sites by the long and bulky side groups of MeLPPP. Some spectral jumps are much larger and occur on energy scales of up to 70 cm^{-1}, which are caused by fluctuating units that are much closer to the emitting chromophore. These TLS can be tentatively attributed to e. g. librations/torsions of the phenylene-rings or methyl-groups in the side chains, which are very close to the backbone (Fig. 6.8). In particular, torsional motions of CH_3-groups are known from hole burning experiments to give rise to spectral diffusion [213].

This assignment is supported by a simple estimation. According to eq. (2.22) and together with the approximations introduced above, the ratio between the smallest ($\Delta\nu_1 = 1\,\mathrm{cm}^{-1}$) and largest observed spectral jumps ($\Delta\nu_2 = 70\,\mathrm{cm}^{-1}$) translates into a ratio between the maximum (R_1) and minimum chromophore – TLS distance (R_2):

$$\frac{R_2}{R_1} = \sqrt[3]{\frac{\Delta\nu_1}{\Delta\nu_2}} = 0.25. \tag{6.1}$$

The minimum distance R_2 is taken as that between the centre of the MeLPPP-backbone and either the phenylene-ring in the 1,4-decylphenyl side chain or the CH_3-group (Fig. 6.8). From the bond length of a carbon – carbon single bond of 0.153 nm and the diameter of a phenylene-ring of 0.28 nm [214], the minimum distance R_2 can be approximated to 0.4 nm. According to eq. (6.1) the maximum distance R_1 is then about 1.6 nm. This latter value is slightly less as compared with the length of the longest side group attached to the MeLPPP-

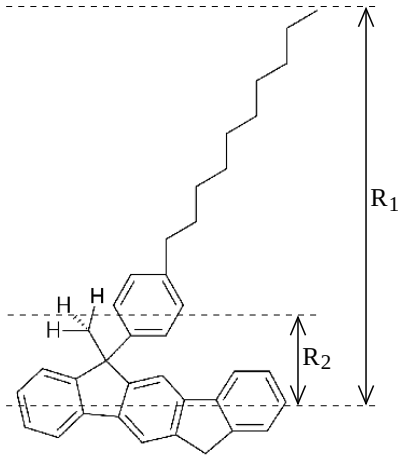

Figure 6.8: Simplified chemical structure of MeLPPP with only one methyl (CH_3) and 1,4-decylphenyl side group. The length of the 1,4-decylphenyl chain is $R_1 = 1.7\,\mathrm{nm}$ (measured from the centre of the MeLPPP-backbone). The distance between the phenylene-ring in the 1,4-decylphenyl group or the CH_3 group and the centre of the MeLPPP-backbone amounts to $R_2 = 0.4\,\mathrm{nm}$. See text for details.

backbone, which is the 1,4-decylphenyl side group with 1.7 nm length (calculated from the bond lengths given above). Taking into account that the side-chains (particularly the long 1,4-decylphenyl groups) are certainly not fully elongated in a real, disordered sample, these numbers support the assignment of TLS that was made above, i. e. the distant TLS are likely to correspond to fluctuating units in the HD/PS matrix, which is shielded by the side groups, and the nearby TLS may be attributed to fluctuations of the phenylene-rings or the methyl-groups in the side chains of MeLPPP.

Line Widths of the Electronic and Vibronic Emission Lines

A further issue that is closely related to spectral diffusion processes concerns the observed ZPL line widths of the CAS as determined from the purely electronic emission lines. Values of the order of several wavenumbers were found for the ZPL line widths of the 0-0 emission (see Fig. 6.4a). Generally, this observation allows two interpretations: (i) These emission lines are homogeneously broadened due to rapid dephasing processes. Given the excited state lifetime of MeLPPP of about 500 ps at low temperatures (see chapter 5) and the narrowest ZPL line width of $1.4\,\mathrm{cm}^{-1}$ (Fig. 6.4a), this results in a lower limit for the dephasing time of 10 ps [see eq. (2.20)]. (ii) The electronic ZPLs may be inhomogeneously broadened by unresolved spectral diffusion processes of the optical transitions that occur

on time scales faster than the acquisition time for an individual spectrum (here: 1 s).

The former process (dephasing on time scales of 10 ps) can be ruled out for two reasons. First, a homogeneous line broadening mechanism results in a Lorentzian shape of a ZPL [111]. However, the analysis of the ZPL line shapes of the 0-0 emission revealed that a significant fraction ($> 40\,\%$) deviates from a Lorentzian function (Fig. 6.3 and Table 6.1). Within the concept of the spectral diffusion kernel this finding can be interpreted to reflect ZPLs that are inhomogeneously broadened by fast, unresolved spectral diffusion processes of the optical transitions (see section 2.2.4). These prevent to record the homogeneously broadened spectral lines. Second, very recent single-molecule fluorescence excitation spectroscopy measurements on MEH-PPV embedded in PMMA at 1.8 K allowed to record electronic ZPLs with a line width of $0.1\,\mathrm{cm}^{-1}$ [56]. However, these narrow absorption lines are still one order of magnitude broader than expected from the excited state lifetime and it was suggested that this also results from residual line broadening due to spectral diffusion processes [56]. With an excited state lifetime of $T_1 = 500\,\mathrm{ps}$ the ZPL line width of $0.1\,\mathrm{cm}^{-1}$ permits to estimate a lower boundary for the pure dephasing time of $T_2^* \geq 120\,\mathrm{ps}$.

These observations allow to conclude that the ZPL line widths of the 0-0 transitions determined by single-molecule fluorescence (excitation) spectroscopy on conjugated polymers are inhomogeneously broadened due to unresolved spectral diffusion rather than homogeneously broadened by fast dephasing processes. This finding is in agreement with results obtained by low-temperature optical spectroscopy (single-molecule, hole-burning, and site-selective fluorescence spectroscopy) on organic molecules in amorphous matrices. Due to the highly disordered nature of their local environment in amorphous hosts, the lifetime-limited homogeneous line widths of the dye molecules could not be resolved (see e. g. Refs. [106, 132, 158, 200, 215]). Therefore, it seems unlikely that for conjugated polymers still narrower electronic ZPLs than $0.1\,\mathrm{cm}^{-1}$ will be observed, because single-molecule studies on these systems are typically performed in amorphous host matrices (PS, PMMA) [52, 54–56, 91, 92, 193, 216]. In addition, widely used conjugated polymers usually possess bulky and flexible side groups to ensure solubility in organic solvents. As discussed above, these side groups are likely to prevent the formation of a well-defined nano-environment for individual sites. However, this would be required to suppress spectral diffusion processes and hence to observe the lifetime-limited homogeneous line width of purely electronic transitions in conjugated polymers at low temperatures.

The line widths of the vibronic transitions presented in Fig. 6.6a are on average about $10\,\mathrm{cm}^{-1}$ broader with respect to the line widths of the electronic ZPLs (Fig. 6.4a). This becomes more clear from Fig. 6.9, where the distribution of the vibronic line widths (black bars) is shown together with the line widths of the electronic ZPLs (grey bars) of the *same*

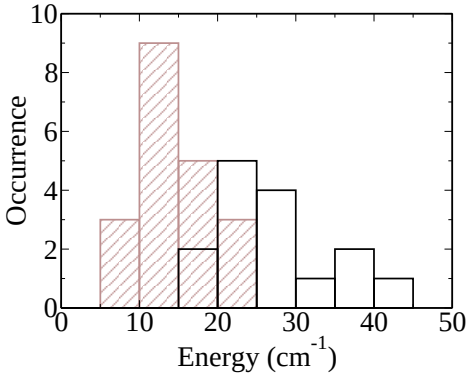

Figure 6.9: Distributions of the line widths of the vibronic class-averaged spectra (black bars) and the ZPL line widths of the 0-0 emission (grey bars) of the same chromophores. Both distributions contain the data for MeLPPP in both HD and PS.

set of chromophores. Because the electronic ZPLs are already inhomogeneously broadened due to spectral diffusion, a further line broadening mechanism must be present for the vibronic emission lines. This mechanism is attributed to homogeneous line broadening owing to fast dephasing processes and vibrational relaxation in the vibrational levels of the electronic ground state. From the mean vibronic line width of $23\,\mathrm{cm}^{-1}$ (Fig. 6.9, black bars) a vibrational dephasing time of $T_2^{\mathrm{vib}} \approx 460\,\mathrm{fs}$ in the electronic ground state can be estimated. Assuming similar pure dephasing times for the electronic ground state and the lowest electronically excited state of $T_2^* \geq 120\,\mathrm{ps}$ (see above), the lifetime of the vibrational levels in the electronic ground state amounts to $T_1^{\mathrm{vib}} \approx 230\,\mathrm{fs}$ at low temperatures. This value is in good agreement with that found for the vibrational levels in the lowest electronically excited state of conjugated polymers of about 200 fs [39,42,108]. However, this finding is in contrast to low-temperature single-molecule data on MeLPPP and MEH-PPV, where significant differences in the vibrational lifetimes between the ground and lowest electronically excited states were found [130,194].

6.4.3 Origin of the Line Splitting of Band III

In the low-energy vibronic CAS (Fig. 6.5b,d, band III) a shoulder in the low-energy wings was observed, which is offset from the dominating line by about $38\,\mathrm{cm}^{-1}$ (Fig. 6.6b and Fig. 6.10a, black bars). In principle, this shoulder may be attributed to the phonon side band of this vibronic transition, because the distributions of the mean phonon energies ω_m as determined for the 0-0 transitions have also entries at energies of about $40\,\mathrm{cm}^{-1}$ (Fig. 6.4c). "Missing" phonon energies of less than $30\,\mathrm{cm}^{-1}$ in the vibronic CAS may be ascribed to the fact that the vibronic CAS have only been evaluated for a very

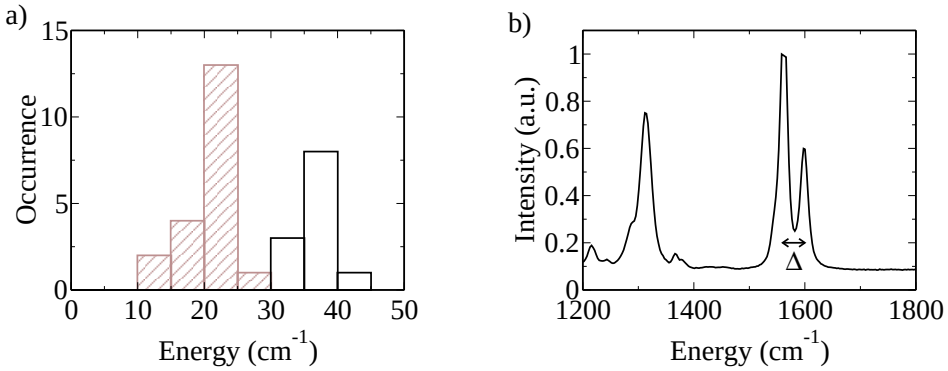

Figure 6.10: a) Distribution of the line splitting in the vibronic band III (black bars) and the histogram of the mean phonon energy determined from the purely electronic CAS (bands I) of the same chromophores (grey bars). b) Part of the room-temperature Raman spectrum of an MeLPPP-film with the strong line of the interring stretching vibration at about 1300 cm^{-1} and of the aromatic ring CC stretching mode at about 1600 cm^{-1}. The latter features a line splitting of $\Delta = 36\,\mathrm{cm}^{-1}$ due to the side groups bound to the backbone.

small subset of all investigated chromophores.

However, two observations argue against this interpretation. First, the shoulder was observed in all vibronic CAS of band III, but not in all CAS of band II (Fig. 6.5). Second, in Fig. 6.10a the distribution of the line splitting as observed for the vibronic CAS of line III (black bars) is shown together with the mean phonon energies ω_m as determined from the purely electronic CAS of the *same* chromophores (grey bars). Obviously, the line splitting observed in the vibronic CAS of band III is larger with respect to the energies of the phonon modes, that couple to the vibrational ground level of the electronic ground state for these particular chromophores. In order to explain these two findings with electron-phonon coupling, unreasonable assumptions about the phonon energies and Debye-Waller factors for the matrix phonons, that couple to the various vibronic and electronic levels, would be required. Hence, the line splitting of the vibronic CAS of the vibronic emission line III is very likely of a different origin.

The low-energy vibronic transition (III in Fig. 6.1) of the single-molecule spectra is assigned to the aromatic-ring CC stretching vibration. In the Raman spectra of MeLPPP-films at room temperature (Fig. 6.10b) the respective mode appears as a double peak at 1568 and 1604 cm^{-1} featuring a line splitting of 36 cm^{-1} due to the side chains bound to the MeLPPP-backbone [152]. The line splitting of this vibration taken from Raman data is in excellent agreement with the mean value of 38 cm^{-1} for the line splitting in the low-energy vibronic CAS (Fig. 6.10a, black bars). This provides strong evidence that the

splitting of the aromatic-ring CC stretching mode is observed on the single-molecule level, and further demonstrates that the IMAGIC programme is a powerful tool to analyse the electronic spectra from individual chromophores embedded in disordered systems despite strong spectral diffusion processes in combination with low signal-to-noise and signal-to-background ratios of the single-molecule spectra.

6.5 Conclusions

The profile of the electronic spectra of individual MeLPPP-chains could be retrieved despite the inherent structural disorder in conjugated polymers by combining low-temperature single-molecule fluorescence spectroscopy with multivariate statistical pattern recognition techniques for data analysis. A detailed analysis of the spectral profile of the purely electronic 0-0 emission lines allowed to determine for the first time the electron-phonon coupling strength of low-energy phonon modes coupled to the electronic ground state in a conjugated polymer. Debye-Waller factors of about 0.5 for MeLPPP embedded in both HD and PS were found which indicates only weak electron-phonon coupling at low temperatures irrespective of the matrix material. Additionally, these data provide strong evidence that the low-frequency phonon modes, which are coupled to the electronic transitions, stem from vibrations of the host matrix suggesting an even weaker intra-chain electron-phonon coupling in MeLPPP. Moreover, unresolved spectral diffusion processes on time scales faster than the acquisition time of individual spectra were identified to prevent the observation of the lifetime-limited homogeneous ZPL line widths of the purely electronic transitions in conjugated polymers. The vibronic emission lines of single MeLPPP-chains were also analysed. This allowed to determine the lifetime of the vibrational levels in the electronic ground state to about 230 fs. Finally, the line splitting of about $38\,\mathrm{cm}^{-1}$ observed for the aromatic-ring CC stretching mode coupled to the electronic transition could be resolved on the single-molecule level.

Appendix A

The Point Group C_{2h}

The most important properties of the point group C_{2h} are briefly reviewed in this appendix. A more detailed presentation can be found e. g. in Ref. [128].

Symmetry elements: These have already been introduced in chapter 2 and are
• identity I,
• centre of symmetry i,
• twofold symmetry axis C_2, and
• plane of symmetry σ_h perpendicular to the C_2 axis.
The C_2 axis and the σ_h plane define the z-axis and the x-y plane, respectively, of the conventional coordinate system for the C_{2h} point group. Because the highest axis is a twofold axis C_2, C_{2h} is a non-degenerate group.

Generating elements and the character table: In non-degenerate groups the character of e. g. a wave function with respect to any symmetry operation of the group may be only +1 or -1. For example a wave function ϕ belonging to the C_{2h} point group remains either unchanged (behaves symmetric) or reverses its sign (behaves antisymmetric) with respect to the symmetry operation i:

$$\begin{aligned} \phi &\xrightarrow{i} +1\ \phi \qquad \text{symmetric} \\ \phi &\xrightarrow{i} -1\ \phi \quad \text{antisymmetric.} \end{aligned}$$

Any particular combination of characters with respect to all symmetry elements is called *symmetry species* or *irreducible representation*.

Two elements of a point group are called generating elements if their product gives a third element of this group, e. g. $C_2 \times i = \sigma_h$ (see multiplication table below). Con-

ventionally, the generating elements of the C_{2h} group are i and C_2. Thus, a classification according to symmetric and antisymmetric behaviour with respect to the generating elements is possible, because all symmetry elements can be expressed as products of C_2 and/or i (see multiplication table below): symmetric and antisymmetric behaviour with respect to the element C_2 is denoted with the labels A and B, respectively, while the corresponding behaviour with respect to the element i is marked with subscripts g (gerade) and u (ungerade), respectively. Therefore, this group has in total four symmetry species, labelled A_g, A_u, B_g, and B_u.

The character table gives the combinations of characters with respect to all symmetry elements that correspond to the four symmetry species of the C_{2h} point group:

	I	C_2	i	σ_h
A_g	+1	+1	+1	+1
B_g	+1	-1	+1	-1
A_u	+1	+1	-1	-1
B_u	+1	-1	-1	+1

A_g is also called the totally symmetric species because all characters are +1, and the remaining species are referred to as non-totally symmetric ones.

Multiplication table:

	I	C_2	i	σ_h
I	I	C_2	i	σ_h
C_2	C_2	I	σ_h	i
i	i	σ_h	I	C_2
σ_h	σ_h	i	C_2	I

Abelian group: All elements of the group commute with each other, e. g. $C_2 \times i = i \times C_2$.

Multiplication of symmetry species: For the subscripts g and u these rules read

$$g \times g = g; \quad u \times u = g; \quad g \times u = u \times g = u$$

and for the labels A and B these are

$$A \times A = A; \quad B \times B = A; \quad A \times B = B \times A = B.$$

Order of the group: This is simply the number of symmetry elements, i. e. four for the C_{2h} point group.

Appendix B

Inverse Laplace Transform: The CONTIN Programme

In the analysis of most experiments the problem is faced that the measurement is indirect, in other words the desired quantity or functional relation is not directly accessible in the experiment but has to be calculated from the data by a mathematical transform. This relationship between the observed data y and the function of interest $s(\lambda)$ can be often expressed by a linear integral operator equation

$$y = \int_a^b F(\lambda)s(\lambda)d\lambda + B + \epsilon, \tag{B.1}$$

where $F(\lambda)$ denotes the kernel of the transform, B stands for a constant background signal, and ϵ is a noise component.

As an example the analysis of time-resolved data by means of eq. (B.1) is considered. In time-resolved spectroscopy the fluorescence decay y from a sample after pulsed excitation is measured as a function of time, $y = y(t)$, and the measurement yields a decay time of electronic excitations. The quantity of interest, however, is their decay (or relaxation) rate, because only decay rates of different relaxation channels can be added up to determine the total decay rate. In this case the kernel of the integral equation (B.1) is an exponential function, $F(\lambda, t) = \exp(-\lambda t)$, and eq. (B.1) reads

$$y = y(t) = \int_a^b \exp(-\lambda t)s(\lambda)d\lambda + B + \epsilon, \tag{B.2}$$

which corresponds to a Laplace transform which connects the time and frequency ("decay rate") domain. In many time-resolved experiments a mono-exponential decay, $y(t) =$

$\exp(-\lambda_0 t)$ with a single decay rate λ_0, is measured (see e. g. [95] and references therein). This function $y(t)$ can be calculated from eq. (B.2) if $s(\lambda)$ is expressed in terms of a delta function $s(\lambda) = \delta(\lambda - \lambda_0)$. Thus eq. (B.2) reduces to

$$y(t) = \int_a^b \exp(-\lambda t)\delta(\lambda - \lambda_0)d\lambda + B + \epsilon = \exp(-\lambda_0 t) + B + \epsilon, \tag{B.3}$$

which shows that a mono-exponential decay from an experiment can be described by a single decay rate λ_0.

In a situation where the fluorescence decay curves deviate from a single exponential behaviour and/or a distribution of decay rates can be expected from the model describing the relaxation dynamics (as for conjugated polymers, chapter 5), a more general solution $s(\lambda)$ is required. This solution can be obtained by inversion of eq. (B.2), i. e. by performing an inverse Laplace transform (ILT), which will generally yield a more or less complex function $s(\lambda)$. However, for an ILT of noisy data a very large – usually an infinite – number of solutions exists that all fit the data within experimental error. Because this holds even for an arbitrarily small noise component ϵ superimposed on the data, an ILT is referred to as an *ill-posed* problem [183].[1] Hence, constraints have to be imposed on the Laplace inversion to obtain stable and physically reasonable results.

The most important constraints for the ILT analysis of time-resolved data are: (i) All solutions with negative decay rates are rejected (non-negativity) because these are physically meaningless. (ii) Only decay rate distributions in a reasonable rate interval are accepted. For example the temporal window of the streak data presented in chapter 5 was 1 – 800 ps. Therefore only distributions in the reciprocal of this window between about $0.001\,\mathrm{ps}^{-1}$ and $1\,\mathrm{ps}^{-1}$ are accepted. (iii) From the remaining solutions the simplest one that fits the experimental data is chosen (usually the single-peaked rate distribution) because this particularly simple solution represents the minimum amount of information that is necessary to reproduce the data. It is therefore less likely that this solution exhibits artefacts. The former two constraints are referred to as "absolute prior knowledge" and the latter one is termed "principle of parsimony" (or "Ockham's Razor"); for further details see Ref. [183].

In order to compute the ILT and to impose the constraints (i) – (iii) the CONTIN programme by S. Provencher was employed (CONTIN: A constrained regularisation method for inverting data represented by linear algebraic or integral equations [183, 184]). This

[1] Solving eq. (B.1) for $s(\lambda)$ is an *ill-posed* problem for most kernels $F(\lambda)$ and is not restricted to exponential kernels.

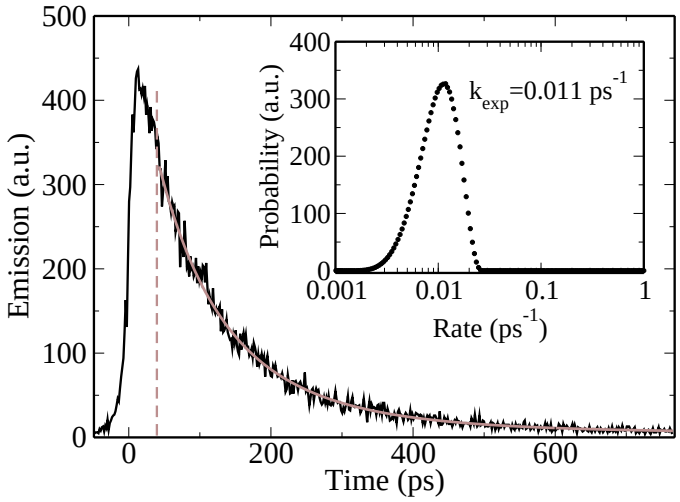

Figure B.1: Example of a fluorescence decay curve extracted from the room-temperature streak data at a detection energy of 21646 cm^{-1} (curve 1 in Fig. 5.1b). The solid grey line depicts the Laplace transform of the decay rate distribution that is shown in the inset and that was computed from the fluorescence transient by the CONTIN programme at 200 grid points between 0.001 ps^{-1} and 1 ps^{-1}. The expectation value of the distribution k_{exp} is 0.011 ps^{-1} corresponding to 91 ps.

programme numerically integrates the discrete form of eq. (B.2)

$$y(t) = \sum_{m=1}^{N_g} \exp(-\lambda_m t) s(\lambda_m) + B + \epsilon, \tag{B.4}$$

and calculates the solution $s(\lambda_m)$ at N_g grid points λ_m. In other words, the kernel of the Laplace transform now comprises N_g exponentials and the resulting solution, the distribution of decay rates $s(\lambda_m)$, is discrete as well.

Fig. B.1 depicts again the example shown in chapter 5 (see Fig. 5.1b). The ILT of the non-exponential fluorescence decay curve yielded the single-peaked distribution of decay rates with an expectation value of 0.011 ps^{-1} (corresponding to 91 ps), which is shown in the inset of Fig. B.1. Due to the fact that the Laplace inversion is an *ill-posed* problem [183] several tests were performed to verify that the obtained distribution is stable. First, only solutions in the interval between 0.001 ps^{-1} and 1 ps^{-1} were accepted, which corresponds roughly to the reciprocal of the time window of the streak data (1 – 800 ps). However, an extension of this window by more than one order magnitude did not affect the result. Second, the rate distribution was calculated at typically 200 grid points. A variation of N_g did not change the results as long as the number of grid points was larger than 100. For $N_g < 100$ often a splitting of the distributions into bi- or trimodal distributions and/or a shift of the expectation values was observed. Third, because a deconvolution of the IRF is

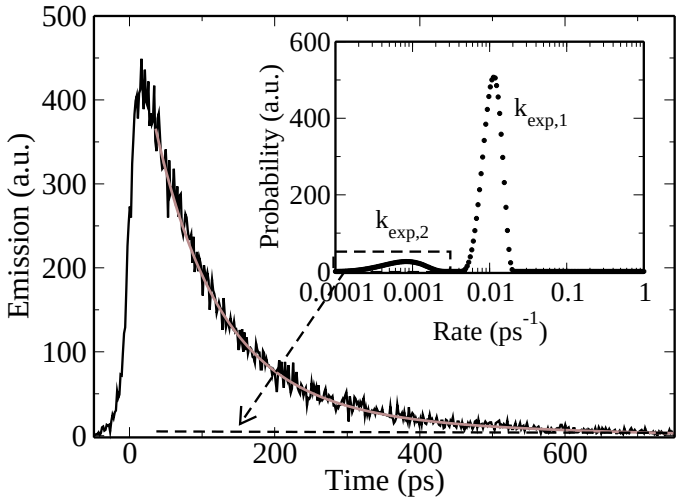

Figure B.2: Room-temperature fluorescence decay curve extracted from the streak data in Fig. 5.1 at a detection energy of 21539 cm^{-1} (solid black line) together with the Laplace transform (solid grey line) of the *entire* decay rate distribution that is presented in the inset. The decay rate distribution was calculated at 200 grid points between 0.0001 ps^{-1} and 1 ps^{-1} and exhibits a bimodal structure with expectation values of $k_{exp,1} = 0.011\,ps^{-1}$ and $k_{exp,2} = 0.0008\,ps^{-1}$ of the dominating and secondary peak, respectively. The Laplace transform of only that part of the rate distribution that is inside the dashed box yields the "decay curve" shown as a dashed black line in the main part of the figure.

not implemented in the CONTIN programme, the ILT of the decay curve in this example was restricted to data points with $t \geq 37$ ps (marked by the dashed grey line in Fig. B.1) to avoid the introduction of artefacts caused by the IRF. It was checked that the precise length of the decaying part of the decay curve did not influence the rate distribution as long as the first few data points after the peak are excluded. Finally, a Laplace transform of the decay rate distribution back into the time domain was performed, which results in the solid grey line in Fig. B.1 fitting the experimental data excellently.

In the tests described above the solutions of the ILT turned out to be stable. Therefore it can be concluded that the decay rate distributions calculated by the ILT yield reasonable results. The standard deviation of the rate distribution should be considered only as an approximate measure for the width, because the standard deviation depends on details of the experimental decay curve, in particular on its signal-to-noise and signal-to-background ratio.

In contrast to the typical single-peaked decay rate distributions (see e. g. in the inset of Fig. B.1), that were computed by the CONTIN programme from nearly all fluorescence decay curves, the ILT of two room-temperature decay curves yielded decay rate rate distri-

butions with more than one peak. As an example a bimodal decay rate distribution is shown in the inset of Fig. B.2, that was calculated by the CONTIN programme from the decay curve extracted from the 296 K streak image at a detection energy of 21539 cm^{-1} (Fig. B.2, solid black line). The Laplace transform of this bimodal decay rate distribution is in very good agreement with the experimental decay curve (Fig. B.2, solid grey line). The expectation value of the dominating peak of the distribution of decay rates is of the order of 0.01 ps^{-1}, while the second peak has an amplitude that is more than one order of magnitude smaller and an expectation value of less than 0.001 ps^{-1}. This latter rate corresponds to an excited state lifetime of more than 1 ns, which is clearly beyond the temporal detection window of 800 ps of the streak data. The Laplace transform of only the secondary peak of the decay rate distribution (enclosed in the dashed box in the inset of Fig. B.2) gives the dashed black line in Fig. B.2, which does not contribute significantly to the fluorescence decay at short times $\leq$ 600 ps. Therefore, the appearance of this weak second peak can be ascribed to the low background signal superimposed on the fluorescence decays, which shows a slight variation across the streak image. This background is interpreted by the CONTIN programme as a very slow decay component ($>$ 1 ns) with a small amplitude. Consequently, these secondary peaks have been neglected in the discussion of the data in chapter 5.

Summary

Conjugated polymers attracted considerable attention in the past years owing to their high potential for applications in (novel) optoelectronic devices, such as polymer light-emitting diodes, organic photovoltaic cells, and flexible displays. However, many of the intrinsic key parameters that determine the photophysical properties of π-conjugated polymers, are not fully understood. Therefore, the nature of the lowest electronic singlet states in a rigid, rod-like π-conjugated polymer, methyl-substituted ladder-type poly(*para*-phenylene) (MeLPPP), was investigated in this thesis by different spectroscopic techniques.

The first set of experiments reported in this thesis is a comparative study of one-photon absorption and two-photon fluorescence excitation spectroscopy on bulk MeLPPP-films at room temperature. The results revealed that for MeLPPP the parity selection rules for optical transitions are well fulfilled. This indicates a high degree of symmetry, particularly the presence of a centre of inversion, in the electronic wave functions in the lowest singlet states. This is a consequence of the rigid, rod-like backbone of MeLPPP that supports a highly ordered structure, at least on typical length scales of the delocalisation of the electronic wave functions in the various electronic states. The bulky and flexible side groups bound to the backbone do not significantly lower the symmetry. Additionally, the symmetries and energies of the dominating vibrational modes, the inter-ring stretching and aromatic ring CC stretching vibrations, coupled to the electronic ground state and the two lowest electronically excited singlet states were analysed in detail. By group theoretical considerations it was found that only totally symmetric a_g vibrations can be observed in 1P- and 2P-spectra of MeLPPP (as well as in its emission spectra). Hence, a discrimination of vibrational modes by symmetry selection rules via 1P- and 2P-spectroscopy is not possible. This led to the finding that the energies of the vibrational modes are on average about $220\,\mathrm{cm}^{-1}$ lower in the second excited 2^1A_g singlet level as compared to the lowest excited singlet (1^1B_u) state and the electronic ground state (1^1A_g). This large shift of the vibrational energies was attributed to significant changes of the equilibrium geometry of the MeLPPP backbone in the 2^1A_g level with respect to the 1^1B_u and the 1^1A_g states.

In the second part of this work, the results of picosecond time-resolved spectroscopy with high spectral resolution were described, which was performed on MeLPPP-films both at 1.5 K and at 296 K by employing a streak camera technique. These experiments were performed to shed light on the excitation energy relaxation processes within the density of electronically excited states (DOS) as well as on the decay kinetics of electronic excitations into the electronic ground state. The decaying part of the fluorescence transients, that were extracted from the high-resolution streak images, were found to be mainly non-exponential. These curves were analysed by means of an inverse Laplace transform which demonstrated that a single-peaked distribution of decay rates, rather than a single time constant, consistently describes the relaxation dynamics both at low and at room temperatures. This reflects the large heterogeneity of conjugated polymer samples, which leads to a distribution of inter-site distances. This results in a broad distribution of intra-DOS excitation energy transfer rates between chromophores due to the distance dependent electronic coupling. Additionally, a distribution of oscillator strengths, caused by a distribution of conjugation lengths of the chromophores, contributes to the decay rate distributions. For both the 1.5 K and 296 K streak data the expectation values of the decay rate distributions were computed as a function of detection energy and the spectral moments of the transient emission spectra were calculated as a function of time. At cryogenic temperatures this allowed to resolve the time- and energy-dependent population of sites located in the low-energy tail of the DOS from energetically higher lying sites in great detail. In particular, the rising components of the fluorescence transients in the low-energy wing of the spectrum and their dependence on the detection energy were revealed for the first time. From these data the nearest-neighbour transfer time of electronic excitations was determined to be 30 – 40 ps at 1.5 K. These findings at low temperatures are in contrast to those at room temperature. At 296 K a time- and energy-dependence of the relaxation processes was not observed which is attributed to (i) a competition between thermally assisted uphill migration and relaxation to lower lying sites within the lifetime of the electronically excited state and (ii) to the fact that the width of the DOS in MeLPPP is primarily given by the homogeneous line width. Finally, the data permitted to determine the radiative lifetime (i. e. the expectation value of a lifetime distribution) of the lowest excited electronic state which is about 800 ps both at 1.5 K and at 296 K.

Finally, single-molecule fluorescence spectroscopy experiments were performed at 1.5 K on individual MeLPPP-chains embedded either in *n*-hexadecane (HD) or in polystyrene (PS). The intrinsic structural disorder in conjugated polymer chains as well as the disordered nature of the surrounding matrix materials leads to strong spectral diffusion processes of the optical transitions. Therefore, the profile of the electronic spectra of individ-

ual MeLPPP-chains could only be retrieved by applying a multivariate statistical pattern recognition technique for analysis of the single-molecule spectra. The purely electronic (0-0) emission lines of individual chromophores in both HD and PS featured a recurrent motif of a sharp line and a shoulder in their low-energy wings, that were assigned to the zero phonon line and the phonon side band. A quantitative analysis of this spectral shape permitted to determine the electron-phonon coupling strength and the energies of the low-energy vibrational modes, that are coupled to the electronic ground state. The Debye-Waller factors are distributed around 0.5 for MeLPPP in both HD and PS indicative of only weak electron-phonon coupling at 1.5 K independent of the matrix material. The analysis of the phonon energies provided strong evidence that the low-energy modes, coupled to the electronic transitions, are vibrations of the host matrix. This suggests a still weaker electron-phonon coupling to intra-molecular modes of MeLPPP. In both matrix materials (HD/PS) strong spectral diffusion processes of the optical transitions of individual chromophores were observed in the single-molecule spectra. These processes were identified to result from fluctuating units in the surrounding host (HD/PS) and from librations/torsions of the phenylene-ring and the methyl-group in the side chains of MeLPPP. Furthermore, unresolved spectral diffusion processes, that occur on time scales faster than the acquisition time of an individual single-molecule spectrum, were found to give rise to inhomogeneous line broadening of the zero phonon lines (ZPL) of the 0-0 emissions. These processes prevent to resolve the lifetime-limited homogeneous line widths of the ZPLs in MeLPPP at 1.5 K. The analysis of the vibronic emission lines of single MeLPPP-chains allowed to determine the vibrational relaxation time in the electronic ground state to about 230 fs. Additionally, the statistical approach for data analysis enabled to resolve (on the single-molecule level) the line splitting of the aromatic-ring CC stretching mode of about $38\,\mathrm{cm}^{-1}$ due to the sidegroups bound to the MeLPPP backbone.

In conclusion, it has been shown in this work that a combination of spectroscopic techniques provides detailed insight into the photophysical parameters of the lowest electronic singlet states of a ladder-type conjugated polymer. Two-photon spectroscopy allowed to investigate higher excited singlet states, that are not accessible by conventional (one-photon) spectroscopy. By time-resolved spectroscopy with high spectral resolution a complete and conclusive picture of relaxation processes within the DOS as well as of the decay kinetics into the electronic ground state was derived. Single-molecule spectroscopy allowed to determine the entire distributions of parameters that is not possible with conventional ensemble spectroscopy, in particular for the first time the electron-phonon coupling strength to low-energy vibrations could be determined for a conjugated polymer.

Deutsche Zusammenfassung

In den letzten Jahren wurden π-konjugierte Polymere mit großem Interesse untersucht, da diese Materialien ein hohes Potential für Anwendungen in (neuen) optoelektronischen Bauelementen besitzen, wie zum Beispiel Polymer-Leuchtdioden, organische Solarzellen und flexible Anzeigen. Jedoch sind viele der intrinsischen Parameter, die die photophysikalischen Eigenschaften konjugierter Polymere bestimmen, noch nicht gut verstanden. Daher wurde in dieser Arbeit die Natur der niedrigsten Singulett-Zustände in einem starren, stabförmigen π-konjugierten Polymer, Methyl-substituiertem Leiter-Poly(*para*-Phenylen), MeLPPP, mit Hilfe verschiedener spektroskopischer Techniken untersucht.

Der erste Teil der Ergebnisse, die in dieser Arbeit präsentiert wurden, ist eine vergleichende Studie zwischen (Ein-Photon, 1P) Absorptions- und Zwei-Photonen (2P) Fluoreszenz-Anregungsspektroskopie an dünnen MeLPPP-Filmen bei Raumtemperatur. Die Ergebnisse zeigten, dass die Symmetrieauswahlregeln für optische Übergänge in MeLPPP sehr gut erfüllt sind, was auf eine hohe Symmetrie der elektronischen Wellenfunktionen in den niedrigsten elektronischen Singulett-Zuständen hindeutet, insbesondere auf die Existenz eines Inversionszentrums. Dies ist eine Konsequenz des starren MeLPPP-Gerüstes, das eine sehr geordnete Polymergeometrie auf typischen Längenskalen der Delokalisation der elektronischen Wellenfunktionen in den untersuchten Singulett-Zuständen unterstützt. Die langen und flexiblen Seitengruppen von MeLPPP verringern diese Symmetrien nicht signifikant. Außerdem wurden die Symmetrien und Energien der dominierenden Vibrationsmoden (die inter-Ring Streckschwingung und die CC-Streckschwingung der aromatischen Ringe), die an den elektronischen Grundzustand und die beiden niedrigsten elektronisch angeregten Singulett-Zustände ankoppeln, im Detail untersucht. Durch gruppentheoretische Überlegungen wurde gefunden, dass nur totalsymmetrische a_g Schwingungen in den 1P- und 2P-Spektren von MeLPPP beobachtet werden können. Dies führte zum Schluss, dass die Energien der Schwingungsmoden im zweiten angeregten Singulett-Zustand (2^1A_g) um ca. $220\,\mathrm{cm}^{-1}$ niedriger sind als im niedrigsten angeregten Singulett- (1^1B_u) und im Grundzustand (1^1A_g). Diese starke Verschiebung der Schwingungsenergien konnte auf

eine signifikante Änderung der Gleichgewichtsgeometrie des MeLPPP-Rückgrats im 2^1A_g Zustand gegenüber der in den 1^1B_u und 1^1A_g Zuständen zurückgeführt werden.

Im zweiten Teil dieser Arbeit wurde an MeLPPP-Filmen mit Hilfe einer Streak-Kamera Technik zeitaufgelöste Spektroskopie auf der Pikosekunden-Zeitskala mit hoher spektraler Auflösung durchgeführt. Diese Experimente erfolgten sowohl bei Raumtemperatur als auch bei 1.5 K, um Informationen über die Relaxationsprozesse elektronischer Anregungen innerhalb der Verteilung elektronisch angeregter Zustände (*density of electronically excited states*, DOS) als auch über die Zerfallskinetik elektronischer Anregungen in den Grundzustand zu erhalten. Der abklingende Teil der Fluorezenzzerfallskurven, die aus den Streak-Kamera Daten berechnet wurden, zeigte in den meisten Fällen ein nicht-exponentielles Verhalten. Diese Kurven wurden mittels einer inversen Laplace-Transformation analysiert und es zeigte sich, dass eine Verteilung von Zerfallsraten des niedrigsten angeregten Zustandes mit nur einem Maximum sowohl die Raum- als auch die Tieftemperaturdaten besser beschreibt als eine einzige Zerfallsrate. Der Grund für diese Beobachtung ist die starke Heterogenität von konjugierten Polymeren, die zu einer Verteilung von Abständen zwischen den Chromophoren auf und zwischen den Ketten führt. Daraus folgt direkt, dass eine Verteilung von Transferraten zwischen den Chromophoren existiert, da der Energietransfer durch eine abstandsabhängige elektronische Kopplung vermittelt wird. Außerdem trägt auch eine Verteilung der Oszillatorenstärke aufgrund einer Verteilung von Konjugationslängen zu einer Verteilung der Zerfallsraten des niedrigsten angeregten Zustandes bei. Für die Tieftemperatur- und die Raumtemperaturdaten wurden die Erwartungswerte der Verteilung der Zerfallsraten als Funktion der Detektionsenergie als auch die spektralen Momente der transienten Emissionsspektren als Funktion der Zeit berechnet. Bei 1.5 K erlaubte dies, die zeit- und energieabhängige Besetzung von energetisch niedriger liegenden Zuständen innerhalb der DOS, ausgehend von energetisch höher liegenden, detailliert aufzulösen. Auch eine ansteigende Komponente in den Fluoreszenzzerfallskurven im niederenergetischen Teil des Spektrums und deren Energieabhängigkeit konnte erstmals gemessen werden. Aus diesen Daten wurde weiterhin die Nächste-Nachbar-Transferzeit zu 30 – 40 ps bei 1.5 K bestimmt. Im Gegensatz zu den 1.5 K Daten wurde in den Raumtemperaturdaten keine zeit- und energieabhängige Relaxation von Anregungen beobachtet, was zurückgeführt wurde auf (i) einen Wettbewerb zwischen thermisch aktivierten Transfer zu höher liegenden Zuständen und Relaxation zu niedriger liegenden Zuständen innerhalb der Lebensdauer der angeregten Zustände, und (ii) auf die Tatsache, dass die Breite der DOS von MeLPPP hauptsächlich durch die homogene Linienbreite bestimmt ist. Schließlich konnte aus den zeitaufgelösten Daten auch die strahlende Lebensdauer (also der Erwartungswert einer Lebensdauerverteilung) des niedrigsten angeregten Zustands zu

ca. 800 ps (bei 1.5 K und Raumtemperatur) bestimmt werden.

Im letzten Teil wurde Einzelmolekülfluoreszenzspektroskopie an MeLPPP bei 1.5 K durchgeführt. Dazu wurden einzelne MeLPPP-Ketten entweder in n-Hexadekan (HD) oder Polystyrol (PS) eingebettet. Aufgrund der intrinsischen strukturellen Unordnung in konjugierten Polymeren und in den umgebenden Matrixmaterialien wurde starke spektrale Diffusion der optischen Übergänge beobachtet. Daher konnte das Profil der optischen Spektren einzelner MeLPPP-Ketten nur bestimmt werden, indem ein multivariater statischer Mustererkennungsalgorithmus zur Datenanalyse angewandt wurde. Die rein elektronischen (0-0) Emissionslinien einzelner Chromophore in beiden Matrizen (HD und PS) zeigten ein wiederkehrendes Profil, das aus einer schmalen Linie und einer Schulter in deren niederenergetischer Flanke besteht, und das der Nullphononenlinie und der Phononenseitenbande zugeordnet wurde. Die quantitative Analyse dieser Linienform erlaubte, die Stärke der Elektron-Phonon-Kopplung und die Energien der niederenergetischen Phononenmoden zu bestimmen, die an den elektronischen Grundzustand koppeln. Die Debye-Waller-Faktoren für MeLPPP in HD als auch PS sind um den Wert 0.5 verteilt, was auf eine schwache Elektron-Phonon-Kopplung bei 1.5 K hindeutet, die unabhängig von der Matrix ist. Die Auswertung der Phononenenergien ergab, dass die Phononen, die an den Grundzustand koppeln, niederenergetische Moden der Matrix sind. Dies weist auf eine noch schwächere Elektron-Phonon-Kopplung von intra-molekulare Schwingungen des MeLPPP-Gerüstes hin. Für beide Matrixmaterialien (HD/PS) wurde starke spektrale Diffusion der optischen Übergänge in den Emissionsspektren einzelner Chromophore beobachtet. Es konnte gezeigt werden, dass diese Prozesse vermutlich von fluktuierenden Einheiten in der Wirtsmatrix und von Librations-/Torsionsmoden der Phenylenringe oder der Methyl-Gruppen in den MeLPPP-Seitenketten verursacht werden. Spektrale Diffusion auf einer Zeitskala, die schneller ist als die Integrationszeit für ein Einzelmolekülspektrum und daher nicht aufgelöst werden kann, führt zu einer inhomogenen Verbreiterung der Nullphononenlinien der rein elektronischen Emissionslinien. Dies verhindert, dass bei 1.5 K die Lebensdauer-begrenzte homogene Breite dieser Linien aufgelöst werden kann. Eine Analyse der Linienbreiten der vibronischen Übergänge einzelner Chromophore erlaubte, die Vibrationsrelaxationszeit zu 230 fs für den elektronischen Grundzustand von MeLPPP zu bestimmen. Außerdem konnte durch die statistische Auswertemethode erstmals die Aufspaltung der CC Streckschwingung der aromatischen Ringe aufgrund der Seitenketten auf Einzelmolekülebene beobachtet werden.

Zusammenfassend konnte in dieser Arbeit gezeigt werden, dass eine Kombination spektroskopischer Techniken detaillierte Einblicke in die photophysikalischen Parameter der niedrigsten Singulett-Zustände in einem Leiter-Typ konjugierten Polymer ermöglicht. Zwei-

Photonen Spektroskopie erlaubte, höhere angeregte Singulett-Zustände zu untersuchen, die durch konventionelle (Ein-Photonen) Spektroskopie nicht zugänglich sind. Durch zeitaufgelöste Spektroskopie mit hoher spektraler Auflösung konnte ein komplettes und schlüssiges Bild der Relaxationsprozesse elektronischer Anregungen innerhalb der DOS als auch deren Zerfallskinetik in den Grundzustand abgeleitet werden. Mit Hilfe der Einzelmolekülspektroskopie können die vollständigen Verteilungen von Parametern gemessen werden, was mit Spektroskopie am Ensemble nicht möglich ist, insbesondere konnte damit erstmals die Elektron-Phonon-Kopplungsstärke niederenergetischer Vibrationsmoden in konjugierten Polymeren bestimmt werden.

Bibliography

[1] C. K. Chiang, C. R. Fincher, Y. W. Park, A. J. Heeger, H. Shirakawa, E. J. Louis, S. C. Gau, and A. G. MacDiarmid. *Phys. Rev. Lett.* **39** (1977) 1098 – 1101.

[2] C. W. Tang and S. A. VanSlyke. *Appl. Phys. Lett.* **51** (1987) 913 – 915.

[3] J. H. Burroughes, D. D. C. Bradley, A. R. Brown, R. N. Marks, K. Mackay, R. H. Friend, P. L. Burns, and A. B. Holmes. *Nature* **347** (1990) 539 – 541.

[4] R. H. Friend, L. W. Gymer, A. B. Holmes, J. H. Burroughes, R. N. Marks, C. Taliani, D. D. C. Bradley, D. A. Dos Santos, J. L. Bredas, M. Logdlund, and W. R. Salaneck. *Nature* **397** (1999) 121 – 128.

[5] U. Scherf, S. Riechel, U. Lemmer, and R. F. Mahrt. *Curr. Opin. Solid St. M.* **5** (2001) 143 – 154.

[6] F. Hide, M. A. Diaz-Garcia, B. J. Schwartz, and A. J. Heeger. *Acc. Chem. Res.* **30** (1997) 430 – 436.

[7] U. Scherf. *J. Mater. Chem.* **9** (1999) 1853 – 1864.

[8] J. Campbell Scott and L. D. Bozano. *Adv. Mater.* **19** (2007) 1452 – 1463.

[9] Q.-D. Ling, Y. Song, S.-L. Lim, E. Yeow-Hwee Teo, Y.-P. Tan, C. Zhu, D. S. Hhung Chan, D.-L. Kwong, E.-T. Kang, and K.-G. Neoh. *Angew. Chem.* **118** (2006) 3013 – 3017.

[10] J. W. Hong, W. L. Hemme, G. E. Keller, M. T. Rinke, and G. C. Bazan. *Adv. Mater.* **18** (2006) 878 – 882.

[11] G. Hadziioannou and P. F. van Putten. *Semiconducting Polymers.* Wiley-VCH, Weinheim, 2000.

[12] www.sony.net/SonyInfo/News/Press/200710/07-1001E/index.html.

[13] F. Laquai, A. K. Mishra, M. R. Ribas, A. Petrozza, J. Jacob, L. Akcelrud, K. Müllen, R. H. Friend, and G. Wegner. *Adv. Funct. Mater.* **17** (2007) 3231 – 3240.

[14] M. R. Andersson, O. Thomas, W. Mammo, M. Svensson, M. Theander, and O. Inganäs. *J. Mater. Chem.* **9** (1999) 1933 – 1940.

[15] A. Kraft, A. C. Grimsdale, and A. B. Holmes. *Angew. Chem. Int. Ed.* **37** (1998) 402 – 428.

[16] S. R. Forrest. *Nature* **428** (2004) 911 – 918.

[17] B. Gerl. *Spektrum der Wissenschaft* **Oktober** (2004) 64 – 67.

[18] W. Clemens and W. Fix. *Physik Journal* **Februar** (2003) 31 – 36.

[19] F. J. M. Hoeben, L. M. Herz, C. Daniel, P. Jonkheijm, A. P. H. J. Schenning, C. Silva, S. C. J. Meskers, D. Beljonne, R. T. Phillips, R. H. Friend, and E. W. Meijer. *Angew. Chem. Int. Ed.* **43** (2004) 1976 – 1979.

[20] D. Beljonne, E. Hennebicq, C. Daniel, L. M. Herz, C. Silva, G. D. Scholes, F. J. M. Hoeben, P. Jonkheijm, A. P. H. J. Schenning, S. C. J. Meskers, R. T. Phillips, R. H. Friend, and E. W. Meijer. *J. Phys. Chem. B* **109** (2005) 10594 – 10604.

[21] M. Pope and C. E. Swenberg. *Electronic Processes in Organic Crystals and Polymers*. Oxford University Press, Oxford, New York, 1999.

[22] J. L. Bredas, D. Beljonne, V. Coropceanu, and J. Cornil. *Chem. Rev.* **104** (2004) 4971 – 5003.

[23] W. Barford. *Electronic and Optical Properties of Conjugated Polymers*. Number 129 in International Series of Monographs on Physics. Oxford University Press, Oxford, Oxford, New York, 2005.

[24] V. May and O. Kühn. *Charge and Energy Transfer Dynamics in Molecular Systems*. WILEY-VCH, Berlin, 2000.

[25] N. S. Sariciftci. *Primary Photoexcitations in Conjugated Polymers: Molecular Exciton versus Semiconductor Band Model*. World Scientific, Singapore, 1997.

[26] E. M. Conwell. *in: Organic Electronic Materials*, chapter 4, 127 – 180. Springer, Berlin, Heidelberg, New York, 2001.

[27] M. Springborg, K. Schmidt, H. Meider, and L. De Maria. *in: Organic Electronic Materials*, chapter 2, 39 – 88. Springer, Berlin, Heidelberg, New York, 2001.

[28] T. Blythe and D. Bloor. *Electrical Properties of Polymers*. Cambridge University Press, Cambridge, New York, 2005.

[29] H. Bässler and B. Schweitzer. *Acc. Chem. Res.* **32** (1999) 173 – 182.

[30] B. J. Schwartz. *Annu. Rev. Phys. Chem.* **54** (2003) 141 – 172.

[31] I. G. Scheblykin, A. Yartsev, T. Pullerits, V. Gulbinas, and V. Sundström. *J. Phys. Chem. B* **111** (2007) 6303 – 6321.

[32] R. Schroeder and B. Ullrich. *Opt. Lett.* **27** (2002) 1285 – 1287.

[33] A. Hohenau, C. Cagran, G. Kranzelbinder, U. Scherf, and G. Leising. *Adv. Mater.* **13** (2001) 1303 – 1307.

[34] M. G. Harrison, G. Urbasch, R. F. Mahrt, H. Giessen, H. Bässler, and U. Scherf. *Chem. Phys. Lett.* **313** (1999) 755 – 762.

[35] R. Schroeder, W. Graupner, U. Scherf, and B. Ullrich. *J. Chem. Phys.* **116** (2002) 3449 – 3454.

[36] C. J. Baker, O. M. Gelsen, and D. D. C. Bradley. *Chem. Phys. Lett.* **201** (1993) 127 – 131.

[37] N. Periasamy, R. Danieli, G. Ruani, R. Zamboni, and C. Taliani. *Phys. Rev. Lett.* **68** (1992) 919 – 922.

[38] U. Lemmer, R. Fischer, J. Feldmann, R. F. Mahrt, J. Yang, A. Greiner, H. Bässler, E. O. Göbel, H. Heesel, and H. Kurz. *Chem. Phys. Lett.* **203** (1993) 28 – 32.

[39] R. Kersting, U. Lemmer, R. F. Mahrt, K. Leo, H. Kurz, H. Bässler, and E. O. Göbel. *Phys. Rev. Lett.* **70** (1993) 3820 – 3823.

[40] S. C. J. Meskers, J. Hübner, M. Oestreich, and H. Bässler. *J. Phys. Chem. B* **105** (2001) 9139 – 9149.

[41] M. Scheidler, U. Lemmer, R. Kersting, S. Karg, W. Riess, B. Cleve, R. F. Mahrt, H. Kurz, H. Bässler, E. O. Göbel, and P. Thomas. *Phys. Rev. B* **54** (1996) 5536 – 5544.

[42] R. Kersting, B. Mollay, M. Rusch, J. Wenisch, G. Leising, and H. F. Kauffmann. *J. Chem. Phys.* **106** (1997) 2850 – 2864.

[43] C. Madigan and V. Bulovic. *Phys. Rev. Lett.* **96** (2006) 046404.

[44] G. R. Hayes, I. D. W. Samuel, and R. T. Phillips. *Phys. Rev. B* **56** (1997) 3838 – 3843.

[45] M. Yan, L. J. Rothberg, F. Papadimitrakopoulos, M. E. Galvin, and T. M. Miller. *Phys. Rev. Lett.* **73** (1994) 744 – 747.

[46] S. Westenhoff, W. J. D. Beenken, R. H. Friend, N. C. Greenham, A. Yartsev, and V. Sundström. *Phys. Rev. Lett.* **97** (2006) 166804.

[47] A. L. T. Khan, P. Sreearunothai, L. M. Herz, M. J. Banach, and A. Köhler. *Phys. Rev. B* **69** (2004) 085201.

[48] V. Gulbinas, I. Mineviciute, D. Hertel, R. Wellander, A. Yartsev, and V. Sundström. *J. Chem. Phys.* **127** (2007) 144907.

[49] D. Hu, J. Yu, K. Wong, B. Bagchi, P. J. Rossky, and P. F. Barbara. *Nature* **405** (2000) 1030 – 1033.

[50] W. E. Moerner and L. Kador. *Phys. Rev. Lett.* **62** (1989) 2535 – 2538.

[51] M. Orrit and J. Bernard. *Phys. Rev. Lett.* **65** (1990) 2716 – 2719.

[52] F. Schindler, J. M. Lupton, J. Feldmann, and U. Scherf. *Proc. Natl. Acad. Sci. U.S.A.* **101** (2004) 14695 – 14700.

[53] D. A. Vanden Bout, W.-T. Yip, D. Hu, D.-K. Fu, T. M. Swager, and P. F. Barbara. *Science* **277** (1997) 1074 – 1077.

[54] J. G. Müller, U. Lemmer, G. Raschke, M. Anni, U. Scherf, J. M. Lupton, and J. Feldmann. *Phys. Rev. Lett.* **91** (2003) 267403.

[55] T. Pullerits, O. Mirzov, and I. G. Scheblykin. *J. Phys. Chem. B* **109** (2005) 19099 – 19107.

[56] F. A. Feist, G. Tommaseo, and T. Basché. *Phys. Rev. Lett.* **98** (2007) 208301.

[57] T. Huser, M. Yan, and L. J. Rothberg. *Proc. Natl. Acad. Sci. U.S.A.* **97** (2000) 11187 – 11191.

[58] J. D. White, J. H. Hsu, W. S. Fann, S.-C. Yang, G. Y. Pern, and S. A. Chen. *Chem. Phys. Lett.* **338** (2001) 263 – 268.

[59] F. Dubin, R. Melet, T. Barisien, R. Grousson, L. Legrand, M. Schott, and V. Voliotis. *Nature Phys.* **2** (2006) 32 – 35.

[60] C. W. Hollars, S. M. Lane, and T. Huser. *Chem. Phys. Lett.* **370** (2003) 393 – 398.

[61] P. Kumar, T.-H. Lee, A. Mehta, B. G. Sumpter, R. M. Dickson, and M. D. Barnes. *J. Am. Chem. Soc.* **126** (2004) 3376 – 3377.

[62] J. Stampfl, S. Tasch, G. Leising, and U. Scherf. *Synth. Met.* **71** (1995) 2125 – 2128.

[63] H. D. Burrows, J. Seixas de Melo, C. Serpa, L. G. Arnaut, A. P. Monkman, I. Hamblett, and S. Navaratnam. *J. Chem. Phys.* **115** (2001) 9601 – 9606.

[64] U. Scherf and K. Müllen. *Adv. Polym. Sci.* **123** (1995) 1 – 40.

[65] P. W. Atkins. *Physikalische Chemie*. Wiley-VCH, Weinheim, 2001.

[66] O. A. Neumüller. *Römpps Chemie Lexikon*. Franckh'sche Verlagshandlung, Stuttgart, 1983.

[67] E. Hückel. *Z. Phys.* **70** (1931) 204 – 286.

[68] E. Hückel. *Z. Phys.* **72** (1931) 310 – 337.

[69] E. Hückel. *Z. Phys.* **76** (1932) 628 – 648.

[70] R. Pariser and R. G. Parr. *J. Chem. Phys.* **21** (1953) 466 – 471.

[71] R. Pariser and R. G. Parr. *J. Chem. Phys.* **21** (1953) 767 – 776.

[72] J. A. Pople. *Trans. Faraday Soc.* **49** (1953) 1375 – 1385.

[73] W. P. Su, J. R. Schrieffer, and A. J. Heeger. *Phys. Rev. Lett.* **42** (1979) 1698 – 1701.

[74] A. J. Heeger, S. Kivelson, J. R. Schrieffer, and W. P. Su. *Rev. Mod. Phys.* **60** (1988) 781 – 850.

[75] J. Bredas, J. Cornil, D. Beljonne, D. A. dos Santos, and Z. Shuai. *Acc. Chem. Res.* **32** (1999) 267 – 276.

[76] S. Tretiak, A. Saxena, R. L. Martin, and A. R. Bishop. *Phys. Rev. Lett.* **89** (2002) 097402.

[77] W. J. D. Beenken and T. Pullerits. *J. Chem. Phys.* **120** (2004) 2490 – 2495.

[78] S. Mukamel, S. Tretiak, T. Wagersreiter, and V. Chernyak. *Science* **277** (1997) 781 – 787.

[79] W. J. D. Beenken and T. Pullerits. *J. Phys. Chem. B* **108** (2004) 6164 – 6169.

[80] E. Hennebicq, C. Deleener, J. Bredas, G. D. Scholes, and D. Beljonne. *J. Chem. Phys.* **125** (2006) 054901.

[81] S. Karabunarliev, E. R. Bittner, and M. Baumgarten. *J. Chem. Phys.* **114** (2001) 5863 – 5870.

[82] D. Beljonne, G. Pourtois, C. Silva, E. Hennebicq, L. M. Herz, R. H. Friend, G. D. Scholes, S. Setayesh, K. Müllen, and J. L. Bredas. *Proc. Natl. Acad. Sci. U.S.A.* **99** (2002) 10982 – 10987.

[83] J. Rissler. *Chem. Phys. Lett.* **395** (2004) 92 – 96.

[84] H. Bässler. *phys. status solidi b* **175** (1993) 15.

[85] H. Bässler. *Primary photoexcitations in conjugated polymers*, chapter 3, 51 – 98. World Scientific, Singapore, 1997.

[86] O. Mirzov and I. G. Scheblykin. *Phys. Chem. Chem. Phys.* **8** (2006) 5569 – 5576.

[87] T. W. Hagler, K. Pakbaz, K. F. Voss, and A. J. Heeger. *Phys. Rev. B* **44** (1991) 8652 – 8666.

[88] J. Gierschner, H.-G. Mack, H.-J. Egelhaaf, S. Schweizer, B. Doser, and D. Oelkrug. *Synth. Met.* **138** (2003) 311 – 315.

[89] J. Yu, D. Hu, and P. F. Barbara. *Science* **289** (2000) 1327 – 1330.

[90] P. F. Barbara, A. J. Gesquiere, S.-J. Park, and Y. J. Lee. *Acc. Chem. Res.* **38** (2005) 602 – 610.

[91] E. Da Como, K. Becker, J. Feldmann, and J. M. Lupton. *Nano Lett.* **7** (2007) 2993 – 2998.

[92] O. Mirzov, T. Pullerits, F. Cichos, C. von Borczyskowski, and I. G. Scheblykin. *Chem. Phys. Lett.* **408** (2005) 317 – 321.

[93] T.-S. Lim, J.-C. Hsiang, J. D. White, J. H. Hsu, Y. L. Fan, K. F. Lin, and W. S. Fann. *Phys. Rev. B* **75** (2007) 165204.

[94] C. F. Wang, J. D. White, T. L. Lim, J. H. Hsu, S. C. Yang, W. S. Fann, K. Y. Peng, and S. A. Chen. *Phys. Rev. B* **67** (2003) 035202–1 – 035202–8.

[95] J. R. Lakowicz. *Principles of fluorescence spectroscopy.* Springer, New York, 2006.

[96] B. Valeur. *Molecular Fluorescence.* Wiley-VCH, Weinheim, New York, 2002.

[97] J. B. Birks. *Organic Molecular Photophysics, Vol. 1.* John Wiley & Sons, London, 1973.

[98] B. Tian and G. Zerbi. *Synth. Met.* **41 − 43** (1991) 255 – 259.

[99] C. Gadermaier, G. Cerullo, C. Manzoni, U. Scherf, E. J. W. List, and G. Lanzani. *Chem. Phys. Lett.* **384** (2004) 251 – 255.

[100] A. Köhler and D. Beljonne. *Adv. Funct. Mater.* **14** (2004) 11 – 18.

[101] Y. V. Romanovskii, A. Gerhard, B. Schweitzer, U. Scherf, R. I. Personov, and H. Bässler. *Phys. Rev. Lett.* **84** (2000) 1027 – 1030.

[102] A. Köhler, J. S. Wilson, R. H. Friend, M. K. Al-Suti, M. S. Khan, A. Gerhard, and H. Bässler. *J. Chem. Phys.* **116** (2002) 9457 – 9463.

[103] H. Wiesenhofer, E. Zojer, E. J. W. List, U. Scherf, J. L. Bredas, and D. Beljonne. *Adv. Mater.* **18** (2006) 310 – 314.

[104] M. A. Ramos and U. Buchenau. *in: Tunneling Systems in Amorphous and Crystalline Solids*, chapter 9, 527 – 569. Springer, Berlin, 1998.

[105] Y. G. Vainer, A. V. Naumov, M. Bauer, and L. Kador. *Phys. Rev. Lett.* **97** (2006) 185501.

[106] J. Friedrich and D. Haarer. *Angew. Chem.* **96** (1984) 96 – 123.

[107] J. L. Richards and S. A. Rice. *J. Chem. Phys.* **54** (1971) 2014 – 2023.

[108] R. F. Mahrt, T. Pauck, U. Lemmer, U. Siegner, M. Hopmeier, R. Hennig, H. Bässler, E. O. Göbel, P. Haring Bolivar, G. Wegmann, H. Kurz, U. Scherf, and K. Müllen. *Phys. Rev. B* **54** (1996) 1759 – 1765.

[109] G. Lanzani, G. Cerullo, C. Brabec, and N. S. Sariciftci. *Phys. Rev. Lett.* **90** (2003) 047402.

[110] Y. V. Romanovskii and H. Bässler. *Chem. Phys. Lett.* **326** (2000) 51 – 57.

[111] R. Loudon. *The Quantum Theory of Light.* Oxford University Press, Oxford, New York, 2000.

[112] Y. R. Shen. *The Principles of Nonlinear Optics.* John Wiley & Sons, New York, 1984.

[113] M. Göppert-Mayer. *Ann. Phys.* **401** (1931) 273 – 294.

[114] T. H. Keil. *Phys. Rev.* **140** (1965) 601 – 617.

[115] E. J. W. List, C. Creely, G. Leising, N. Schulte, A. D. Schlüter, U. Scherf, K. Müllen, and W. Graupner. *Chem. Phys. Lett.* **325** (2000) 132 – 138.

[116] E. Peeters, A. Marcos Ramos, S. C. J. Meskers, and R. A. J. Janssen. *J. Chem. Phys.* **112** (2000) 9445 – 9454.

[117] U. Rant, U. Scherf, M. Rehahn, P. Galda, J. L. Bredas, and E. Zojer. *Synth. Met.* **127** (2002) 241 – 245.

[118] C. Chi, C. Im, and G. Wegner. *J. Chem. Phys.* **124** (2006) 024907.

[119] A. Samoc, M. Samoc, M. Woodruff, and B. Luther-Davies. *Opt. Lett.* **20** (1995) 1241 –1243.

[120] C. Xu and W. W. Webb. *J. Opt. Soc. Am. B* **13** (1996) 482 – 491.

[121] C. Xu, R. M. Williams, W. R. Zipfel, and W. W. Webb. *Bioimaging* **4** (1996) 198 – 207.

[122] I. D. W. Samuel, I. Ledoux, C. Dhenaut, J. Zyss, H. H. Fox, R. R. Schrock, and R. J. Silbey. *Science* **265** (1994) 1070 – 1072.

[123] R. H. Clarke and H. A. Frank. *J. Chem. Phys.* **65** (1976) 39 – 47.

[124] K. F. Freed and S. H. Lin. *Chem. Phys.* **11** (1975) 409 – 432.

[125] M. Bixon and J. Jortner. *J. Chem. Phys.* **48** (1968) 715 – 726.

[126] B. R. Henry and W. Siebrand. *J. Chem. Phys.* **54** (1971) 1072 – 1085.

[127] V. Lawetz, G. Orlandi, and W. Siebrand. *J. Chem. Phys.* **56** (1972) 4058 – 4072.

[128] J. M. Hollas. *Symmetry in Molecules*. Chapman & Hall, London, 1972.

[129] G. Herzberg. *Molecular spectra and molecular structure: Infrared and raman spectra of polyatomic molecules*. Krieger, Malabar, 1991.

[130] J. G. Müller, M. Anni, U. Scherf, J. M. Lupton, and J. Feldmann. *Phys. Rev. B* **70** (2004) 035205.

[131] W. M. McClain. *J. Chem. Phys.* **55** (1971) 2789 – 2796.

[132] L. A. Rebane, A. A. Gorokhovskii, and J. V. Kikas. *Appl. Phys. B* **29** (1982) 235 – 250.

[133] M. Orrit, J. Bernard, and R. I. Personov. *J. Phys. Chem.* **97** (1993) 10256 – 10268.

[134] G. D. Scholes, D. S. Larsen, G. R. Fleming, G. Rumbles, and P. L. Burn. *Phys. Rev. B* **61** (2000) 13670 – 13678.

[135] W. A. Phillips. *J. Low Temp. Phys.* **7** (1972) 351 – 360.

[136] P. W. Anderson, B. I. Halperin, and C. M. Varma. *Phil. Mag.* **25** (1972) 1 – 9.

[137] E. Geva and J. L. Skinner. *J. Phys. Chem. B* **101** (1997) 8920 – 8932.

[138] A. Kiraz, M. Ehrl, C. Hellriegel, C. Bräuchle, and A. Zumbusch. *ChemPhysChem* **6** (2005) 919 – 925.

[139] T. L. Reinecke. *Solid State Commun.* **32** (1979) 1103 – 1106.

[140] P. D. Reilly and J. L. Skinner. *J. Chem. Phys.* **101** (1994) 965 – 973.

[141] L. Kador. *J. Chem. Phys.* **95** (1991) 5574 – 5581.

[142] R. Richert and A. Blumen. *Disorder Effects on Relaxational Processes.* Springer-Verlag, Heidelberg, Berlin, 1994.

[143] W. Barford and C. D. P. Duffy. *Phys. Rev. B* **74** (2006) 075207.

[144] B. Mollay, U. Lemmer, R. Kersting, R. F. Mahrt, H. Kurz, H. F. Kauffmann, and H. Bässler. *Phys. Rev. B* **50** (1994) 10769 – 10779.

[145] T. Förster. *Z. Phys.* **2** (1947) 55 – 75.

[146] H. Wiesenhofer, D. Beljonne, G. D. Scholes, E. Hennebicq, J.-L. Bredas, and E. Zojer. *Adv. Funct. Mater.* **15** (2005) 155 – 160.

[147] Y. Olivier, V. Lemaur, J. L. Bredas, and J. Cornil. *J. Phys. Chem. A* **110** (2006) 6356 – 6364.

[148] B. Schweitzer, G. Wegmann, D. Hertel, R. F. Mahrt, H. Bässler, F. Uckert, U.Scherf, and K. Müllen. *Phys. Rev. B* **59** (1999) 4112 – 4118.

[149] Y. V. Romanovskii, H. Bässler, and U. Scherf. *Chem. Phys.* **276** (2002) 321 – 331.

[150] F. Schindler, J. Jacob, A. C. Grimsdale, U. Scherf, K. Müllen, J. Lupton, and J. Feldmann. *Angew. Chem. Int. Ed.* **44** (2005) 1520 – 1525.

[151] R. Chang, J. H. Hsu, W. S. Fann, K. K. Liang, C. H. Chang, M. Hayashi, J. Yu, S. H. Lin, E. C. Chang, K. R. Chuang, and S. A. Chen. *Chem. Phys. Lett.* **317** (2000) 142 – 152.

[152] D. Somitsch, F. P. Wenzl, J. Kreith, M. Pressl, R. Kaindl, U. Scherf, G. Leising, and P. Knoll. *Synth. Met.* **138** (2003) 39 – 42.

[153] M. Gaal, E. J. W. List, and U. Scherf. *Macromolecules* **36** (2003) 4236 – 4237.

[154] L. Liu, S. Qiu, B. Wang, W. Zhang, P. Lu, Z. Xie, M. Hanif, Y. Ma, and J. Shen. *J. Phys. Chem. B* **109** (2005) 23366 – 23370.

[155] G. Kranzelbinder, H. J. Byrne, S. Hallstein, S. Roth, G. Leising, and U. Scherf. *Phys. Rev. B* **56** (1997) 1632 – 1636.

[156] U. Lemmer, S. Heun, R. F. Mahrt, U. Scherf, M. Hopmeier, U. Siegner, E. O. Göbel, K. Müllen, and H. Bässler. *Chem. Phys. Lett.* **240** (1995) 373 – 378.

[157] A. Bloess, Y. Durand, M. Matsushita, R. Verberk, E. J. J. Groenen, and J. Schmidt. *J. Phys. Chem. A* **105** (2001) 3016 – 3021.

[158] C. Gooijer, F. Ariese, and J. W. Hofstraat. *Shpol'skii Spectroscopy and Other Site-Selection Methods*. Wiley-Interscience, New York, 2000.

[159] E. V. Shpol'skii, A. A. Ilina, and L. A. Klimova. *Dokl. Akad. Nauk SSSR* **87** (1952) 935 – 938. (42) Not in File.

[160] E. Lang, R. Hildner, H. Engelke, P. Osswald, F. Würthner, and J. Köhler. *ChemPhysChem* **8** (2007) 1487 – 1496.

[161] T. R. Corle and G. S. Kino. *Confocal scanning optical microscopy and related imaging systems*. Academic Press, San Diego, London, 1996.

[162] E. Lang, J. Baier, and J. Köhler. *J. Microscopy* **222** (2006) 118 – 123.

[163] R. Hildner. *Aufbau eines Multi-Photonen-Fluoreszenzmikroskops*. Diploma thesis, Universität Bayreuth (2003).

[164] C. C. Corredor, Z. Huang, and K. D. Belfield. *Adv. Mater.* **18** (2006) 2910 – 2914.

[165] W. Zhou, S. M. Kuebler, K. L. Braun, T. Y. Yu, J. K. Cammack, C. K. Ober, J. W. Perry, and S. R. Marder. *Science* **296** (2002) 1106 – 1109.

[166] W. Denk, J. H. Strickler, and W. W. Webb. *Science* **248** (1990) 73 – 76.

[167] A. Diaspro, G. Chirico, and M. Collini. *Quart. Rev. Biophys.* **38** (2005) 97 – 166.

[168] R. Vestberg, R. Westlund, A. Eriksson, C. Lopes, M. Carlsson, B. Eliasson, E. Glimsdal, M. Lindgren, and E. Malmström. *Macromolecules* **39** (2006) 2238 – 2246.

[169] S. V. Frolov, Z. Bao, M. Wohlgenannt, and Z. V. Vardeny. *Phys. Rev. B* **65** (2001) 205209.

[170] W. Barford, R. J. Bursill, and R. W. Smith. *Phys. Rev. B* **66** (2002) 115205.

[171] F. Guo and Z. Y. Shih. *Chem. Phys. Lett.* **370** (2003) 572 – 577.

[172] D. Beljonne, Z. Shuai, J. Cornil, D. A. dos Santos, and J. L. Bredas. *J. Chem. Phys.* **111** (1999) 2829 – 2841.

[173] C. Gadermaier, G. Cerullo, M. Zavelani-Rossi, G. Sansone, G. Lanzani, E. Zojer, A. Pogantsch, D. Beljonne, Z. Shuai, J. L. Bredas, U. Scherf, and G. Leising. *Phys. Rev. B* **66** (2002) 125203.

[174] M. Tong, C.-X. Sheng, and Z. V. Vardeny. *Phys. Rev. B* **75** (2007) 125207.

[175] G. Zerbi and M. Del Zoppo. *in: Modern Polymer Spectroscopy*, chapter 3, 87 – 206. Wiley-VCH, Weinheim, 1999.

[176] H. E. Schaffer, R. R. Chance, R. J. Silbey, K. Knoll, and R. R. Schrock. *J. Chem. Phys.* **94** (1991) 4161 – 4170.

[177] D. Somitsch, F. P. Wenzl, E. J. W. List, P. Wilhelm, U. Scherf, G. Leising, and P. Knoll. *Macromol. Symp.* **181** (2002) 383 – 388.

[178] U. Lemmer, R. F. Mahrt, Y. Wada, A. Greiner, H. Bässler, and E. O. Göbel. *Appl. Phys. Lett.* **62** (1993) 2827 – 2829.

[179] S. C. J. Meskers, J. Hübner, M. Oestreich, and H. Bässler. *Chem. Phys. Lett.* **339** (2001) 223 – 228.

[180] U. Lemmer, R. F. Mahrt, Y. Wada, A. Greiner, H. Bässler, and E. O. Göbel. *Chem. Phys. Lett.* **209** (1993) 243 – 246.

[181] G. R. Hayes, I. D. W. Samuel, and R. T. Phillips. *Phys. Rev. B* **52** (1995) 11569 – 11572.

[182] A. Haugeneder, M. Neges, C. Kallinger, W. Spirkl, U. Lemmer, J. Feldmann, M.-C. Amann, and U. Scherf. *J. Appl. Phys.* **85** (1999) 1124 – 1130.

[183] S. W. Provencher. *Comput. Phys. Comm.* **27** (1982) 213 – 227.

[184] S. W. Provencher. *Comput. Phys. Comm.* **27** (1982) 229 – 242.

[185] Y. Zaushitsyn, K. G. Jespersen, L. Valkunas, V. Sundström, and A. Yartsev. *Phys. Rev. B* **75** (2007) 195201.

[186] L. M. Herz, C. Silva, A. C. Grimsdale, K. Müllen, and R. T. Phillips. *Phys. Rev. B* **70** (2004) 165207.

[187] A. Alvarez, A. Alegria, and J. Colmenero. *Phys. Rev. B* **44** (1991) 7306 – 7312.

[188] A. Pugzlys, R. Augulis, P. H. M. van Loosdrecht, C. Didraga, V. A. Malyshev, and J. Knoester. *J. Phys. Chem. B* **110** (2006) 20268 – 20276.

[189] T.-Q. Nguyen, J. Wu, V. Doan, B. J. Schwartz, and S. H. Tolbert. *Science* **288** (2000) 652 – 656.

[190] K. K. Rebane. *Impurity Spectra of Solids.* Plenum Press, New York, London, 1970.

[191] S. P. Kennedy, N. Garro, and R. T. Phillips. *Phys. Rev. Lett.* **86** (2001) 4148 – 4151.

[192] F. Milota, J. Sperling, V. Szöcs, A. Tortschanoff, and H. F. Kauffmann. *J. Chem. Phys.* **120** (2004) 9870 – 9885.

[193] K. Becker and J. M. Lupton. *J. Am. Chem. Soc.* **127** (2005) 7306 – 7307.

[194] F. Schindler and J. M. Lupton. *ChemPhysChem* **6** (2005) 926 – 934.

[195] L. Borland and M. van Heel. *J. Opt. Soc. Am. A* **7** (1990) 601 – 610.

[196] M. van Heel, B. Gowen, R. Matadeen, E. V. Orlova, R. Finn, T. Pape, D. Cohen, H. Stark, R. Schmidt, M. Schatz, and A. Patwardhan. *Quart. Rev. Biophys.* **33** (2000) 307 – 369.

[197] C. Hofmann, H. Michel, M. van Heel, and J. Köhler. *Phys. Rev. Lett.* **94** (2005) 195501.

[198] C. Hofmann. *Pigment-Pigment Interactions and Protein Dynamics in Light-Harvesting Complexes: a Single-Molecule Study.* Ph.D. thesis, Universität Bayreuth (2004).

[199] Y. Kanematsu, J. S. Ahn, and T. Kushida. *Phys. Rev. B* **48** (1993) 9066 – 9070.

[200] N. Verdal and A. M. Kelley. *J. Chem. Phys.* **118** (2003) 7985 – 7992.

[201] K. K. Rebane. *Chem. Phys.* **189** (1994) 139 – 148.

[202] T. Pauck, H. Bässler, J. Grimme, U. Scherf, and K. Müllen. *Chem. Phys.* **210** (1996) 219 – 227.

[203] N. T. Harrison, D. R. Baigent, I. D. W. Samuel, R. H. Friend, A. C. Grimsdale, S. C. Moratti, and A. B. Holmes. *Phys. Rev. B* **53** (1996) 15815 – 15822.

[204] Y. V. Romanovskii, H. Bässler, and U. Scherf. *Chem. Phys. Lett.* **383** (2004) 89 – 94.

[205] D. A. Braden, S. F. Parker, J. Tomkinson, and B. S. Hudson. *J. Chem. Phys.* **111** (1999) 429 – 437.

[206] K. Inoue, T. Kanaya, S. Ikeda, K. Kaji, K. Shibata, M. Misawa, and Y. Kiyanagi. *J. Chem. Phys.* **95** (1991) 5332 – 5340.

[207] R. Inoue, T. Kanaya, K. Nishida, I. Tsukushi, and K. Shibata. *Phys. Rev. Lett.* **95** (2005) 056102.

[208] S. F. Parker, D. A. Braden, J. Tomkinson, and B. S. Hudson. *J. Phys. Chem. B* **102** (1998) 5955 – 5956.

[209] V. L. Gurevich, D. A. Parshin, and H. R. Schober. *Phys. Rev. B* **67** (2003) 094203.

[210] L. Winterling. *Untersuchung der elektronischen Anregungszustände π-konjugierter Polymere mit Hilfe von Einzelmolekülspektroskopie.* Diploma thesis, Universität Bayreuth (2007).

[211] Y. J. Lee, D. Y. Kim, J. K. Grey, and P. F. Barbara. *ChemPhysChem* **6** (2005) 2404 – 2409.

[212] A. Kiraz, M. Ehrl, C. Bräuchle, and A. Zumbusch. *J. Chem. Phys.* **118** (2003) 10821 – 10824.

[213] K. Orth, P. Schellenberg, and J. Friedrich. *J. Chem. Phys.* **99** (1993) 1 – 6.

[214] J. March. *Advanced Organic Chemistry.* John Wiley & Sons, New York, 1992.

[215] A. V. Naumov, Y. G. Vainer, and L. Kador. *Phys. Rev. Lett.* **98** (2007) 145501.

[216] Z. Yu and P. F. Barbara. *J. Phys. Chem. B* **108** (2004) 11321 – 11326.

List of Publications

- R. Hildner, U. Lemmer, U. Scherf, and J. Köhler. Continuous-Wave Two-Photon Spectroscopy on a Ladder-Type Conjugated Polymer. *Chem. Phys. Lett.* **448** (2007) 213 – 217.

- E. Lang, R. Hildner, H. Engelke, P. Osswald, F. Würthner, and J. Köhler. Comparison of the Photophysical Parameters for three Perylene Bisimide Derivatives by Single-Molecule Spectroscopy. *ChemPhysChem* **8** (2007) 1487 – 1496.

- R. Hildner, U. Lemmer, U. Scherf, M. van Heel, and J. Köhler. Revealing the Electron-Phonon Coupling in Conjugated Polymers by Single-Molecule Spectroscopy. *Adv. Mater.* **19** (2007) 1978 – 1982.

- R. Hildner, U. Lemmer, U. Scherf, and J. Köhler. Picosecond Excitation Energy Relaxation Processes in a Ladder-Type π-Conjugated Polymer. *Chem. Phys. Lett.* **429** (2006) 103 – 108.

Danksagung

Am Ende will ich mich bei allen Personen bedanken, die zum Gelingen dieser Arbeit beigetragen haben. Und sofort stellt sich die Frage: wie macht man das am besten? In den letzten Jahren lernte ich am Lehrstuhl EP IV einige kreative Ideen kennen, aber ich will hier trotzdem eine Standard- (oder mit Leopoldschen Worten: langweilige) Danksagung machen und auf philosophische Betrachtungen zu Danksagungen im allgemeinen und Dissertationen im speziellen (oder umgekehrt) verzichten. Ich bin schließlich kein Philosoph und meine vielen Deutschlehrer haben mir außerdem davon abgeraten, irgendetwas in dieser Richtung zu machen.

Als erstes ist hier mein Doktorvater Prof. Dr. Jürgen Köhler zu nennen, der dieses Projekt in seiner Gruppe ermöglicht hat. Ich durfte eine hervorragende Betreuung genießen, Jürgen hat sich immer viel Zeit genommen, um über meine Ergebnisse zu diskutieren, und er hatte viele entscheidende Tipps und Hinweise, wenn ich nicht weitergekommen bin. Er hat mir aber auch große Freiheit gewährt, dieses Projekt zu bearbeiten und zu entwickeln. Ich möchte mich auch für das große Vertrauen bedanken, dass er in mich gesteckt hat, als das Projekt nach zwei Jahren "auf der Kippe" stand. Als Bayern München-Anhänger kann ich es daher sogar verschmerzen, dass Jürgen – für mich unverständlich – großer Fan der Fahrstuhlmannschaft Borrussia Mönchengladbach ist, und ich halte es mit dem Fußballprofi Marko Reich: "Früher war ich großer Fan von Borrussia Mönchengladbach, aber da hatte ich noch keine Ahnung vom Fußball".

Einen großen Anteil am Erfolg dieser Arbeit hatten auch unsere Kooperationspartner in diesem von der Deutschen Forschungsgemeinschaft finanziell unterstützten Projekt: Prof. Dr. Uli Lemmer möchte ich für die Tipps zu den zeitaufgelösten Messungen und wertvollen Hinweise während der Vorbereitung der Publikation danken, die daraus entstanden ist; außerdem vielen Dank für die Übernahme des 3. Gutachtens. Prof. Dr. Ullrich Scherf sei gedankt für die schnellen Antworten auf meine Anfragen zu neuen Proben, die dann meist schon zwei Tage später in Bayreuth ankamen, und für seine Hinweise zur Handhabung von MeLPPP. Das MSA-Programm wurde von Prof. Dr. Marin van Heel zur

Verfügung gestellt und Ralf Schmidt von Image Science, Berlin, sandte mir immer schnell die nötigen Lizenzdateien zu.

Kapitel 5 wäre sicher nicht in der Form entstanden ohne die Unterstützung von Uwe Denzer und Gerhard Rousseau von Hamamatsu Photonics, die alle meine Fragen und Probleme mit der Streak-Kamera in den berühmten "zwei" Wochen im März 2005 sofort beantwortet haben bzw. lösen konnten, vielen Dank dafür. Auch Prof. Dr. Werner Köhler sei hier gedankt, dass er mir das CONTIN-Programm für die Analyse der zeitaufgelösten Daten zur Verfügung gestellt hat und immer Zeit für meine Fragen und zur Diskussion hatte.

Auch die "Lebenslänglichen" am Lehrstuhl EP IV hatten großen Anteil am Gelingen dieser Arbeit: Danke an Dr. Wolfgang Richter für seine vielen experimentellen Tipps und die hilfreichen, interessanten Diskussionen, die wir führten, an Apl. Prof. Dr. Lothar Kador für viele Hinweise zu den Einzelmolekülmessungen, an unsere Techniker Werner Reichstein und Michael Heimler, die immer schnell bei allen kleineren und größeren Problemen v. a. während der Aufbauphase geholfen haben, und natürlich an die Sektretärinnen Karin Baier und Evelyn Hülsmann für ihre Unterstützung bei allen verwaltungstechnischen Angelegenheiten (die Menge Wasser nach meiner Prüfung war aber trotzdem anders abgesprochen!).

Zu Beginn meiner Arbeit beanspruchte ein großer Teil der Zeit die Ausstattung des neuen Labors, der Umzug des Lasers, der Apparatur und die Inbetriebnahme eines Kryostaten. Ohne die schnelle und kompetente Unterstützung der Mechanikwerkstätten im NW I und vor allem aber im NW II wäre das mit Sicherheit nicht so schnell abgelaufen. Stellvertretend möchte ich Frank Neumann und Hendrik Ohlmeyer, die die meiste Arbeit mit mir hatten, sehr herzlich dafür danken.

Auch meinem neuen Chef, Prof. Dr. Niek F. van Hulst, sei hier gedankt fuer sein Verstaendnis in den ersten Wochen am ICFO, in denen ich mich sicherlich nicht immer 100% ig auf meine neue Aufgabe konzentrieren konnte.

Allen gegenwärtigen und ehemaligen Mitarbeitern am Lehrstuhl EP IV, die ich nicht alle namentlich erwähnen will (sonst vergesse ich noch jemanden), möchte ich für sechs unvergessliche Jahre danken, für die vielen lustigen und interessanten Stunden in der Kaffeee(?)cke, in Biergärten, bei den Lehrstuhlausflügen, die ich leider immer "verpasst" habe, aber auch für viele fachliche Diskussionen und Tipps. Besonderer Danke gebührt hier Erwin Lang, der mir vor allem zu Beginn meiner Diplomarbeit sehr geholfen hat, meinen damaligen Aufbau zu realisieren und mich auch beim Aufbau des Kryostaten unterstützt hat. Unsere vielen Diskussionen, die wir in den gemeinsamen Jahren am Lehrstuhl führten, waren immer sehr hilfreich und haben mir außerdem einen guten Einblick in die Welt der

”kleinen” Moleküle gegeben, was mir bei meiner neuen Stelle sehr hilft. Er war auch immer zur Stelle, wenn es um NW II-Feiern, Biergärten und natürlich um die Verteidigung unseres Lieblingsklubs gegen den Mönchengladbach-Anhänger am Lehrstuhl ging. Auch bei meinem langjährigen Bürokollegen Florian Spreitler möchte ich mich bedanken (nicht nur für die Einladung zu seiner Hochzeit), er hat geduldig meine vielen, manchmal wirren, Gedanken ertragen, und die Diskussionen mit ihm haben mir immer geholfen, wenn ich irgendwo nicht weiter gekommen bin. Nicht zu vergessen natürlich auch die anderen Mitglieder des Streak-Kompetenzteams, Tobias Pflock und Christiane Hofmann, die zur sehr angenehmen Atmosphäre in ”unserem” Labor beigetragen haben. Mit Jürgen Baier habe ich besonders am Ende unserer Arbeiten viele Auswerteprogramme ausgetauscht, was zwar zu kleineren Missverständnissen geführt hat (es macht einen Unterschied, ob die Phononenseitenbande ”links” oder ”rechts” der Nullphononenlinie liegt), aber trotzdem erfolgreich war. Außerdem danke an Carmen Perez Leon und Laura Torre Lorente für ihre Hilfe bei der Aufnahme der Raman- bzw. FTIR-Spektren von MeLPPP.

Auch Laura Winterling und Dominique Ernst möchte ich nicht vergessen, danke für die Einladungen zum Grillen, Feiern und die vielen ESA-Sachen. Laura war ”meine” erste Diplomandin, was für mich eine wichtige und interessante Erfahrung war. Durch ihre vielen Fragen musste ich über einiges nachdenken, bei dem ich dachte, ich wäre mir sicher. Es war aber auch nicht immer leicht, sie für Messungen und Auswertungen zu begeistern, da sie viel nebenher gemacht hat, aber letzlich ist es doch eine erfolgreiche Diplomarbeit geworden (und vielleicht werden es sogar drei Veröffentlichungen ;-). Durch die vielen Diskussionen mit Dominique habe ich viel über Dimere und Energie- und Ladungstransfer in diesen Systemen gelernt, was mir bei meiner neuen Stelle auch zu Gute kommt.

Schließlich will ich mich auch bei meiner Familie, besonders bei meinen Eltern, für ihre große Unterstützung bedanken, was mir ein sorgenfreies Studium inklusive Auslandsaufenthalt ermöglicht hat; und natürlich auch bei meiner Freundin Laura für die wunderschönen letzten beiden Jahre (und hoffentlich noch viele weitere), die ich sehr genossen habe, für ihre Unterstützung und Hilfe in dieser Zeit und beim Start meines neuen Lebensabschnitts in ”ihrem” Land.

Erklärung

Hiermit erkläre ich, dass ich die vorliegende Arbeit selbst verfasst und keine anderen als die angegebenen Quellen und Hilfsmittel benutzt habe.

Bayreuth, den 14.12.2007 _____

Richard Hildner